Mechanisms and Mitigation of Injection-Induced Earthquakes

by

Megan Rose Mary Brown

B.S., Arizona State University, 2007

M.S., University of Missouri, 2015

A thesis submitted to the

Faculty of the Graduate School of the

University of Colorado in partial fulfillment

of the requirement for the degree of

Doctor of Philosophy

Department of Geological Sciences

2019

This thesis entitled:
written by Megan Rose Mary Brown
has been approved for the Department of Geological Sciences

_____

Shemin Ge

_____

Anne Sheehan

Date_____

The final copy of this thesis has been examined by the signatories, and we find that both the content and the form meet acceptable presentation standards of scholarly work in the above mentioned discipline.

ABSTRACT

Brown, Megan Rose Mary (Ph.D., Geological Sciences)

Mechanisms and Mitigation of Injection-Induced Earthquakes

Thesis directed by Professor Shemin Ge

Injection-induced seismicity caused by wastewater injection is a continuing problem for the central and eastern United States. Mitigation of induced earthquakes often focuses on operational parameters like injection rate. While pore pressure increase has been the main mechanism invoked in injection-induced seismicity, other mechanisms like Coulomb static stress transfer may play a role. In this dissertation, I examine the mechanisms of injection –induced earthquakes in relation to mitigation.

I investigate the role of aggregate injection rate, the combined injection rate of multiple wells, by modeling pore pressure increase caused by 22 wastewater disposal wells injecting into the same disposal zone within 30 km of seismicity in Greeley, Colorado. I find that the wells 15 – 30 km from the seismicity contribute approximately 44% of pore pressure increase at the location of the earthquakes. Therefore, aggregate injection rate and well spacing is important when planning mitigation strategies.

I also derive a simple relation between pore pressure change and surface deformation that can be used to constrain hydraulic parameters of confined aquifers to a first-order. This relation can estimate expected surface deformation associated with pore pressure model results, which can then be compared to observed surface deformation using geodetic techniques. I validate this relation by constraining the storativity of an aquifer in Texas that experienced uplift associated with wastewater disposal.

Finally, I investigate the role of small magnitude earthquakes in induced seismicity. I use generic models to test if small magnitude earthquakes can cumulatively transfer, through earthquake interactions, stress of a magnitude comparable to pore pressure increase from wastewater injection. I find that the stress caused by earthquake interactions (Coulomb static stress transfer) is comparable in magnitude to pore pressure increase. However, the area influenced by the increased stress is much smaller than in pore pressure diffusion. This means that earthquake interactions may induce more earthquakes though over a smaller area than pore pressure increase. If earthquake interactions induce additional events, reduction in injection rate or even shutting down a well may not mitigate seismicity. Therefore, earthquake interactions should be taken into account when planning mitigation, especially the timing of mitigation measures.

ACKNOWLEDGEMENTS

This dissertation would not have been possible without the support of my family throughout the years. My parents taught me to make education a priority and then gave their time and effort when I wanted to do *all* the extra activities. They put up with my collection of rocks on the porch since I was five years old and supported me through all my higher education. My sister has been a constant throughout my life and education putting up with listening to me expound on geology and helping me with grammar on many papers along the way.

My advisor, Shemin Ge, is the best advisor I could have had for my PhD. She was supportive of my professional goals from day one and always supported me when I again decided to do *all* the activities. She gave me opportunities to practice teaching and pursue research in pedagogy. She also encouraged me to be a mentor to multiple undergraduate students. She made me a better writer, a better researcher, and a better mentor. And above and beyond being an advisor, she is a friend – welcoming me into her home and always being there to talk about life.

To my committee: Anne Sheehan, Kristy Tiampo, David Budd, and Jonathan Godt. The mentorship and support given were instrumental to my degree, from including me in your groups to giving me extra outside opportunities to giving your time and energy. To my lab mates: Matt Weingarten, Sarah Evans, Steven Henning, Katherine Pfieffer, and Claudia Corona – each of you made me a better scientist, teacher, and mentor. I could not have asked for a better research group than this one. Finally, I need to acknowledge the institutions that funded me through the years: the United States Geological Survey and National Science Foundation.

TABLE OF CONTENTS

LIST OF TABLES

LIST OF FIGURES

CHAPTER 1: INTRODUCTION

1.1 Background

Fluid-induced earthquakes have been the topic of study for decades [e.g. *Healy et al.*, 1968; *Raleigh et al.*, 1976]. Pore pressure increase within pre-existing, critically stressed, optimally oriented faults has been thought to be the main mechanism of injection-induced seismicity [e.g. *Hubbert and Rubey*, 1959; *Healy et al.*, 1968; *Raleigh et al.*, 1976; *Ellsworth*, 2013; *Keranen et al.*, 2014]. Wastewater injection causes increased pore pressure in the injection interval that diffuses into the crystalline basement. The increased pore pressure encounters a critically stressed fault, reduces the effective normal stress along the fault, and induces seismicity. This phenomenon is ubiquitous around the world tied to both injection of fluids and water reservoirs [*National Research Council*, 2013]. Since 2009, injection-induced seismicity research has regained attention due to an increase in earthquake occurrence in the central and eastern United States caused by large-scale wastewater injection into deep sedimentary aquifers [e.g. *Ellsworth*, 2013; *Keranen et al.*, 2013].

Wastewater injection wells fall under the regulation of the Environmental Protection Agency's (EPA) Underground Injection Control (UIC) Program. State agencies usually take primacy over the regulation of wastewater disposal wells. Permitting regulations focus on the protection of usable aquifers, and there are limited regulations surrounding induced seismicity. Seven states do have some form of regulations related to injection-induced seismicity: Arkansas, Colorado, Illinois, Kansas, New Mexico, Oklahoma, and Texas [*Stewart and Ingelson*, 2016]. Arkansas has placed a moratorium on injection in areas with previous injection-induced seismicity [*Stewart and Ingelson*, 2016]. Colorado does not have any direct regulations about

induced seismicity, but has the discretion to reject permits or put certain conditions like seismic monitoring on UIC permits [*COGCC*, 2016; *Stewart and Ingelson*, 2016]. A seismic review is also part of the permitting process for UIC wells in Colorado. In addition, Colorado uses an unofficial traffic light system to respond to induced seismicity [*COGCC*, 2016]. Illinois also follows a traffic light system when dealing with injection-induced earthquakes [*Stewart and Ingelson*, 2016].

Kansas developed a seismic network [*Stewart and Ingelson*, 2016] and called for a reduction in injection rate in five targeted areas of high injection [*Rubinstein et al.*, 2018]. New Mexico acknowledges the occurrence of induced-seismicity, but only requires operators to demonstrate that the well integrity will not be compromised [*Stewart and Ingelson*, 2016]. Oklahoma created an extensive seismic network through the Oklahoma Geological Survey and the United States Geological Survey and imposed a traffic light approach to seismicity monitoring and mitigation [*Stewart and Ingelson*, 2016]. In addition, a 40% reduction in injection rate was required in an "area of interest" in order to mitigate induced earthquakes [*Langenbruch and Zoback*, 2016], though this occurred concurrently with a downturn in the market and a consequential reduction in oil and gas production. Texas requires a history of seismicity in the surrounding 100 square miles of the area of a proposed wastewater disposal well and has language in the permits that allows the permitting organization (Texas Railroad Commission) to go as far as terminating a well if it determines the injection contributes to seismicity [*Stewart and Ingelson*, 2016].

Most of these regulations fall into a category of reactive mitigation, mitigation actions that occur after the seismicity has started, rather than preventative mitigation, measures that occur prior to seismicity in order to prevent the occurrence of earthquakes. One of the main

ways induced earthquakes are mitigated is by decreasing injection rates or shutting down the wastewater disposal well entirely [*Kim*, 2013; *Langenbruch and Zoback*, 2016; *Yeck et al.*, 2016a]. This does not always take into account the numerous wells that inject into the same aquifers in the larger region. In addition, large earthquakes can continue to occur after the injection well(s) have had large reductions in injection rate or been shut down [*Kim*, 2013; *Yeck et al.*, 2017]. To properly plan mitigation strategies, the physical mechanisms that induce earthquakes must be understood.

Mechanisms other than pore pressure increase are being considered. For example, poroelastic effects [*Yeck et al.*, 2016b; *Goebel et al.*, 2017] have been considered as a mechanism for far-field seismicity tens of kilometers from injection wells. In addition, Coulomb static stress transfer (earthquake interactions) has been proposed as a mechanism following both moderate magnitude events [*Sumy et al.*, 2014; *McNamara et al.*, 2015] and considering the cumulative effect of many small magnitude events [*Catalli et al.*, 2013; *Catalli et al.*, 2016; *Qin et al.*, 2018]. Fluid flow through a fault reducing the coefficient of friction may also be a mechanism [*Diao and Espinosa-Marzal*, 2018].

1.2 Summary of Work

Mitigation of fluid-induced earthquakes is a main concern for the public, regulators, and researchers. This dissertation focuses on understanding the mechanisms of fluid-induced earthquakes in order to inform mitigation efforts. Understanding the physical mechanisms that control induced seismicity is the key to planning effective mitigation strategies.

Pore pressure increase is thought to be the main mechanism of fluid-induced earthquakes. Often when earthquakes occur near wastewater disposal wells, the closest well or wells are targeted for mitigation [*Yeck et al.*, 2016a]. While the closest well(s) may contribute the most to

the pore pressure increase, wells further from the seismicity can also contribute. In Chapter 2, I investigate pore pressure change from wells within 30 km of the Greeley, Colorado seismicity. This case study examines the role of wastewater disposal wells beyond the more traditional distance that is often correlated with seismicity. When a felt earthquake (M3.2) occurred in Greeley, Colorado in June 2014, the well closest to the event was the injection well with the highest injection rate. This well was targeted for mitigation, and the bottom of the well was cemented to try to limit the hydraulic connection between the injection interval and the crystalline bedrock below. I modeled the pore pressure change from 22 wells within 30 km of seismicity disposing wastewater into the same disposal zone. I find that the wells furthest away (15 – 30 km) from the earthquakes are responsible for approximately 44% of the pore pressure increase at the location of the earthquakes. This is important when planning mitigation because it indicates that well spacing and the aggregate injection rate of wells are factors that must be considered. A change in the operational parameters (i.e. injection rate) of one particular well may not be effective in mitigating seismicity.

In Chapter 3, I describe a method of estimating surface uplift based on pore pressure change results from groundwater models. This method can give a first-order constraint on the aquifer parameters (hydraulic conductivity and storativity). The estimated uplift can be compared to observed uplift measured by differential interferometric synthetic aperture radar (DInSAR) and other methods like GPS, tilt-meters, and leveling. I outline the derivation of the method and then test the validity using uplift measurements taken by DInSAR in Texas [*Kim and Lu*, 2018]. I use average hydraulic conductivity measurements taken from literature and the injection rate of the well the uplift surrounds to estimate the storativity of the system by matching the uplift observed by DInSAR. I use the analytical Theis [*Theis*, 1935] solution and a

pore pressure model to constrain the storativity of the system. I find that the storativity of the system must be between 10^{-4} and 10^{-3} [-] to have the correct magnitude of uplift to match the observed surface deformation. These values are within the range expected for confined aquifers and translate to an aquifer compressibility value that matches competent bedrock. This simple relation could be helpful in constraining pore pressure models in areas with limited in-situ data like wastewater disposal areas. In addition, the method can be calculated quickly and with a low computational cost.

Chapter 4 investigates a second mechanism that may control the occurrence of injection-induced seismicity – earthquake interactions. In this study, I use generic pore pressure models and Coulomb static stress transfer models to compare the magnitude of stress change caused by pore pressure increase and earthquake interactions. I test whether the cumulative stress change from small magnitude earthquakes is comparable to pore pressure increase. I find that the stress change from the two mechanisms is comparable and that much larger stress changes can occur from earthquake interactions. However, the area with stress changes that promote seismicity is much larger for pore pressure change than for earthquake interactions. This indicates that pore pressure increase can influence a larger area and possibly a larger number of faults, while Coulomb static stress transfer only influences the fault the earthquakes are occurring on and a small surrounding area.

CHAPTER 2: EVALUATING THE EFFECTIVENESS OF INDUCED SEISMICITY MITIGATION: NUMERICAL MODELING OF WASTEWATER INJECTION NEAR GREELEY, COLORADO

Abstract

Mitigation of injection-induced seismicity in Greeley, Colorado, is based largely on proximity of wastewater disposal wells to seismicity and consists of cementation of the bottom of wells to eliminate connection between the disposal interval and crystalline basement. Brief injection rate reductions followed felt events, but injection rates returned to high levels, >250,000 barrels/month, within six months. While brief rate reduction reduces seismicity in the short term, overall seismicity is not reduced. We examine contributions to pore pressure change by injection from twenty-two wells within 30 kilometers of the center of seismicity. The combined injection rate of seven disposal wells within 15 kilometers of the seismicity (Greeley Wells) is correlated with the seismicity rate. We find that injection from NGL-C4A, the well previously suspected as the likely cause of the induced seismicity, is responsible for ~28% of pore pressure increase. The other six Greeley Wells contribute ~28% of pore pressure increase, and the fifteen Far-field Wells between 15 and 30 kilometers from the seismicity contribute ~44% of pore pressure increase. Modeling results show that NGL-C4A plays the largest role in increased pore pressure, but shows the six other Greeley Wells have approximately the same influence as NGL-C4A. Furthermore, the fifteen Far-field Wells have significant influence on pore pressure near the seismicity. Since the main mitigation action of cementing the bottom of wells has not decreased seismicity, mitigation based on reduced injection rates and spacing wells farther apart would likely have a higher potential for success.

The chapter has been previously published:

Brown, M.R.M., S. Ge, A.F. Sheehan, and J.S. Nakai (2017), Evaluating the Effectiveness of Induced Seismicity Mitigation: Numerical Modeling of Wastewater Injection near Greeley, Colorado, *Journal of Geophysical Research Solid Earth,122,* 6569-6582, doi: 10.1002/2017JB014456

2.1 Introduction

The occurrence of wastewater injection induced seismicity has been recognized since the Denver earthquakes at the Rocky Mountain Arsenal starting in the 1960s [*Healy et al.*, 1968; *Hsieh and Bredehoeft*, 1981]. When wastewater disposal well injection causes pore pressure increase along preexisting, critically stressed faults, the effective normal stress is reduced and an induced earthquake can occur. Even though this mechanism has been accepted for decades [*Healy et al.*, 1968; *Raleigh et al.*, 1976; *Ellsworth*, 2013], how to respond and mitigate induced seismicity is still debated. The focus of mitigation, to date, has mostly been on temporarily stopping or reducing the injection as a way to control the seismicity. *Raleigh et al.* [1976] showed the feasibility of changing injection parameters, injection/extraction rates and locations, to control seismicity with the Rangely, Colorado experiments. Mandates for the reduction of injection rates have been used in Oklahoma, and may be effective in lowering the total number of seismic events of magnitude M >3.0 [*Langenbruch and Zoback,* 2016]. However, several large magnitude earthquakes, including the Pawnee, Oklahoma moment magnitude M_w 5.8 earthquake, the largest in Oklahoma's instrumental record, occurred after the mandated injection reduction [*Yeck et al.*, 2017]. Generally, attempts to control the seismicity via controlling injection have not been effective overall [*Bommer et al.*, 2015], especially in enhanced geothermal projects where the largest magnitude earthquakes often occur following the shut-in (stopping of injection/pumping) of the wells. The largest earthquake, an M_w 3.9, in a series of

wastewater injection induced earthquakes in Youngstown, Ohio occurred within 24 hours of the cessation of the injection [*Kim*, 2013]. *Bommer et al.* [2015] suggest a fundamentally different approach to induced seismicity mitigation based on changes to all elements of risk like exposure (e.g. amount of buildings, infrastructure, and people in area of possible shaking) and vulnerability (e.g. susceptibility of structures to damage or adverse consequences). That is, mitigation is not necessarily focused on stopping or even reducing seismicity, but in reducing the risk to communities.

Mitigation actions fall into two categories: preventative measures and reactive measures. Wastewater disposal wells are permitted under the Environmental Protection Agency's (EPA) Underground Injection Control Program, but state agencies often have the regulatory authority. Preventative measures are taken during the permitting process for new wells. Preventative measures may include well spacing requirements to reduce the possibility of combined influence of injection from multiple wells; well siting away from critical infrastructure, population centers, and high-risk facilities; and identification of known earthquake sources (past earthquake locations and known faults). The Colorado regulatory agency, the Colorado Oil and Gas Conservation Commission (COGCC), requires a review of seismicity potential using the Colorado Geological Survey earthquake databases and published maps, United States Geological Survey (USGS) earthquake databases and maps, and other known fault maps [*COGCC*, 2016]. In addition, the COGCC does not allow injection into the Precambrian crystalline basement formations, unless it can be proven that the potential for induced seismicity is low [*COGCC*, 2016].

Reactive responses, in contrast, happen once the induced seismicity has begun. Reactive responses can include change in the injection well operation parameters such as reduced

injection rate or a change in the injection depth interval. In addition, a reactive response may include the complete shutdown of one or more injection well operations. "Traffic-light" systems are sometimes used to trigger reactive measures [*Ellsworth*, 2013; *Bommer et al.*, 2015; *McGarr et al.*, 2015]. In a "traffic-light" system, regulatory agency required action, i.e. lowering injection rates or stopping injection, is taken when earthquakes of a certain number or magnitude occur [*Ellsworth*, 2013; *McGarr et al.*, 2015]. The effectiveness of these systems is often limited by sparse seismic network coverage that results in a relatively high magnitude detection threshold [*Ellsworth*, 2013].

Greeley, Colorado (Figure 2.1) has been the focus of injection induced seismicity research since the occurrence of an M_w 3.2 earthquake in June 2014 [*Yeck et al.*, 2016a] and is a good case for studying the effectiveness of induced seismicity mitigation. Following the earthquakes, reactive mitigation measures included of concreting the bottom of the well and temporary reduction of injection rates. Disposal well NGL-C4A was the closest well to the earthquake and had a high injection rate (between 250,000 and 364,000 barrels per month (bbls/month) during the previous ten months); therefore, NGL-C4A was identified as the likely cause of the induced seismicity. Tests following the June 2014 earthquake of NGL-C4A found the lowest section of the injection interval to be highly fractured. In order to reduce a possible hydraulic connection between the injection formations and the crystalline basement, the bottom of NGL-C4A was cemented [*Yeck et al.*, 2016a]. When additional felt events occurred in August 2016, similar mitigation efforts were taken at two addition disposal wells near the seismicity, EWS-2 and HPD Kersey 1 (Figure 2.1). Here we use numerical groundwater models to determine if the mitigation efforts were effective. We model the pore pressure change caused by injection from 22 wastewater injection wells within 30 km of the seismicity to determine the

relative contribution of injection of Greeley Wells close to the seismicity (< 15 km) and the Far-field Wells farther from the seismicity (15 – 30 km). The change in the injection interval caused by the cementing the bottom of the well, the main mitigation action, is also captured during the modeling.

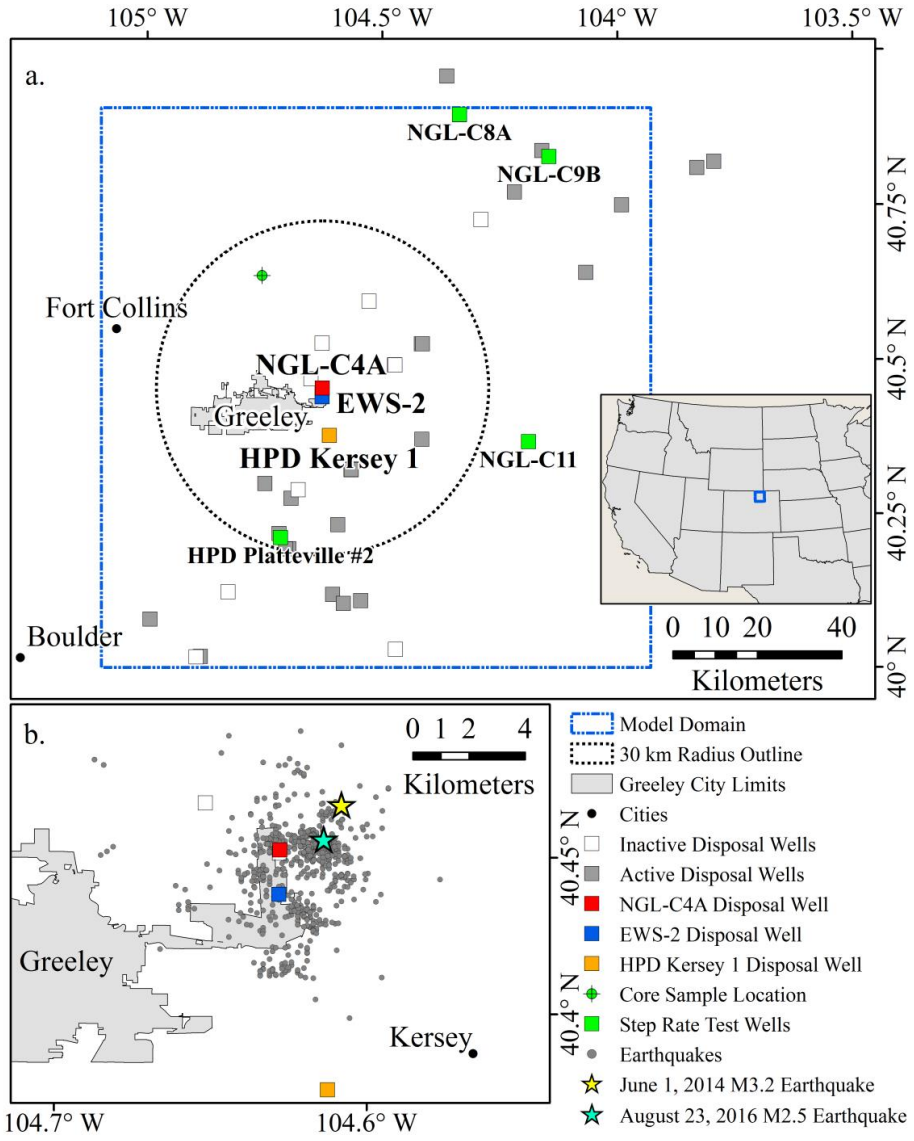

Figure 2.1: Study area. (a.) Wastewater disposal wells (squares) within Weld County, Colorado. Disposal Wells that were involved in mitigation efforts are NGL-C4A in red, EWS-2 in blue, and HPD Kersey 1 in orange. Step Rate Test reanalysis wells are marked in green. The well location for the core used in constant-head permeameter tests is marked in green circle with cross. The model domain is outlined in dashed-blue, and the 30 km radius circle centered on the center of seismicity is in dashed-black. (b.) Seismicity from June 2014 to August 2016. Yellow star indicates the location of the June 1, 2014 Mw 3.2 earthquake and the blue star indicated the location of the felt earthquakes on August 23, 2016. Earthquake data between November 2013 and April 2015 are from *Yeck et al.* [2016a].

2.2 Study Site Background

Greeley, Colorado (Figure 2.1) is located near the north-south trending axis of the asymmetrical Denver-Julesburg (DJ) Basin (also called Denver Basin). The DJ Basin, a Laramide-age structure, is approximately 180,000 km2 in eastern Colorado, extending into Wyoming and Nebraska [*Higley and Cox*, 2007]. Oil and gas produced in the DJ Basin, the majority of which is in Colorado, is a major contributor to Colorado's total oil and gas production annually. The DJ Basin has produced hydrocarbons since 1881, when the first well was drilled in the basin [*Higley and Cox*, 2007]. During the production of hydrocarbons, a large amount of wastewater is generated and must be disposed of either through wastewater disposal wells, wastewater recycling, or trucking of wastewater elsewhere. Wastewater disposal via Underground Injection Control Program Class II wastewater disposal wells is the leading disposal method near Greeley, Colorado. Currently, there are over 30 disposal wells near Greeley (Figure 2.1) injecting into the Denver Basin combined disposal zone. The Denver Basin combined disposal zone is a sedimentary interval of approximately 500-meter thick, comprised of the Permian Lyons sandstone Formation, the interbedded sandstone and carbonate Wolfcamp and Ingleside Formations, and the Pennsylvanian Fountain coarse-grained arkose Formation (Table 2.1). The Denver Basin combined disposal zone is directly underlain by the Precambrian crystalline basement. A small number of the disposal wells (six) inject into only the upper Denver Basin combined disposal zone (Lyons Formation), while the majority of the disposal wells inject into the entire disposal zone (Lyons through Fountain Formations).

Table 2.1: Denver Basin combined disposal zone lithology

Formation	Dominate Lithology	Approximate Thickness (m)
Confining Layer		
Lykins	Mudstone	190
Injection Interval		
Lyons	Sandstone	95
Lower Satanka	Shale	91
Wolfcamp	Sandstone & Carbonate	107
Ingleside	Sandstone & Carbonate	80
Fountain	Coarse-Grained Arkose	170
Basement		
Precambrian Basement	Crystalline Basement	N/A

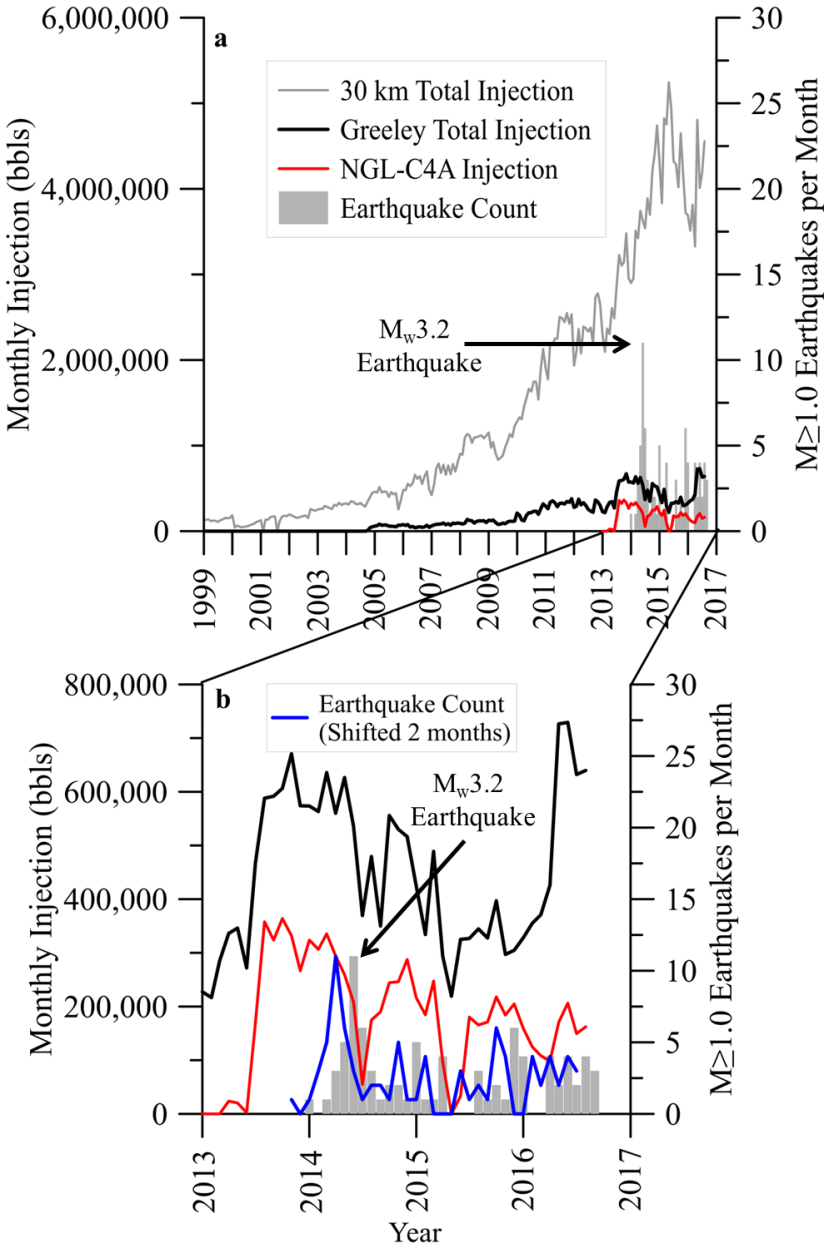

Figure 2.2: Injection and seismicity M>1.0 history. (a.) History of wastewater injection, into the Denver Basin combined disposal zone, within 30 km of the area of seismicity. The grey line represents the total monthly injection for all the wells; the black line is the total monthly injection for the Greeley Wells. The bar graph represents the earthquakes per month. (b.) Total monthly injection for the Greeley Wells and earthquakes per month for January 2013 through August 2016. The blue line represents the earthquakes per month shifted two months to show the approximate lag in the correlation between the injection and seismicity. Earthquake data between November 2013 and April 2015 are from *Yeck et al.* [2016a].

An M_w 3.2 earthquake occurred near Greeley on June 1, 2014 (Figure 2.1b). Prior to this earthquake, the area had not experienced a reported earthquake for more than 41 years [*Yeck et al.*, 2016a]. Following the earthquake, University of Colorado Boulder researchers deployed six seismometers to monitor the seismicity in the area. Injection volumes, well logs, and injection tests were obtained from publicly available sources at the Colorado Oil and Gas Conservation Commission [*COGCC*, 2016]. The earthquake occurred close to the wastewater disposal well NGL-C4A, which started injection in April 2013 and injected consistently over 250,000 bbls/month, with a maximum rate of 363,888 bbls/month, from August 2013 to June 2014. *Weingarten et al.* [2015] studied the relationships between wastewater disposal well injection parameters and seismicity in the central United States and showed a statistically significant correlation between high injection rate (> 300,000 bbls/month) and occurrence of earthquakes.

NGL-C4A was the closest well to the M_w 3.2 earthquake and had the highest injection rate among the wells near Greeley. This disposal well became the focus of the investigation and seismicity mitigation efforts. *Yeck et al.* [2016a] used subspace detection methods to determine when the earthquakes began and found seismicity commenced in November 2013, several months following the initial injection at NGL-C4A. Prior to November 2013, no earthquakes occurred within the Greeley area, which is further confirmed by no seismicity detected from 2008-2010 in the small magnitude seismicity catalog from *Nakai et al.* [2017a]. In addition, drilling logs and a spinner survey (a downhole measurement of fluid velocity with depth) conducted on NGL-C4A after the June 2014 earthquake suggest a highly fractured interval in the mid-to-lower Fountain Formation that was receiving the majority of the injected wastewater. Additional events in June 2014 prompted the COGCC to require the NGL-C4A Well to be shut-in. To mitigate hydraulic connection between the injection interval and the basement, the bottom

500 feet (152.4 meters) of the well was plugged with cement [*Yeck et al.*, 2016a]. After the plugging, injection resumed into the interval above the cemented section. The resumed injection followed a tiered injection rate scheme: slowly increasing injection rate over time. In addition, seismic monitoring by the operators around new disposal wells with injection rates >10,000 bbls/day (~300,000 bbls/month) was instituted as a precautionary measure.

Induced earthquakes can occur at distances of greater than 20 or 30 km from the wastewater disposal wells [*Keranen et al.*, 2014; *Block et al.*, 2015]. Within 30 km of the induced seismicity, an additional twenty-one wastewater disposal wells (Table 2.2 and Figure 2.1) are injecting or have injected into the Denver Basin combine disposal zone. The majority of the disposal wells inject into the entire Denver Basin combined disposal zone, but six inject into only the upper Denver Basin combined disposal zone, the Lyons Formation. The first injection within the 30 km radius began in January 1999; nine of the wells began injection after the June 2014 earthquake. To determine how much impact the injection from the additional wells has on pore pressure change, we modeled the pore pressure generated from injection of the twenty-two wells from January 1999 through August 2016 using a 3D numerical groundwater model of the basin.

Table 2.2: Denver Basin combined disposal zone wastewater disposal wells within 30 km of seismicity [1]

Well Name	API	Date of Injection	Distance from NGL-C4A [km]	Latitude	Longitude	Disposal Zone
NGL-C4A	0512335841	Apr-2013 to Present	0.00	40.45	-104.63	Denver Basin combined disposal zone
NGL C4	0512312448	Oct-2004 to Nov-2014	0.11	40.45	-104.63	Upper Denver Basin combined disposal zone
EWS 2 [former Triton #2]	0512337808	May-2015 to Present	1.58	40.44	-104.63	Denver Basin combined disposal zone
Johnson 22-34I	0512326604	Mar-2008 to Feb-2010	2.62	40.47	-104.65	Upper Denver Basin combined disposal zone
NGL-C10	0512340772	Feb-2016 to Present	8.08	40.53	-104.63	Denver Basin combined disposal zone
HPD Kersey 1	0512327116	Jan-2010 to Present	8.62	40.38	-104.61	Denver Basin combined disposal zone
Synergy Disposal 15-18 I	0512325694	Nov-2008 to May-2015	13.69	40.49	-104.47	Upper Denver Basin combined disposal zone
Conquest SWD 1-8	0512316804	Jan-1999 to Nov-2007	15.52	40.32	-104.57	Upper Denver Basin combined disposal zone
NGL-C1B	0512329536	Mar-2009 to Present	15.53	40.32	-104.57	Denver Basin combined disposal zone
NGL-C1C	0512340377	Mar-2015 to Present	15.57	40.32	-104.57	Denver Basin combined disposal zone
NGL C1A (SWD 1-8A)	0512323038	Jan-2006 to Present	15.59	40.32	-104.57	Upper Denver Basin combined disposal zone
NGL-C7A	0512332207	Mar-2011 to Present	19.54	40.52	-104.42	Denver Basin combined disposal zone
NGL-C7B	0512334520	Aug-2014 to Present	19.72	40.52	-104.41	Denver Basin combined disposal zone
EWS-3 [former Triton 1]	0512337120	Sep-2014 to Present	20.05	40.30	-104.75	Denver Basin combined disposal zone
NGL-C12	0512341201	Oct-2015 to Present	20.16	40.37	-104.42	Denver Basin combined disposal zone
NGL-C3A	0512331735	Oct-2014 to Present	20.64	40.27	-104.69	Denver Basin combined disposal zone
NGL C3 [Geraldine 32-1]	0512319688	Jan-2000 to Feb-2015	20.65	40.27	-104.69	Upper Denver Basin combined disposal zone
LSWD-1	0512330367	Apr-2012 to Present	24.77	40.23	-104.59	Denver Basin combined disposal zone
HPD Platteville #1	0512329168	Jan-2010 to Present	27.34	40.22	-104.72	Denver Basin combined disposal zone
HPD Platteville #2	0512339710	Mar-2015 to Present	28.00	40.21	-104.72	Denver Basin combined disposal zone
NGL-C6	0512326004	Nov-2007 to Present	29.58	40.19	-104.70	Denver Basin combined disposal zone
NGL-C6A	0512340968	May-2015 to Present	29.74	40.19	-104.71	Denver Basin combined disposal zone

[1] Data from [*COGCC*, 2016] listed in order of distance from NGL-C4A. Greeley Wells, within 15 km of seismicity, are shaded grey.

2.3 Wastewater Injection and Seismicity Data

Taking into account all the wells within 30 km of the seismicity, the total injection rate has been over 1 million bbls/month since 2009 and consistently over two million bbls/month since 2012 (Figure 2.2a). Between the start of injection at NGL-C4A and the June 2014 earthquake, the averaged total injection rate for all wells was approximately three million bbls/month. Between June 2014 and August 2016, when another felt sequence of earthquakes occurred, the average injection rate for all wells has been over four million bbls/month.

Seismicity in the area visually correlates with the injection rate of the seven Greeley Wells that are within 15 km of the seismicity with only short time lags of approximately a few months between the peak injection months and increased seismicity (Figure 2.2b). The data are for the entire period over which both the injection data and seismicity data are available. Seismicity began in November 2013 [*Yeck et al.*, 2016a], and continues through the present. Seismicity decreased after the felt sequence in June 2014 corresponding with the decreased injection rates. Seismicity increased again in January 2015, shortly after the injection of the Greeley Wells exceeded 500,000 bbls/month. Another peak in seismicity occurred in April 2015, shortly after injection reached 490,000 bbls/month. Spatially, there is not a clear diffusion front in the seismicity migration.

The seismic data are from *Yeck et al.* [2016a] and this study with varying magnitudes of completeness. We determined the magnitude of completeness, the minimum magnitude of complete earthquake record in a catalog, using the maximum curvature method [*Wiemer and Wyss*, 2000; *Woessner and Wiemer*, 2005]. A conservative magnitude of completeness for all the datasets is M 1.0. Figure 2.2 presents the pattern of correlation between the injection rates and the seismicity above the magnitude of completeness M 1.0.

Currently, four of the original six seismometers installed near NGL-C4A continue to monitor seismicity in the area. Two of the original six seismometers were removed in April 2015, and one of the remaining four seismometers was relocated in June 2016. Between May 2016 and August 2016, an additional nine seismometers were installed in the area. We also installed one seismometer at the Rocky Mountain Arsenal National Wildlife Refuge, approximately 65 km southwest of Greeley.

2.4 Hydrologic Parameters

Hydrologic parameters are needed for modeling of pore pressure generated from injection. To estimate hydrologic parameters for the injection interval, we reanalyzed step rate test data on four wells with injection intervals in the Denver Basin combined disposal zone (Figure 2.1a) and conducted constant-head permeameter tests on core samples from the injection interval units. The step rate test data are obtained from the *COGCC* [2016]. We took core samples from the 1UPPR-Ferch Core (Figure 2.1a) stored at the U.S. Geological Survey's Core Research Center [*USGS CRC*, 2016].

2.4.1 Step Rate Test as Variable Rate Injection Test

Step rate tests are conducted on injection wells during the well permitting process to determine the injection interval's fracture parting pressure – the pressure at which preexisting fractures extend or new fractures form within the formation. During a step rate test, pressure in the injection well is initially allowed to equilibrate to formation pressure [*Singh et al.*, 1987]. A variable rate injection test is then performed in a step rate fashion using steps of equal time length and increasing injection rate. The length of the time step is chosen such that the bottom-hole pressure is stabilized at the end of each time step, for wells near Greeley usually less than 30 minutes. Data recorded are the injection rate and well bottom-hole pressure. The injection rate

versus the stabilized bottom-hole pressure data are expected to be linear with a constant slope until the fracture parting pressure is reached. Once the fracture parting pressure is reached, fractures are created and they act as higher permeability conduits for fluid and pressures are lowered, resulting in a reduced slope.

We analyzed the step rate test data from four wells, HPD Platteville #2, NGL-C11, NGL-C8A, NGL-C9B (Figure 2.1a), as a step-drawdown test, which is a variable rate pumping test used to determine hydrologic properties under different pumping conditions. The data are from the *COGCC* [2016] well files for the four disposal wells. Step rate and step-drawdown tests have similar procedures although one test injects (step rate test) while the other pumps (step-drawdown test). Since the two tests have a procedure of step rate injection/pumping, the same equation that solves the step-drawdown test can be used on data from the step rate test to estimate hydraulic conductivity. The sign on the pumping rate and change in hydraulic head is just reversed for injection and increasing hydraulic head.

We use the program AQTESOLV [*Duffield*, 2006] for the analysis. AQTESOLV solves for transmissivity and storativity using a modified version of the Theis method [*Theis*, 1935] for step-drawdown tests in confined aquifers; we use this method for single-well tests assuming fully penetrating wells and taking into account linear and nonlinear well losses [*Bear*, 1979 p. 374-375]:

$$\Delta h = \frac{\mathrm{Q}}{4\pi \mathrm{T}}[w(u) + 2S_w] + CQ^P \quad (1)$$

$$w(u) = \int_u^\infty \frac{e^{-x}}{x} dx \quad (2)$$

$$u = \frac{r^2 S}{4Tt} \quad (3)$$

where is change in hydraulic head in the pumped/injected well [L], Q is pumping or injection rate [L^3 T^{-1}], T is transmissivity [L^2 T^{-1}], S_w is the wellbore skin factor [1], CQP is

nonlinear well loss [L], is the well function [1], *u* is a dimensionless time parameter [1], *x* is the variable of integration [1], *r* is radial distance of influence [L], *S* is storativity [1], and *t* is time [T]. The radius of the well is used for the radial distance when analyzing single-well tests in AQETSOLV. Single-well tests estimate transmissivity well, but storativity values are hard to estimate from due to the well losses [*Jacob*, 1947; *Agarwal et al.*, 1970; *Renard et al.*, 2009]. The wellbore skin factor S_w relates to the change in permeability of the formation at the borehole due to damage during drilling or well completion [*Bear*, 1979]. Positive wellbore skin factors indicate the damaged area has a lower hydraulic conductivity than the actual formation; negative wellbore skin factors indicate the damaged area has a higher hydraulic conductivity than the actual formation [*Yang and Gates*, 1997]. The well loss constant *C* takes into account the well's construction (e.g. screen, liner, gravel pack) and the quality of its completion.

By varying the nonlinear well loss variables, we found the transmissivity is insensitive to the nonlinear well loss. We used several skin factors during analysis to achieve the best solution. We included an anisotropy ratio, vertical hydraulic conductivity over horizontal hydraulic conductivity (*Kv/Kh*), of 1:10 in the analysis, which was confirmed by the constant-head permeameter testing (see section 2.4.2). Using the thickness of the injection interval, we calculated the hydraulic conductivity for the disposal zone in each well.

The hydraulic conductivity ranges from approximately 10^{-8} to 10^{-7} meters per second (m s^{-1}). We note that while solution (1) assumes a homogeneous aquifer, the step rate tests were conducted over the entire injection interval, which includes numerous formations of varying composition, including sandstones and carbonates. The entire injection interval, therefore, can be heterogeneous. The hydraulic conductivity results between the wells that are located across the basin are consistent.

2.4.2 Constant-Head Permeameter Tests

We conducted constant-head permeameter tests on samples collected from core drilled in the DJ Basin and stored at the USGS CRC in Denver, Colorado. The core samples are from the 1 UPPR-Ferch Well (Figure 2.1a) that was cored through all of the geologic units of the Denver Basin combined disposal zone. We took samples from the Lyons, Wolfcamp, Ingleside, and Fountain Formations. These formations are largely sandstones, but there are some carbonates interbedded within the Wolfcamp and Ingleside Formations. The samples were picked based on previous permeability values estimated by petrophysical service companies [*USGS CRC*, 2016]. We chose samples of relatively higher permeability estimates as those intervals are where most of the injection fluid will go within the heterogeneous injection interval.

The USGS CRC cut the core samples to a diameter of 2.5 cm. We secured the ten samples in PVC pipe for testing on a Trautwein M100000 Standard Panel permeameter. We saturated the samples by allowing at least 50 milliliters (mL) of water, which is greater than 25 pore volumes, to flow through the sample. We then ran multiple constant-head tests by measuring the time for at least 20 mL of water to flow through the sample. We calculated the hydraulic conductivity of each test using a variation of Darcy's Law [*Freeze and Cherry*, 1979]:

$$K = \frac{VL}{\pi r^2 ht} \tag{4}$$

where K is hydraulic conductivity in the direction of flow [L T^{-1}], V is volume of fluid discharged [L^3], L is sample length [L], r is sample radius [L], h is the constant head difference maintained across the sample [L], and t is time [T]. The results range from 10^{-10} to 10^{-6} m s^{-1}. These values are consistent with the hydraulic conductivities used by [*Belitz and Bredehoeft*, 1988] to model groundwater flow in the DJ Basin aquifers. We conducted tests on three sets of samples, one from the Lyons Formation, one from the Ingleside Formation, and one from the Fountain Formation, to measure the vertical and horizontal hydraulic conductivities from the

same interval. The anisotropy (K_v/K_h) was 0.16 for the Lyons sandstone samples, 0.06 for the Ingleside sandstone/carbonate samples, and 0.19 for the Fountain coarse-grained arkose samples. The disparity in anisotropy values is likely due to the differences in lithology of the three formations or natural variation between the samples. However, the difference in the anisotropy values is only within one order of magnitude. Constant-head permeameter test data for these samples and additional samples are presented in the Data (section 2.8).

2.5 Groundwater Modeling of Pore Pressure Distribution Generated by Injection

2.5.1 Model Setup

We modeled the change in pore pressure caused by wastewater injection from the twenty-two wells within a 30 km radius of the Greeley seismicity using the USGS 3D finite difference model MODFLOW-2005. MODFLOW solves the 3D transient groundwater flow equation for hydraulic head [*McDonald and Harbaugh*, 1988]:

$$S_s \frac{\partial h}{\partial t} = \frac{\partial}{\partial x}\left(K_x \frac{\partial h}{\partial x}\right) + \frac{\partial}{\partial y}\left(K_y \frac{\partial h}{\partial y}\right) + \frac{\partial}{\partial z}\left(K_z \frac{\partial h}{\partial z}\right) + Q \quad (5)$$

where S_s is specific storage [L^{-1}]; h is hydraulic head [L]; t is time [T]; K_x, K_y, and K_z are hydraulic conductivity in the x, y, and z directions [$L\ T^{-1}$]; and Q is the volumetric flux per unit volume of sources and/or sinks [T^{-1}]. Change in hydraulic head is calculated by subtracting the head at each time step by the initial conditions (steady-state conditions). We converted the change in hydraulic head into pore pressure change using the specific weight conversion:

$$\Delta P = \gamma \Delta h \quad (6)$$

where ΔP is pore pressure change [$MLT^{-2}L^{-2}$], γ is the specific weight of water [$MLT^{-2}L^{-3}$], and Δh is hydraulic head change [L].

We created a 3D model of 100 km by 100 km by 8.6 km that captures the asymmetric nature of the Denver Basin combined disposal zone formations (Figure 2.3). The model domain

is large to reduce the effect of boundary conditions on the changes caused by the injection of the wells near the center of the model domain. We assigned constant head boundaries to the east and west sides of the domain with constant heads consistent with the hydraulic head measurements given for the units in [*Belitz and Bredehoeft*, 1988]. This constant head condition ensures a background regional flow of the injection interval from west to east. We set a general-head boundary on the south boundary. General-head boundaries are head-dependent flux boundaries where the flux is dependent on the difference between the simulated head inside the boundary and a specified head at a certain distance beyond the boundary. The specified head are those on the southernmost part of the DJ Basin obtained from the modeling study of [*Belitz and Bredehoeft*, 1988]. A no-flow boundary is assigned to the north boundary since the boundary is far enough from the injection that the modeled pore pressure change caused by injection is not affected by the boundary conditions. We assigned a constant head boundary on the model top to simulate a constant water table that follows the topography at the surface of the model domain.

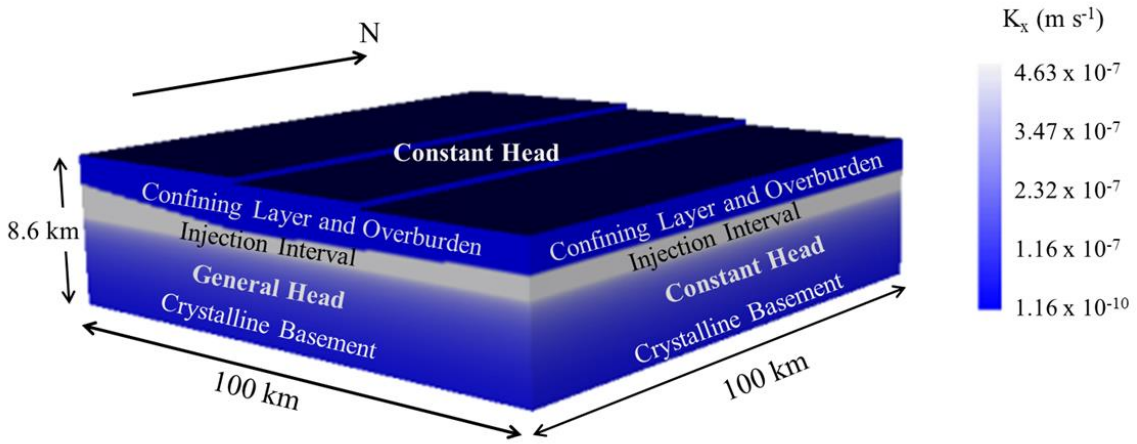

Figure 2.3: Model set-up. The west and east boundaries have a constant head boundary condition. The model top follows local topography and is a constant head boundary. The south boundary is a general head boundary and the north boundary (not shown) is a no-flow boundary. In all of the model runs, horizontal hydraulic conductivities K_x and K_y are equal, and the basement horizontal hydraulic conductivity decreases exponentially with depth. K_z is equal to K_x in the modeled scenarios shown in Figure 2.4. However, vertical anisotropy, K_z/K_x, is varied during the sensitivity analyses.

As a base case, we set an isotropic, homogeneous hydraulic conductivity of the Denver Basin combined disposal zone (injection interval) to 4.6 x 10^{-7} m s^{-1}. This value is on the high end of the permeameter test results, which ranged from 10^{-10} to 10^{-7} m s^{-1}, and is consistent with the step rate test as variable rate injection test analysis, which ranged from 10^{-8} to 10^{-7} m s^{-1}. *Schulze-Makuch et al.* [1999] showed that in heterogeneous systems hydraulic conductivity scales with the volume of the tested sample. Therefore, larger volume pumping (or injection) tests are a more representative estimation of the aquifer parameters than small volume permeameter tests. While there is likely lateral heterogeneity throughout the Denver Basin, the results from the step rate test analyses are consistent and cover a wide area across the basin. In addition, the hydraulic conductivities calculated from the constant-head permeameter testing are

also consistent with the step rate test estimations. The consistency in the estimated values from different wells across such a wide area supports our choice to model the injection interval as a homogeneous unit.

We assigned a hydraulic conductivity of 1.6×10^{-10} m s^{-1} to the confining layer, the Lykins mudstone Formation, above the injection interval. We assigned a hydraulic conductivity the same as the injection interval to the top of the crystalline basement and decreased the conductivity of the basement exponentially with depth [*Manning and Ingebritsen*, 1999]. We assigned a specific storage of 10^{-7} m^{-1}, which is in the range of values estimated in the step rate test as a variable rate injection test analysis and is consistent with values in the literature for the injection intervals [*Colorado Division of Water Resources*, 1976]. We ran the model under steady-state conditions without injection to acquire initial head conditions for the transient model. The initial hydraulic heads approximate the potentiometric surface from *Belitz and Bredehoeft* [1988] of the injection interval units that is a result of steady-state regional groundwater flow modeling study.

We placed the wells in our model based on the well logs provided by the *COGCC* [2016]. We assign the injection interval of NGL-C4A to reflect the change in the injection interval following the cementation of the bottom in June 2014. We used the injection records from the COGCC to calculate the injection rate through time for each of the twenty-two wells. The injection volume and number of injection days are reported to the COGCC on a monthly basis, and we estimated the daily injection rate by dividing the injection volume by number of injection days. We ran the model from January 1, 1999 through August 31, 2016. Each of the twenty-two wells inject for at least a portion of the time.

2.5.2 Pore Pressure Model Results

We present the modeled pore pressure change (Figure 2.4a) for November 2013, when the seismicity began; June 2014 (Figure 2.4b), when the M_w 3.2 earthquake occurred; and August 2016 (Figure 2.4c), when an addition felt sequence of earthquakes occurred. Most of the seismicity occurred between two and five km below mean sea level (bmsl) (3.4 – 6.4 km below ground surface) with the majority of the earthquakes occurring at approximately 4.25 km bmsl [*Yeck et al.*, 2016a] (5.6 km below ground surface). Therefore, we present the pore pressure change at four km bmsl (~5.4 km below ground surface) (Figures 2.4a-2.4c).

The earthquakes prior to June 2014 were detected using subspace detection methods applied to two regional seismic stations, >100 km from the events [*Yeck et al.*, 2016a]. We assume the detected November 2013 earthquakes are in the same area of the first locatable earthquakes (June 2014) based on the waveforms matching during the subspace detection. Therefore, the November 2013 earthquakes all occur in the area where model results predicted an increase in pore pressure of approximately 0.10 MPa (Figure 2.4a). The June 2014 earthquakes (Figure 2.4b) also occur within the area of approximately 0.10 MPa of pore pressure increase. By August 2016, the area where seismicity occurs has a pore pressure increase of approximately 0.15 MPa (Figure 2.4c). The north-south cross-section in Figure 2.4d, through the area of seismicity and NGL-C4A, shows the injection interval experiences a much larger increase in pore pressure than the crystalline basement where the majority of the earthquakes occur. In addition, the increased pore pressure extends deep into the basement and to the south of the injection wells. The injection wells closest to the cross-section are indicated in Figure 2.4d by triangles at the surface of the model.

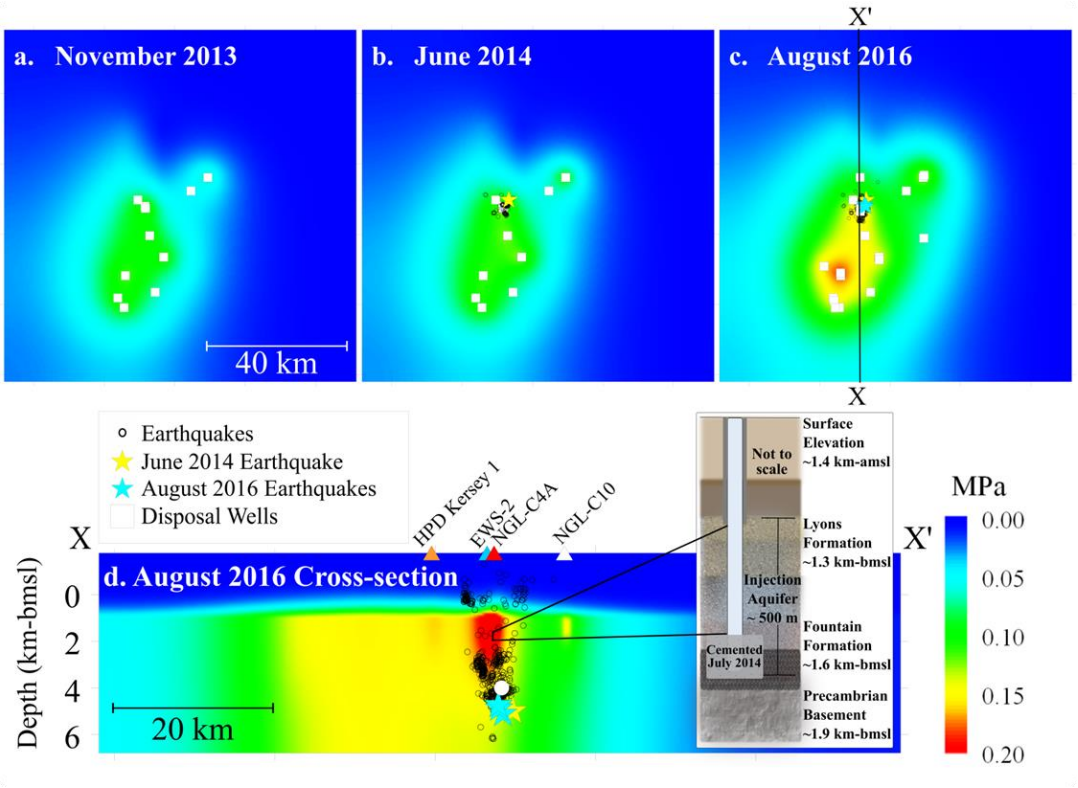

Figure 2.4: Modeled pore pressure results viewed at 4 km-bmsl (a. – c.). Wastewater disposal wells are labeled in white squares. (a.) Pore pressure for November 2013. (b.) June 2014 pore pressure with June 2014 earthquakes in black circles and the June 1, 2014 M_w 3.2 earthquake indicated by the yellow star. (c.) Pore pressure for August 2016 with all earthquakes since June 2014 in black circles and August 2016 felt earthquakes as blue stars. The line X-X' is the location of the cross-section in (d.). (d.) Cross-section X-X' with earthquakes projected onto the cross-section. The main grouping of seismicity starts directly below the bottom of the injection interval (~1.7-1.9 km-bsl) and extends deeper into the basement. The white dot, approximately 2 – 2.5 km below the injection interval, is the location of model estimates shown in Figures 2.5 and 2.6. Earthquake locations from June 2014 through April 2015 are from *Yeck et al.* [2016a]. Surface locations of wastewater injection wells close to the cross-section are labeled with triangles. An inset of a generalized well diagram of NGL-C4A with main injection interval formations labeled is included to illustrate the Denver Basin combined disposal zone. The well diagram is modified from *Yeck et al.* [2016a].

These results are from the base case scenario with mid-range hydraulic conductivity in the injection interval, no anisotropy, and no fractured (higher hydraulic conductivity) layer. We tested other scenarios during the sensitivity analysis. We performed sensitivity analyses of the model for a range of hydraulic conductivities obtained from the permeameter tests and step rate tests analysis. In addition, we ran the model with combinations of anisotropy and the presence of a high hydraulic conductivity fractured layer near NGL-C4A and across the entire basin (Figure 2.5), a feature inferred from the well logs and the spinner survey conducted on NGL-C4A. Model results using the lowest hydraulic conductivity values for the injection interval produced unrealistically high pore pressure changes and, therefore, are not presented. Figure 2.5 presents the pore pressure change at a location (shown in Figure 2.4d) near the majority of the earthquakes for each of the sensitivity analysis results. Excluding the highest hydraulic conductivity scenario, the pore pressure near the majority of the earthquakes increases in the sensitivity analysis to at least 0.08 MPa by November 2013 when the seismicity started.

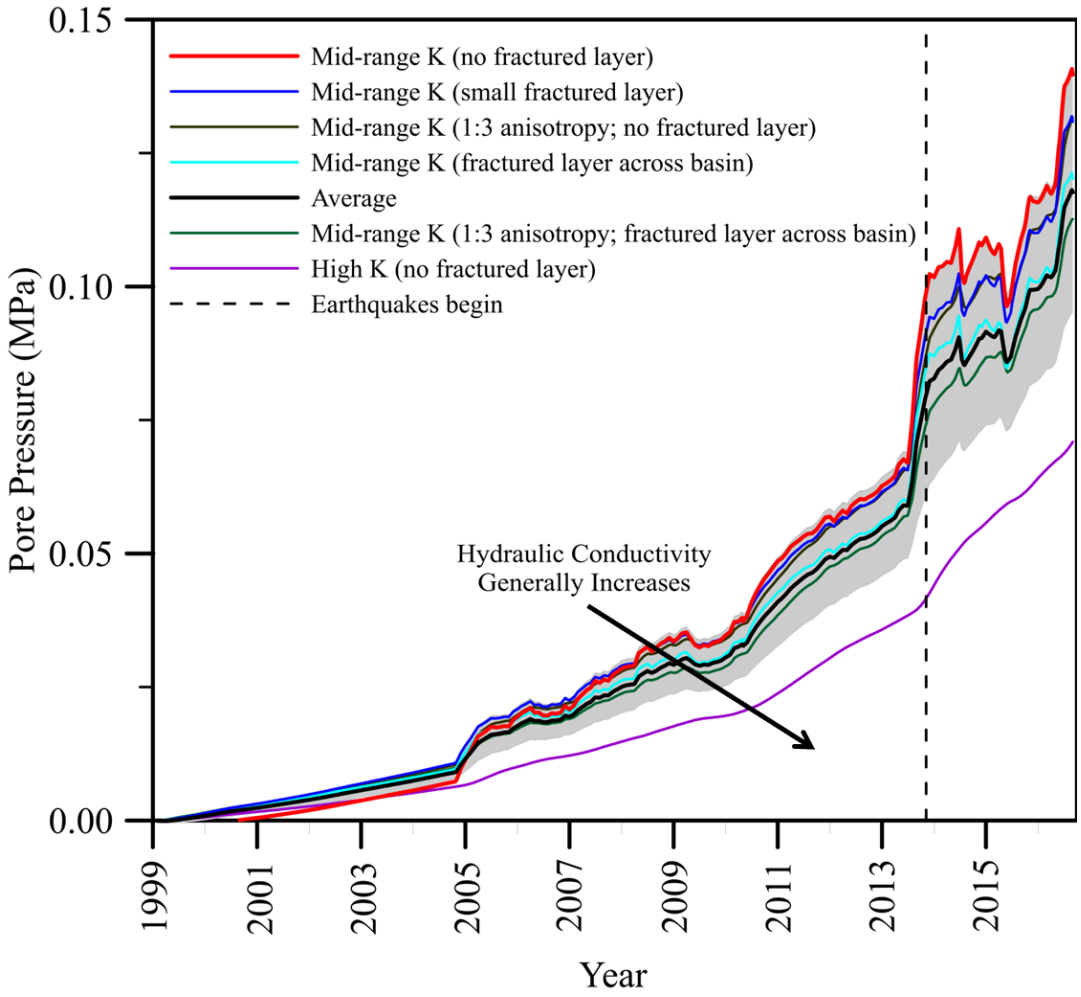

Figure 2.5: Pore pressure change (MPa) through time at a location in the area of seismicity, located at white dot in Figure 2.4d. Colored lines each represent one scenario in the sensitivity analysis. The dark black line represents the average of the pore pressure change and the grey area is +/- one standard deviation. The thicker red line is the model results shown in Figures 2.4 and 2.6. The vertical dashed line is November 2013, when seismicity began.

We also ran the model, using the base case parameters as used to attain the results shown in Figure 2.4, with only the Greeley Wells injecting; only NGL-C4A; and only the Far-field Wells between 15-30 km from the seismicity injecting to determine the relative contribution of these wells to the total pore pressure increase at a single location (shown in Figure 2.4d) near the majority of the earthquakes. The results are presented in Figure 2.6. Figure2.6a shows a pore

pressure increase of approximately 0.10 MPa in November 2013 when all wells within 30 km of radius inject. Figure 2.6b shows that 68% of the pore pressure increase in November 2013 is attributed to the Greeley Wells (which includes NGL-C4A), and 34% of the pore pressure increase in November 2013 is attributed to NGL-C4A alone. Figure 2.6c shows the pore pressure increase caused by injection at the Far-field Wells both from the modeled far-field injection and from subtracting the model results of the only Greeley Wells injecting from the results of all wells injecting (Calculated Far-field). The percentage of the modeled total pore pressure increase due to injection of the Far-field Wells is also presented in Figure 2.6d. The results in Figure 2.6c and 2.6d show a small difference between the modeled and calculated far-field results. We also assess the influence of the well groupings by averaging the percentages of pore pressure increase for each well grouping's modeled results. The Far-field Well grouping's averaged percentage was calculated using the percentage difference between the all well injection model results and the only Greeley Wells injection model results. On average, the Greeley Wells (including NGL-C4A) contribute 56% of the pore pressure, NGL-C4A contributes 28% of the pore pressure, and the Far-field Wells contribute 44% of the pore pressure.

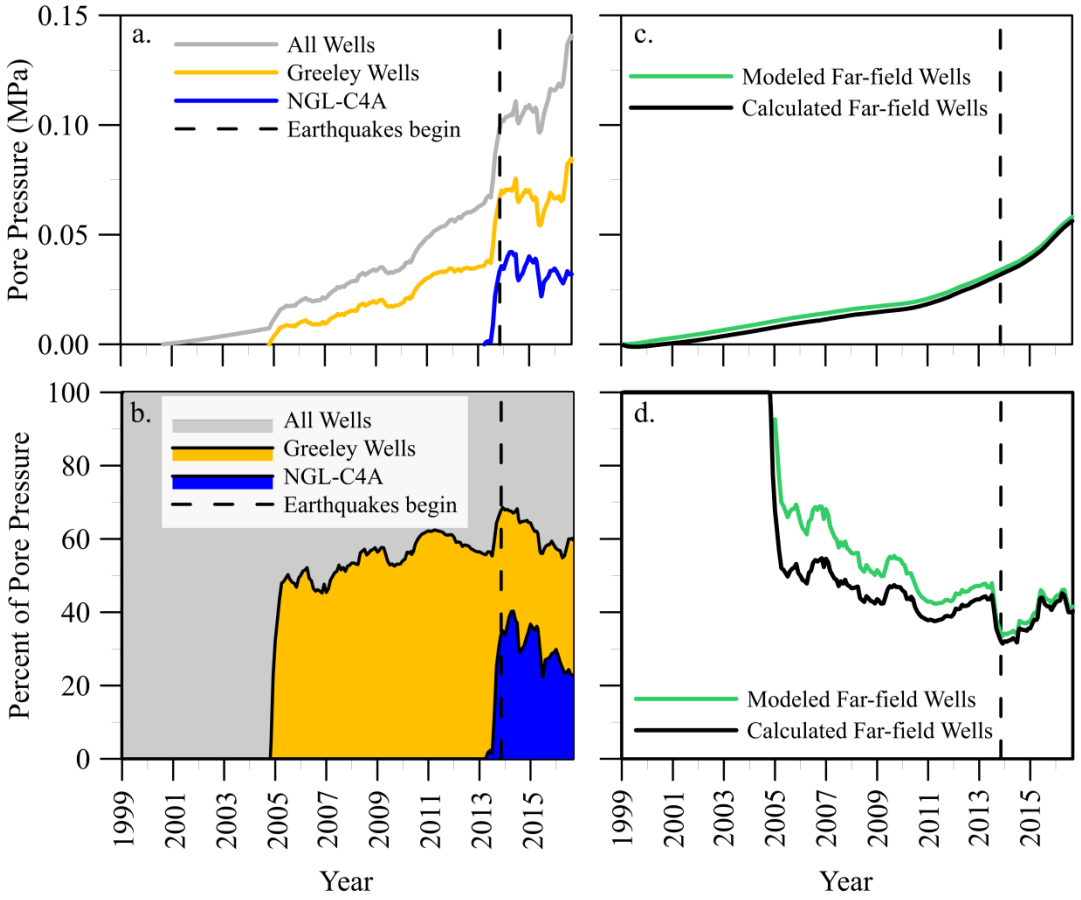

Figure 2.6: Well contributions to pore pressure change at a location in the area of seismicity, located at white dot in Figure 2.4d. (a.) Pore pressure change (MPa) through time for all wells (grey), only Greeley Wells (orange), and only NGL-C4A (blue). (b.) The percent of the total pore pressure change by well grouping. Grey represents 100% of the pore pressure change from all the wells. Orange represents the percent of the total pore pressure change from only the Greeley Wells (within 15 km). Blue represents the percent of the total pore pressure change from only NGL-C4A. (c.) Pore pressure change (MPa) through time for the far-field wells (15 – 30 km from the seismicity). The green line represents the pore pressure change results when only the injection of the far-field wells is modeled. The black line represents the pore pressure change caused by the injection of the far-field wells calculated from the difference between the modeled results for injection of all the wells and modeled results for injection of only the Greeley Wells. (d.) The percent of the total pore pressure change for the far-field wells. The vertical black dashed line is November 2013, when seismicity began.

2.6 Discussion

The pore pressure modeling results show that the pore pressure increase to approximately 0.10 MPa coincided with the commencement of seismicity in November 2013. This pore pressure increase is similar to the suggested triggering threshold in Oklahoma of approximately 0.07 MPa [*Keranen et al.*, 2014]. It is also within the range of pore pressure increase, 0.01 to 0.20 MPa, modeled for Azle, Texas by *Hornbach et al.* [2015]. In addition to studies of induced seismicity, studies of dynamic triggering [e.g. *Hill*, 2008] and Coulomb stress transfer [e.g. *King et al.*, 1994; *Stein*, 1999] indicate that very small changes in stress can promote or prohibit seismicity. If faults in the crust are critically stressed [*Townend and Zoback*, 2000], then a site-specific critical pore pressure change threshold is a reasonable assumption. *Hsieh and Bredehoeft* [1981] also asserted that a critical threshold was consistent with the theory of *Hubbert and Rubey* [1959] on fluid pressure's role on fault mechanics, the theoretical framework used by *Healy et al.* [1968] to explain the mechanism of the Denver earthquakes.

Analysis of the likely *in situ* stress field was not conducted as part of this study due to scarce existing data preventing a thorough mapping of the local stress field. However, the fault movement and orientation is consistent with the regional stress field. *Dart* [1985] found the mean minimum horizontal stress orientation of the Denver-Julesburg Basin to be between N73E and N76E, based on borehole breakouts. The moment tensor solution for the June 2014 M_w 3.2 earthquake shows a normal faulting event with north-northwest striking nodal planes [*Herrmann*, 2016]. Northwest-striking normal faults are consistent with the current stress field.

In 1999 – 2004, prior to the Greeley Wells injecting, pore pressure increases near the seismicity were predicted by the model as less than 0.01 MPa (Figure 2.6a). NGL-C4, almost co-located with NGL-C4A and one of the Greeley Wells (Table 2.2), started injection in October

2004. The injection rate rapidly increased across the area in mid-2009, which leads to an increase in pore pressure near the location of the future seismicity. However, pore pressure did not significantly increase near the area of future seismicity until NGL-C4A began injection in April 2013. The first seismicity in November 2013 and the June 2014 M_w 3.2 earthquake followed the dramatic increase in pore pressure to approximately 0.10 MPa. Pore pressures continue to generally increase from the start of seismicity in November 2013 through the second felt earthquake sequence in August 2016, reaching the model predicted estimate of approximately 0.14 MPa near the location of the seismicity (Figure 2.5 and Figure 2.6a).

From June 2014 to April 2016, the combined injection rates of the Greeley Wells fluctuate, ranging between approximately 220,000 bbls/month to 556,000 bbls/month. Following April 2016, there is a general increase in injection rate until June 2016, when the rate reached a new maximum combined rate of 729,375 bbls/month (Figure 2.2b). The Greeley Wells, including NGL-C4A, account for on average 56% of the pore pressure increase (Figure 2.6b). NGL-C4A alone accounts for on average 28% of the pore pressure increase. Therefore, the six wells near Greeley (not including NGL-C4A) are responsible for on average 28% of the pore pressure increase. The relative contributions to the pore pressure by each grouping of wells are a function of the injection rate and distance from the seismicity. From the modeled results, the Far-field Wells have less influence on the area near seismicity when the Greeley Wells are injecting than when they are not (Figure 2.6c-2.6d). However, the overall influence of the Far-field Wells does not change much whether the Greeley Wells closer to the seismicity are injecting or not.

An interesting observation is that the largest pore pressure increase is not in the area of the seismicity, but farther south near the well with the highest average injection rate during 2016. The reason for the lack of seismicity in the large area of increased pore pressure could be due to

multiple factors. We can speculate that faults on which the seismicity would occur are not present, or not optimally oriented for failure, or not critically stressed.

2.6.1 Reactive Mitigation

Mitigation efforts in Greeley, Colorado following felt earthquakes have focused on individual wells. Following the June 2014 M_w 3.2 earthquake, the operator of NGL-C4A cemented the bottom 500 feet (152.4 m) of the well. Injection resumed in July 2014 at an allowable rate of 5,000 bbls/day (~ 150,000 bbls/month). The rate was increased in steps reaching a rate close to the injection rates prior to the earthquake. The allowable injection rate increased in August 2014 to 7,500 bbls/day (~225,000 bbls/month); in October 2014 to 9,500 bbls/day (~285,000 bbls/month); and in December 2014 to 12,000 bbls/day (~360,000 bbls/month). The actual injection rate at NGL-C4A, between July 2014 and December 2014, did not exceed 288,000 bbls/month.

Since June 2014, the average injection rate at NGL-C4A has decreased, but the injection rate at a nearby Greeley Well, HPD Kersey 1, has stayed consistent. In addition, another operator installed a new well, EWS-2, less than two km from NGL-C4A that started injection in May 2015 and injects at relatively high rates (maximum of ~312,000 bbls/month). In August 2016, a series of felt earthquakes occurred near Greeley [*DYFI*, 2016]. The largest earthquake in the series was a local magnitude (M_L) 2.5 followed by a M_L 2.3 several hours later. After these earthquakes, the COGCC required the operators of the two closest wells to NGL-C4A, EWS-2 and HPD Kersey 1, to plug the bottom of the wells with cement. The bottom 372 feet (~113 m) of EWS-2 was cemented in late August 2016, and the bottom 498 feet (~151.8 m) of HPD Kersey 1 was cemented in October 2016 [*COGCC*, 2016]. Injection resumed at EWS-2 and HPD Kersey 1 directly following the plugging of the bottom of the wells. EWS-2 resumed injection at

a rate of ~160,000 bbls/month, and HPD Kersey 1 resumed injection at a rate of ~82,000 bbls/month [*COGCC*, 2016]. On November 6, 2016, another series of felt earthquakes occurred [*DYFI*, 2016]; the largest of which were two earthquakes five seconds apart, a M_L 2.7 followed by a M_L 3.0.

Based on the occurrence of seismicity that continues, cementing the bottom of the wells has not stopped or reduced seismicity. *Weingarten et al.* [2015] suggested a statistically significant link between injection rate and induced seismicity. Other sites of induced seismicity, e.g. Rocky Mountain Arsenal, Colorado[*Healy et al.*, 1968; *Hsieh and Bredehoeft*, 1981]; Rangely, Colorado [*Raleigh et al.*, 1976]; and Oklahoma sites [*Langenbruch and Zoback*, 2016], have seen reduced seismicity rates with reduction of injection rates. Since over half of the pore pressure increase can be attributed to the Greeley Wells (Figure 2.6b, Table 2.2), reducing the rates at these wells will likely be a more effective approach in minimizing the pore pressure increase and, therefore, reducing the chance of triggering the seismicity. Reducing the rates of wells or larger well spacing overall, therefore effectively reducing the aggregate injection rate, may not be feasible for a variety of reasons. Recommending a specific well spacing or spatially limited injection rate, i.e. an injection rate per square kilometer injection, would be largely site specific and be heavily influenced by the local hydraulic parameters [*Weingarten and Ge*, 2015]. In addition, a thorough cost-benefit analysis would be needed to determine if the well spacing and injection rate limitations were possible.

2.7 Conclusions

Pore pressure modeling shows that the Greeley area seismicity began after the pore pressure increase reached approximately 0.10 MPa in the area of activity. The largest contribution to pore pressure increase, on average 56% in the area of seismicity, is from the

seven Greeley Wells that are within 15 km of the seismic area. However, the wells between 15 and 30 km of the center of seismicity still contributed a substantial portion, on average 44%, of the pore pressure increase near the seismicity. Our results show not only the influence of injection on pore pressure at short distances from the earthquakes, but also the significant contribution to pore pressure change by injection at all distances modeled, up to 30 km, from the earthquakes.

Our modeling shows that pore pressure increase from injection could reach 0.15 MPa without a permeable pathway such as a fault or fractured zone. This magnitude of pore pressure increase has been shown in other studies to be sufficient to induce seismicity [*Keranen et al.*, 2014; *Hornbach et al.*, 2015; *Ogwari and Horton*, 2016]. In addition, sensitivity analysis of hydraulic conductivity shows pore pressure in the area of seismicity could increase to a level that induces earthquakes for the range of hydraulic conductivity in the area.

The local seismic network continues to detect seismicity in the area despite mitigation efforts, such as the cementing of the bottom of the injection interval. Our model results indicate the pore pressure continues to increase with continued injection near the seismicity. Mitigation by cementing wells in Greeley has been ineffective in reducing the number or magnitude of earthquakes. Since over 50% of the pore pressure increase in the area of seismicity can be attributed to the Greeley Wells, a more effective approach may include reduction of injection rates at these wells. Furthermore, the Far-field Wells between 15 and 30 km from the seismicity contribute approximately 44% of the pore pressure increase. This is a significant portion of the total increase in pore pressure. An appropriate preventative mitigation action may include larger spacing between wells. Farther well spacing would reduce the number of wells within a prescribed distance such that the spatial aggregation of the injection rate would be much smaller.

Mitigating induced seismicity may require hard decisions about economic and physical feasibility. A cost-benefit analysis of the number of wells, well spacing, and injection rate limitation would be necessary to examine the feasibility of various scenarios.

2.8 Data

Table 2.3 contains constant-head permeameter test results from tests done using a Trautwein M100000 Standard Panel permeameter on samples from the Horsetooth Reservoir (HR samples) and Owl Canyon, CO (OC samples) areas (see Figure 2.1 for locations). First, the samples were saturated with 30-50 milliliters (mL) of water. Second, up to 10 tests were run using approximately 20 mL of water each. All tests were completed using tap water at room temperature.

Table 2.4 contains constant-head permeameter test results from tests on samples from core (CRC Library Code E053). Data is also available on the CRC website [*USGS CRC*, 2016].

Table 2.3: Outcrop samples constant-head permeameter test results [1]

Sample	Test	Diameter (cm)	Area (cm^2)	Length (cm)	Total Volume (mL)	Time (s)	Pressure (psi)	head (cm)	Q (cm^3/s)	K (cm/s)	K (m/s)
OC1-1	1	2.7	5.7	4.2	120.42	6.24E+02	9.40	660.89	1.93E-01	2.14E-04	2.14E-06
Ingleside	2				106.68	4.63E+02	9.60	674.95	2.30E-01	2.51E-04	2.51E-06
Formation	3				120.42	5.58E+02	10.00	703.07	2.16E-01	2.25E-04	2.25E-06
	4				138.02	5.55E+02	10.10	710.10	2.49E-01	2.57E-04	2.57E-06
	5				113.60	5.34E+02	9.40	660.89	2.13E-01	2.36E-04	2.36E-06
	6				115.87	6.05E+02	9.40	660.89	1.91E-01	2.12E-04	2.12E-06
	7				112.36	5.39E+02	9.40	660.89	2.08E-01	2.31E-04	2.31E-06
	8				125.53	5.27E+02	10.00	703.07	2.38E-01	2.48E-04	2.48E-06
	9				123.82	4.79E+02	10.00	703.07	2.59E-01	2.70E-04	2.70E-06
	10				126.10	4.64E+02	10.10	710.10	2.72E-01	2.81E-04	2.81E-06
HR1-3H	SAT	2.7	5.7	3.3	72.70	3.60E+02	10.10	710.10	2.02E-01	1.64E-04	1.64E-06
Fountain	1				33.98	1.80E+02	10.10	710.10	1.89E-01	1.53E-04	1.53E-06
Formation	2				34.08	2.40E+02	10.10	710.10	1.42E-01	1.15E-04	1.15E-06
	3				34.08	2.17E+02	10.10	710.10	1.57E-01	1.27E-04	1.27E-06
	4				34.08	2.14E+02	10.10	710.10	1.59E-01	1.29E-04	1.29E-06
HR1-4	SAT	2.7	5.7	3.2	97.03	3.30E+05	10.10	710.10	2.94E-04	2.31E-07	2.31E-09
Fountain	1				45.44	1.73E+05	10.10	710.10	2.63E-04	2.07E-07	2.07E-09
Formation	2				45.44	1.89E+05	10.10	710.10	2.41E-04	1.89E-07	1.89E-09
	3				75.54	3.19E+05	10.10	710.10	2.37E-04	1.87E-07	1.87E-09
	4				28.40	1.16E+05	10.10	710.10	2.45E-04	1.93E-07	1.93E-09
	5				51.69	1.71E+05	10.10	710.10	3.02E-04	2.37E-07	2.37E-09
	6				105.65	3.31E+05	10.10	710.10	3.19E-04	2.51E-07	2.51E-09
	7				55.10	1.77E+05	10.10	710.10	3.12E-04	2.45E-07	2.45E-09
	8				31.14	9.56E+04	10.10	710.10	3.26E-04	2.56E-07	2.56E-09
	9				103.38	3.30E+05	10.10	710.10	3.13E-04	2.47E-07	2.47E-09
	10				56.80	1.78E+05	10.10	710.10	3.18E-04	2.51E-07	2.51E-09

Sample	Test	Diameter (cm)	Area (cm^2)	Length (cm)	Total Volume (mL)	Time (s)	Pressure (psi)	head (cm)	Q (cm^3/s)	K (cm/s)	K (m/s)
HR1-3V	SAT	2.7	5.7	3.2	63.31	1.07E+05	10.10	710.10	5.91E-04	4.66E-07	4.66E-09
Fountain	1				25.32	8.15E+04	10.10	710.10	3.11E-04	2.45E-07	2.45E-09
Formation	2				36.91	2.62E+05	10.10	710.10	1.41E-04	1.11E-07	1.11E-09
	3				28.25	2.74E+05	10.10	710.10	1.03E-04	8.13E-08	8.13E-10
	4				37.99	4.07E+05	10.10	710.10	9.34E-05	7.35E-08	7.35E-10
	5				23.38	2.87E+05	10.10	710.10	8.14E-05	6.40E-08	6.40E-10
	6				34.09	5.08E+05	10.10	710.10	6.70E-05	5.28E-08	5.28E-10
	7				46.27	8.52E+05	10.10	710.10	5.43E-05	4.27E-08	4.27E-10
	8				19.97	2.72E+05	10.10	710.10	7.35E-05	5.79E-08	5.79E-10
HR1-1H	SAT	2.7	5.7	4.2	82.79	8.63E+04	10.10	710.10	9.59E-04	9.91E-07	9.91E-09
Fountain	1				91.56	8.68E+04	10.10	710.10	1.06E-03	1.09E-06	1.09E-08
Formation	2				92.53	8.55E+04	10.10	710.10	1.08E-03	1.12E-06	1.12E-08
	3				94.97	8.70E+04	10.10	710.10	1.09E-03	1.13E-06	1.13E-08
	4				94.97	8.69E+04	10.10	710.10	1.09E-03	1.13E-06	1.13E-08
	5				85.23	8.56E+04	10.10	710.10	9.96E-04	1.03E-06	1.03E-08
	6				82.79	8.20E+04	10.10	710.10	1.01E-03	1.04E-06	1.04E-08
	7				81.82	8.82E+04	10.10	710.10	9.28E-04	9.58E-07	9.58E-09
HR2-3V	SAT	2.7	5.7	2.8	29.22	5.09E+05	10.10	710.10	5.74E-05	3.95E-08	3.95E-10
Lyons	1				15.58	5.28E+05	10.10	710.10	2.95E-05	2.03E-08	2.03E-10
Formation	2				16.07	5.10E+05	10.10	710.10	3.15E-05	2.17E-08	2.17E-10
	3				26.79	1.13E+06	10.10	710.10	2.37E-05	1.63E-08	1.63E-10
	4				17.53	7.59E+05	10.10	710.10	2.31E-05	1.59E-08	1.59E-10
	5				13.64	5.36E+05	10.10	710.10	2.54E-05	1.75E-08	1.75E-10
	6				17.53	7.74E+05	10.10	710.10	2.27E-05	1.56E-08	1.56E-10
	7				18.99	6.87E+05	10.10	710.10	2.77E-05	1.90E-08	1.90E-10
	8				21.43	7.87E+05	10.10	710.10	2.72E-05	1.87E-08	1.87E-10
	9				17.05	5.99E+05	10.10	710.10	2.85E-05	1.96E-08	1.96E-10
	10				18.51	5.24E+05	10.10	710.10	3.53E-05	2.43E-08	2.43E-10

Sample	Test	Diameter (cm)	Area (cm^2)	Length (cm)	Total Volume (mL)	Time (s)	Pressure (psi)	head (cm)	Q (cm^3/s)	K (cm/s)	K (m/s)
HR2-1H	SAT	2.7	5.7	3.6	82.79	8.63E+04	10.10	710.10	9.59E-04	8.49E-07	8.49E-09
Lyons	1				91.56	8.66E+04	10.10	710.10	1.06E-03	9.36E-07	9.36E-09
Formation	2				92.53	8.54E+04	10.10	710.10	1.08E-03	9.59E-07	9.59E-09
	3				94.97	8.70E+04	10.10	710.10	1.09E-03	9.67E-07	9.67E-09
	4				94.97	8.68E+04	10.10	710.10	1.09E-03	9.69E-07	9.69E-09
	5				85.23	8.56E+04	10.10	710.10	9.96E-04	8.82E-07	8.82E-09
	6				82.79	8.20E+04	10.10	710.10	1.01E-03	8.94E-07	8.94E-09
	7				81.82	8.82E+04	10.10	710.10	9.28E-04	8.21E-07	8.21E-09
	SAT				47.24	9.12E+04	10.10	710.10	5.18E-04	4.59E-07	4.59E-09
	8				47.73	1.67E+05	10.10	710.10	2.86E-04	2.53E-07	2.53E-09
	9				29.71	8.40E+04	10.10	710.10	3.54E-04	3.13E-07	3.13E-09

[1] cm = centimeter; mL = milliliter; s = seconds; psi = pounds per square inch; SAT = saturation part of tests. In sample names, letter abbreviations and numbers give the sample locations; and V and H in sample names represent vertical or horizontal samples.

Table 2.4: Core CRC Library Code E053 samples constant-head permeameter test results [1]

Sample	Test	Diameter (cm)	Area (cm^2)	Length (cm)	Total Volume (mL)	Time (s)	Pressure (psi)	head (cm)	Q (cm^3/s)	K (cm/s)	K (m/s)
9175H	SAT	2.5	4.9	3.6	99.89	1.96E+03	10.10	710.10	5.09E-02	5.25E-05	5.25E-07
Lyons	1				63.70	1.76E+03	10.10	710.10	3.61E-02	3.73E-05	3.73E-07
Formation	2				98.37	2.51E+03	10.10	710.10	3.92E-02	4.05E-05	4.05E-07
	3				90.48	2.11E+03	10.10	710.10	4.30E-02	4.44E-05	4.44E-07
	4				71.00	1.80E+03	10.20	717.13	3.94E-02	4.03E-05	4.03E-07
	5				83.66	2.02E+03	10.10	710.10	4.14E-02	4.27E-05	4.27E-07
	6				93.50	1.95E+03	10.10	710.10	4.78E-02	4.94E-05	4.94E-07
	7				70.03	1.68E+03	10.10	710.10	4.17E-02	4.31E-05	4.31E-07
	8				59.31	1.82E+03	10.10	710.10	3.26E-02	3.37E-05	3.37E-07
	9				65.85	2.27E+03	10.10	710.10	2.90E-02	2.99E-05	2.99E-07
	10				62.72	2.22E+03	10.10	710.10	2.82E-02	2.92E-05	2.92E-07
9175V	1	2.5	4.9	3.3	36.79	6.59E+03	10.20	717.13	5.58E-03	5.23E-06	5.23E-08
Lyons	2				39.25	6.26E+03	10.20	717.13	6.27E-03	5.87E-06	5.87E-08
Formation	3				22.35	4.47E+03	10.20	717.13	5.00E-03	4.69E-06	4.69E-08
	4				20.70	3.85E+03	10.10	710.10	5.37E-03	5.09E-06	5.09E-08
	5				20.35	3.57E+03	10.10	710.10	5.70E-03	5.40E-06	5.40E-08
	6				23.76	3.11E+03	10.10	710.10	7.64E-03	7.23E-06	7.23E-08
	7				28.25	3.73E+03	10.10	710.10	7.58E-03	7.18E-06	7.18E-08
	8				26.30	3.55E+03	10.10	710.10	7.41E-03	7.01E-06	7.01E-08
	9				25.52	3.56E+03	10.10	710.10	7.17E-03	6.79E-06	6.79E-08
	10				30.68	4.12E+03	10.10	710.10	7.45E-03	7.05E-06	7.05E-08

Sample	Test	Diameter (cm)	Area (cm^2)	Length (cm)	Total Volume (mL)	Time (s)	Pressure (psi)	head (cm)	Q (cm^3/s)	K (cm/s)	K (m/s)
9203H	SAT	2.5	4.9	2.2	26.74	5.95E+04	10.10	710.10	4.49E-04	2.83E-07	2.83E-09
Lyons	SAT				36.09	2.91E+05	10.10	710.10	1.24E-04	7.83E-08	7.83E-10
Formation	SAT_Total				62.82	3.50E+05	10.10	710.10	1.79E-04	1.13E-07	1.13E-09
	1				38.86	3.55E+05	10.10	710.10	1.09E-04	6.90E-08	6.90E-10
	2				80.26	8.36E+05	10.10	710.10	9.60E-05	6.06E-08	6.06E-10
	3				32.04	3.37E+05	10.10	710.10	9.51E-05	6.00E-08	6.00E-10
	4				28.73	2.89E+05	10.10	710.10	9.95E-05	6.28E-08	6.28E-10
	5				32.63	3.18E+05	10.10	710.10	1.02E-04	6.47E-08	6.47E-10
	6				19.48	7.07E+04	10.10	710.10	2.75E-04	1.74E-07	1.74E-09
9463H	SAT	2.5	4.9	3.6	39.19	4.34E+05	10.10	710.10	9.03E-05	9.33E-08	9.33E-10
Wolfcamp	1				34.65	6.96E+05	10.10	710.10	4.98E-05	5.14E-08	5.14E-10
Formation	2				30.76	5.11E+05	10.10	710.10	6.02E-05	6.21E-08	6.21E-10
	3				60.78	5.23E+05	10.10	710.10	1.16E-04	1.20E-07	1.20E-09
	4				59.07	3.44E+05	10.10	710.10	1.72E-04	1.77E-07	1.77E-09
	5				34.08	1.69E+05	10.10	710.10	2.01E-04	2.08E-07	2.08E-09
	6				44.87	1.73E+05	10.10	710.10	2.60E-04	2.69E-07	2.69E-09
	7				42.03	1.71E+05	10.10	710.10	2.45E-04	2.53E-07	2.53E-09
	8				40.33	2.60E+05	10.10	710.10	1.55E-04	1.60E-07	1.60E-09
	9				36.35	2.64E+05	10.10	710.10	1.38E-04	1.42E-07	1.42E-09
	10				58.50	4.39E+05	10.10	710.10	1.33E-04	1.38E-07	1.38E-09

Sample	Test	Diameter (cm)	Area (cm^2)	Length (cm)	Total Volume (mL)	Time (s)	Pressure (psi)	head (cm)	Q (cm^3/s)	K (cm/s)	K (m/s)
9463V	SAT	2.5	4.9	4.0	54.54	3.49E+05	10.10	710.10	1.56E-04	1.79E-07	1.79E-09
Wolfcamp	1				33.60	2.55E+05	10.10	710.10	1.32E-04	1.51E-07	1.51E-09
Formation	2				58.93	5.30E+05	10.10	710.10	1.11E-04	1.28E-07	1.28E-09
	3				25.81	2.54E+05	10.10	710.10	1.01E-04	1.16E-07	1.16E-09
	4				36.53	3.43E+05	10.10	710.10	1.06E-04	1.22E-07	1.22E-09
	5				16.07	1.77E+05	10.10	710.10	9.10E-05	1.04E-07	1.04E-09
	6				37.01	3.42E+05	10.10	710.10	1.08E-04	1.24E-07	1.24E-09
	7				34.09	3.30E+05	10.10	710.10	1.03E-04	1.19E-07	1.19E-09
	8				61.36	3.61E+05	10.10	710.10	1.70E-04	1.95E-07	1.95E-09
	9				36.04	1.72E+05	10.10	710.10	2.10E-04	2.41E-07	2.41E-09
	10				104.22	4.27E+05	10.10	710.10	2.44E-04	2.80E-07	2.80E-09
9536H	SAT	2.5	4.9	3	56.49	1.12E+03	10.10	710.10	5.05E-02	4.34E-05	4.34E-07
Wolfcamp	1				36.43	9.95E+02	10.10	710.10	3.66E-02	3.15E-05	3.15E-07
Formation	2				77.33	2.06E+03	10.10	710.10	3.75E-02	3.22E-05	3.22E-07
	3				76.70	1.81E+03	10.10	710.10	4.24E-02	3.65E-05	3.65E-07
	4				78.60	2.01E+03	10.10	710.10	3.91E-02	3.36E-05	3.36E-07
	5				99.25	2.42E+03	10.10	710.10	4.09E-02	3.52E-05	3.52E-07
	6				80.26	1.90E+03	10.10	710.10	4.22E-02	3.64E-05	3.64E-07
	7				98.27	2.45E+03	10.10	710.10	4.01E-02	3.45E-05	3.45E-07
	8				65.65	1.55E+03	10.10	710.10	4.24E-02	3.65E-05	3.65E-07
	9				61.26	1.33E+03	10.10	710.10	4.60E-02	3.96E-05	3.96E-07
	10				58.83	1.29E+03	10.10	710.10	4.57E-02	3.93E-05	3.93E-07

Sample	Test	Diameter (cm)	Area (cm^2)	Length (cm)	Total Volume (mL)	Time (s)	Pressure (psi)	head (cm)	Q (cm^3/s)	K (cm/s)	K (m/s)
9878.5V	SAT	2.5	4.9	2.3	47.24	8.14E+03	10.10	710.10	5.81E-03	3.83E-06	3.83E-08
Ingleside	1				36.23	2.82E+04	10.10	710.10	1.29E-03	8.49E-07	8.49E-09
Formation	2				73.05	5.27E+04	10.10	710.10	1.39E-03	9.14E-07	9.14E-09
	3				47.24	2.81E+04	10.10	710.10	1.68E-03	1.11E-06	1.11E-08
	4				98.27	6.52E+04	10.10	710.10	1.51E-03	9.95E-07	9.95E-09
	5				25.03	1.61E+04	10.10	710.10	1.56E-03	1.03E-06	1.03E-08
	6				91.46	6.97E+04	10.10	710.10	1.31E-03	8.66E-07	8.66E-09
	7				35.74	2.68E+04	10.10	710.10	1.34E-03	8.81E-07	8.81E-09
	8				77.33	6.41E+04	10.10	710.10	1.21E-03	7.96E-07	7.96E-09
	9				29.12	2.27E+04	10.10	710.10	1.28E-03	8.45E-07	8.45E-09
	10				41.30	2.30E+04	10.10	710.10	1.79E-03	1.18E-06	1.18E-08
9895H	SAT	2.5	4.9	3.5	98.86	5.26E+02	10.10	710.10	1.88E-01	1.89E-04	1.89E-06
Ingleside	1				59.41	2.86E+02	10.10	710.10	2.08E-01	2.08E-04	2.08E-06
Formation	2				56.49	2.84E+02	10.10	710.10	1.99E-01	1.99E-04	1.99E-06
	3				59.80	3.08E+02	10.10	710.10	1.94E-01	1.95E-04	1.95E-06
	4				44.32	2.42E+02	10.10	710.10	1.83E-01	1.84E-04	1.84E-06
	5				39.93	2.09E+02	10.10	710.10	1.91E-01	1.91E-04	1.91E-06
	6				37.99	2.10E+02	10.10	710.10	1.81E-01	1.82E-04	1.82E-06
	7				39.45	2.32E+02	10.10	710.10	1.70E-01	1.71E-04	1.71E-06
	8				38.37	2.15E+02	10.10	710.10	1.78E-01	1.79E-04	1.79E-06
	9				37.99	2.34E+02	10.10	710.10	1.62E-01	1.63E-04	1.63E-06
	10				38.86	2.46E+02	10.10	710.10	1.58E-01	1.59E-04	1.59E-06

Sample	Test	Diameter (cm)	Area (cm^2)	Length (cm)	Total Volume (mL)	Time (s)	Pressure (psi)	head (cm)	Q (cm^3/s)	K (cm/s)	K (m/s)
9895V	SAT	2.5	4.9	1.4	75.87	1.16E+03	10.10	710.10	6.52E-02	2.62E-05	2.62E-07
Ingleside	1				61.75	1.10E+03	10.10	710.10	5.62E-02	2.26E-05	2.26E-07
Formation	2				57.85	1.29E+03	10.10	710.10	4.47E-02	1.80E-05	1.80E-07
	3				47.19	1.28E+03	10.10	710.10	3.70E-02	1.49E-05	1.49E-07
	4				47.14	1.57E+03	10.10	710.10	3.01E-02	1.21E-05	1.21E-07
	5				47.14	2.08E+03	10.10	710.10	2.26E-02	9.09E-06	9.09E-08
	6				32.14	2.21E+03	10.10	710.10	1.46E-02	5.85E-06	5.85E-08
	7				27.76	2.24E+03	10.10	710.10	1.24E-02	4.97E-06	4.97E-08
	8				22.79	1.59E+03	10.10	710.10	1.43E-02	5.74E-06	5.74E-08
	9				17.92	1.58E+03	10.10	710.10	1.14E-02	4.56E-06	4.56E-08
	10				62.34	5.62E+03	10.10	710.10	1.11E-02	4.45E-06	4.45E-08
10010.5V	SAT	2.5	4.9	2.6	42.50	8.64E+04	10.10	710.10	4.92E-04	3.67E-07	3.67E-09
Ingleside	1				29.64	8.65E+04	10.10	710.10	3.43E-04	2.55E-07	2.55E-09
Formation	2				30.39	8.99E+04	10.10	710.10	3.38E-04	2.52E-07	2.52E-09
	3				93.72	2.52E+05	10.10	710.10	3.72E-04	2.78E-07	2.78E-09
	4				30.10	8.99E+04	10.10	710.10	3.35E-04	2.50E-07	2.50E-09
	5				34.08	8.58E+04	10.10	710.10	3.97E-04	2.96E-07	2.96E-09
	6				31.81	8.68E+04	10.10	710.10	3.67E-04	2.73E-07	2.73E-09
	7				31.24	8.66E+04	10.10	710.10	3.61E-04	2.69E-07	2.69E-09
	8				25.56	7.03E+04	10.10	710.10	3.63E-04	2.71E-07	2.71E-09
	9				130.07	3.61E+05	10.10	710.10	3.60E-04	2.69E-07	2.69E-09
	10				57.94	1.71E+05	10.10	710.10	3.39E-04	2.53E-07	2.53E-09

Sample	Test	Diameter (cm)	Area (cm^2)	Length (cm)	Total Volume (mL)	Time (s)	Pressure (psi)	head (cm)	Q (cm^3/s)	K (cm/s)	K (m/s)
10029H	SAT	2.5	4.9	4.3	26.70	9.44E+04	10.10	710.10	2.83E-04	3.49E-07	3.49E-09
Ingleside	1				21.58	7.55E+04	10.10	710.10	2.86E-04	3.52E-07	3.52E-09
Formation	2				43.74	1.87E+05	10.10	710.10	2.34E-04	2.88E-07	2.88E-09
	3				17.04	9.35E+04	10.10	710.10	1.82E-04	2.25E-07	2.25E-09
	4				25.56	1.49E+05	10.10	710.10	1.71E-04	2.11E-07	2.11E-09
	5				46.58	2.73E+05	10.10	710.10	1.71E-04	2.10E-07	2.10E-09
	6				14.20	8.70E+04	10.10	710.10	1.63E-04	2.01E-07	2.01E-09
10029V	SAT	2.5	4.9	4.6	18.18	9.13E+04	10.10	710.10	1.99E-04	2.63E-07	2.63E-09
Ingleside	1				30.67	9.00E+04	10.10	710.10	3.41E-04	4.50E-07	4.50E-09
Formation	2				75.54	9.51E+04	10.10	710.10	7.94E-04	1.05E-06	1.05E-08
	3				22.72	7.66E+04	10.10	710.10	2.97E-04	3.91E-07	3.91E-09
	4				86.34	1.77E+05	10.10	710.10	4.89E-04	6.45E-07	6.45E-09
	5				24.99	1.00E+05	10.10	710.10	2.49E-04	3.29E-07	3.29E-09
10165H	SAT	2.5	4.9	5.2	40.42	2.63E+05	10.10	710.10	1.54E-04	2.29E-07	2.29E-09
Fountain	1				29.22	1.93E+05	10.10	710.10	1.52E-04	2.26E-07	2.26E-09
Formation	2				27.66	1.60E+05	10.10	710.10	1.73E-04	2.59E-07	2.59E-09
	3				43.44	2.52E+05	10.10	710.10	1.72E-04	2.57E-07	2.57E-09
	4				32.14	1.73E+05	10.10	710.10	1.86E-04	2.78E-07	2.78E-09
	5				81.82	3.51E+05	10.10	710.10	2.33E-04	3.48E-07	3.48E-09
	SAT				65.75	1.62E+05	10.10	710.10	4.06E-04	6.06E-07	6.06E-09
	6				50.16	8.91E+04	10.10	710.10	5.63E-04	8.40E-07	8.40E-09
	7				51.62	8.04E+04	10.10	710.10	6.42E-04	9.58E-07	9.58E-09
	8				54.06	9.15E+04	10.10	710.10	5.91E-04	8.81E-07	8.81E-09
	9				53.57	8.09E+04	10.10	710.10	6.62E-04	9.87E-07	9.87E-09

Sample	Test	Diameter (cm)	Area (cm^2)	Length (cm)	Total Volume (mL)	Time (s)	Pressure (psi)	head (cm)	Q (cm^3/s)	K (cm/s)	K (m/s)
10165V	SAT	2.5	4.9	3.2	1.87	8.50E+04	10.10	710.10	2.20E-05	2.02E-08	2.02E-10
Fountain	SAT				3.44	1.56E+05	10.10	710.10	2.20E-05	2.02E-08	2.02E-10
Formation	SAT				1.70	9.19E+04	10.10	710.10	1.85E-05	1.70E-08	1.70E-10
	SAT				1.70	8.17E+04	10.10	710.10	2.09E-05	1.92E-08	1.92E-10
	SAT				1.80	8.50E+04	10.10	710.10	2.12E-05	1.95E-08	1.95E-10
	SAT				1.94	7.28E+04	10.10	710.10	2.66E-05	2.44E-08	2.44E-10
	SAT				2.27	1.04E+05	10.10	710.10	2.18E-05	2.00E-08	2.00E-10
	SAT				4.88	2.37E+05	10.10	710.10	2.06E-05	1.89E-08	1.89E-10
	SAT				2.27	1.09E+05	10.10	710.10	2.08E-05	1.91E-08	1.91E-10
	SAT				2.17	7.94E+04	10.10	710.10	2.73E-05	2.51E-08	2.51E-10
	SAT				2.27	9.67E+04	10.10	710.10	2.35E-05	2.16E-08	2.16E-10
	SAT				1.70	8.69E+04	10.10	710.10	1.96E-05	1.80E-08	1.80E-10
	SAT				5.68	2.35E+05	10.10	710.10	2.42E-05	2.22E-08	2.22E-10
	SAT				22.15	8.73E+05	10.10	710.10	2.54E-05	2.33E-08	2.33E-10
	1				21.92	6.16E+05	10.10	710.10	3.56E-05	3.27E-08	3.27E-10
	2				18.84	4.36E+05	10.10	710.10	4.32E-05	3.97E-08	3.97E-10
	3				19.78	2.71E+05	10.10	710.10	7.30E-05	6.70E-08	6.70E-10
	4				30.00	2.35E+05	10.10	710.10	1.28E-04	1.17E-07	1.17E-09
	5				33.04	2.89E+05	10.10	710.10	1.14E-04	1.05E-07	1.05E-09
	6				48.18	2.81E+05	10.10	710.10	1.72E-04	1.58E-07	1.58E-09
	7				12.50	7.09E+04	10.10	710.10	1.76E-04	1.62E-07	1.62E-09
	8				111.90	6.27E+05	10.10	710.10	1.79E-04	1.64E-07	1.64E-09

Sample	Test	Diameter (cm)	Area (cm^2)	Length (cm)	Total Volume (mL)	Time (s)	Pressure (psi)	head (cm)	Q (cm^3/s)	K (cm/s)	K (m/s)
10511V	SAT	2.5	4.9	3.9	21.02	2.50E+05	10.10	710.10	8.42E-05	9.42E-08	9.42E-10
Fountain	1				21.02	6.14E+05	10.10	710.10	3.42E-05	3.83E-08	3.83E-10
Formation	2				21.58	7.79E+05	10.10	710.10	2.77E-05	3.10E-08	3.10E-10
	3				18.18	7.59E+05	10.10	710.10	2.40E-05	2.68E-08	2.68E-10
	4				21.58	8.81E+05	10.10	710.10	2.45E-05	2.74E-08	2.74E-10
	5				19.88	1.12E+06	10.10	710.10	1.78E-05	1.99E-08	1.99E-10
	6				26.13	1.39E+06	10.10	710.10	1.89E-05	2.11E-08	2.11E-10
	7				13.63	5.24E+05	10.10	710.10	2.60E-05	2.91E-08	2.91E-10

[1] cm = centimeter; mL = milliliter; s = seconds; psi = pounds per square inch; SAT = saturation part of tests. Number in sample name is the depth the same was taken from (in feet) and V and H in sample names represents vertical or horizontal samples.

CHAPTER 3: A SIMPLE RELATION TO CONSTRAIN PORE PRESSURE MODELS USING SURFACE DEFORMATION

Abstract

A simple relation between pore pressure change and 1D surface deformation is presented. The relation is for pore pressure change in a confined aquifer that causes surface deformation. It can be applied to pore pressure models of any discretization and is computationally efficient. The estimated surface deformation from model results can be compared to observed surface deformation through geodetic techniques such a Differential Synthetic Aperture Radar (DInSAR). Model parameters then are constrained using the observed surface deformation. The validity of this relation is shown through constraint of model parameters for surface uplift due to pore pressure increase caused by wastewater disposal injection.

3.1 Introduction

Constraining hydrologic parameters in pore pressure modeling is crucial to model results that are representative of the actual system. Obtaining direct measurements of hydraulic parameters for pore pressure models is often difficult. Deep confined aquifers, especially those used for wastewater disposal of produced water from oil and gas extraction, have limited accessibility and few direct measurements of hydraulic parameters are available. Pore pressure models in situations of injection-induced seismicity are important to determine the cause of induced seismicity and plan mitigation strategies. In these models, literature values are frequently used for the specific aquifer formation or type of formation [e.g. *Keranen et al.,* 2014; *Brown and Liu,* 2016]. Some injection-induced seismicity areas may have core samples available for laboratory testing [e.g. *Brown et al.,* 2017]. In selected cases, induced seismicity sites may have well tests for the aquifer of interest that can be used to estimate hydraulic properties [e.g. *Hornbach et al.,* 2015; *Ogwari and Horton,* 2016; *Brown et al.,* 2017].

Surface deformation can be a physical manifestation of pore pressure changes in the subsurface [*Teatini et al.,* 2011]. When pore pressure increases within a confined aquifer, the aquifer skeleton expands resulting in surface uplift. Surface deformation is observed using a number of techniques including leveling data [e.g. *Bell et al.,* 2002], global positioning system (GPS) [e.g. *Ishitsuka et al.,* 2017], tilt-meters [e.g. *Jahr et al.,* 2008], and remote sensing like Differential Synthetic Aperture Radar (DInSAR) [e.g. *Shirzaei et al.,* 2016; *Barba-Sevilla et al.,* 2018]. Uplift on the order of millimeters to centimeters has been observed using DInSAR in multiple areas [e.g. *Shirzaei et al.,* 2016; *Barba-Sevilla et al.,* 2018; *Kim and Lu,* 2018; *Loesch and Sagan,* 2018] of wastewater disposal injection related to oil and gas activities. Interferograms are created by co-registering two SAR images of similar imaging geometries.

DInSAR relies on calculating phase differences from two or more passes of the SAR satellite to quantify surface displacement. DInSAR can provide both cumulative deformation and time series of deformation over a broad spatial area with centimeter or better resolution.

When considering areas of wastewater disposal, production in the vicinity must also be considered as a mechanism of surface deformation. However, if the oil and gas production is mostly enhanced oil recovery, where fluids are injected into the subsurface to increase the hydrocarbons flowing into production wells, then the surface deformation from production can be assumed to be negligible. A goal of the enhanced oil recovery is to keep the pressure in the production zone constant [*Rubinstein and Mahani*, 2015]. The amount of fluids being injected into the production zone is assumed to be almost equal to the amount being extracted due to production. Therefore, the surface deformation is caused primarily by the wastewater injection (Figure 3.1).

Surface deformation has been used to estimate hydraulic parameters for aquifer systems where water level measurements are scarce [*Hu et al.*, 2018]. *Rinaldi et al.* [2017] used inverse modeling of surface uplift to determine mechanical and hydraulic properties at the CO_2 injection site at In Salah, Algeria. In their study, *Rinaldi et al.* [2017] use iTOUGH-PEST and TOUGH-FLAC for the inverse modeling. While this type of inverse modeling can help constrain parameters, it has a very high computational cost.

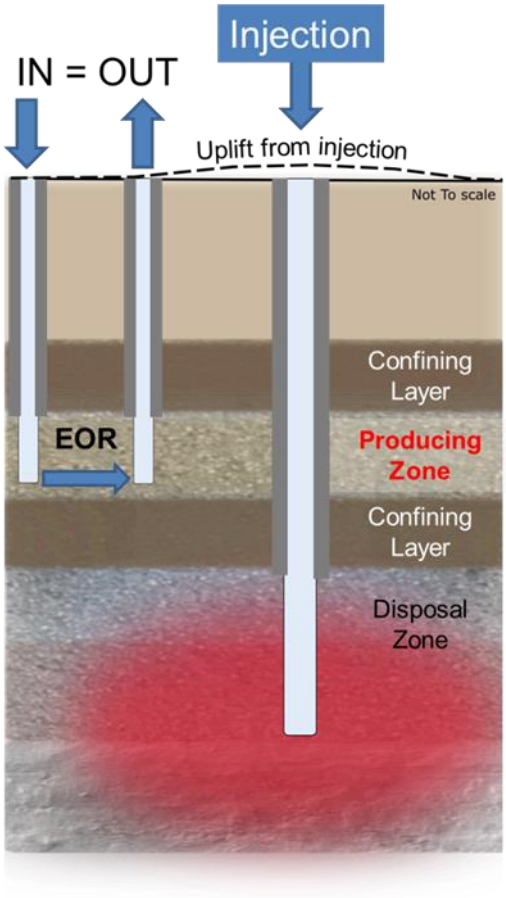

Figure 3.1: Conceptual diagram depicting surface uplift related to pore pressure increase. The enhanced oil recovery (EOR) within the producing zone does not cause surface deformation due to the net zero injection/extraction. The wastewater disposal injection (right well) does cause surface uplift due to the large increase of pore pressure in the disposal zone.

Here, we present a simple relation that relates pore pressure changes to 1D compaction or expansion, and therefore, surface deformation. This work is motivated by the new applications of DInSAR in areas of wastewater injection [e.g. *Shirzaei et al.*, 2016; *Barba-Sevilla et al.*, 2018; *Kim and Lu*, 2018; *Loesch and Sagan*, 2018]. The formulation can be used for constraining hydraulic parameters in pore pressure models and analytical solutions. The simplicity of the relation allows for broad accessibility to modelers of all levels with low computational expense.

3.2 Model Results to Surface Deformation Relation

Vertical deformation by compaction or expansion of the geologic material in the groundwater system can be calculated, as explained by *Hoffman et al.* [2003], based on the *Terzaghi* [1925] principle of coupling between sediment compaction and changes in hydraulic head.

Hydraulic head (h) [m] can be expressed by the sum of elevation head (h_z) [m] and pressure head:

$$h = \frac{p}{\rho_f g} + h_z \tag{1}$$

where p is pore pressure [Pa], ρ_f [kg/m^3] is fluid density, and g [m/s^2] is gravitational acceleration. Elevation head does not change; therefore, the change in hydraulic head can be expressed by the change in pressure head or the pore pressure.

In the most general form, the effective stress tensor (σ'_{ij}) is calculated from:

$$\sigma'_{ij} = \sigma_{ij} - \delta_{ij} p, \tag{2}$$

where σ_{ij} [Pa] is total stress tensor and p [Pa] is pore pressure. The Kronecker delta δ_{ij} is defined as 1 if i=j and 0 if $i \neq j$. Equation 2 becomes the following when only the vertical component (kk) is considered:

$$\sigma'_{zz} = \sigma_{zz} - p \tag{3}$$

Considering that the hydraulic head can be expressed by pressure head and changes in fluid density caused by the compression or expansion of water are considered negligible, the change in vertical effective stress can be expressed as:

$$\Delta\sigma'_{zz} = \rho_f g \Delta h, \tag{4}$$

where Δh [m] is the change in hydraulic head, or drawdown. Compressibility of material is defined as:

$$\alpha_m = \frac{-\frac{\Delta V}{V}}{\Delta \sigma'}, \tag{5}$$

where α_m [Pa^{-1}] is the compressibility of the material, ΔV [m^3] is the change in volume of a control volume with initial volume V [m^3], and $\Delta\sigma'$ [Pa] is the change in effective stress. When considering only the vertical direction, Equation 5 becomes:

$$\overline{\alpha_m} = \frac{-\frac{\Delta b}{b}}{\Delta \sigma'_{zz}}, \tag{6}$$

where Δb [m] is the change in thickness of a control volume with initial thickness b [m]. If it is assumed only changes in pore pressure are responsible for changes in effective stress, Equation 4 and Equation 6 can be combined:

$$\rho_f g \overline{\alpha_m} b = \frac{\Delta b}{\Delta h} \tag{7}$$

This formulation is the basis of the USGS Subsidence and Aquifer-System Compaction (referred to as SUB) package in MODFLOW-2000 [*Hoffman et al.*, 2003]. However, the SUB package assumes the deformation is caused by the removal of water from fine-grained material interbedded within the unconsolidated aquifer and confining layers. In problems like surface deformation from wastewater injection, the surface deformation is assumed to be caused by the expansion of the rocks r due to increases in pore pressure [e.g. *Teatini et al.*, 2011]. We assume that pore pressure increase and deformation are contemporaneous, i.e. no delays due to fluid draining or pressure dissipation in this process. We also assume that the deformation is elastic and recoverable.

The total surface deformation can be calculated using a variation of Equation 7, integrating all layers affected by a pore pressure change. The compressibility of the material is taken into account through the specific storage in the groundwater model. Specific storage is a measure of the ability of the aquifer to store or release water per unit volume per unit change in

hydraulic head. Specific storage (S_s) [m^{-1}] is a function of the compressibility of the aquifer material (α_m) and the compressibility of water (β):

$$S_s = \rho_f g(\alpha_m + n\beta), \tag{8}$$

where n is porosity [-] of the aquifer material and β the compressibility of water [Pa^{-1}] and the product of the two can be considered negligible. Therefore, the change in thickness (Δb) [m] can be expressed by substituting Equation 8 into Equation 7:

$$\Delta b = S_s b \Delta h \tag{9}$$

Using the relation in Equation 9, the total surface deformation can be calculated by summing over the model discretized layers:

$$D(i,j,t) = \sum_{k=1}^{N} S_{s_k} b_k \Delta h_k, \tag{10}$$

where *D* [m], the total surface deformation as a function of location *i,j* (row, column) and time *t*, is the sum of the individual change in thickness of N model layers. Each model layer's change in thickness is calculated using the layer's specific storage, initial thickness, and change in hydraulic head. Figure 3.2 presents a schematic of calculating the surface deformation based on the model discretization. The total surface deformation estimated from the pore pressure model can then be compared to the observed surface deformation results calculated by DInSAR or other methods.

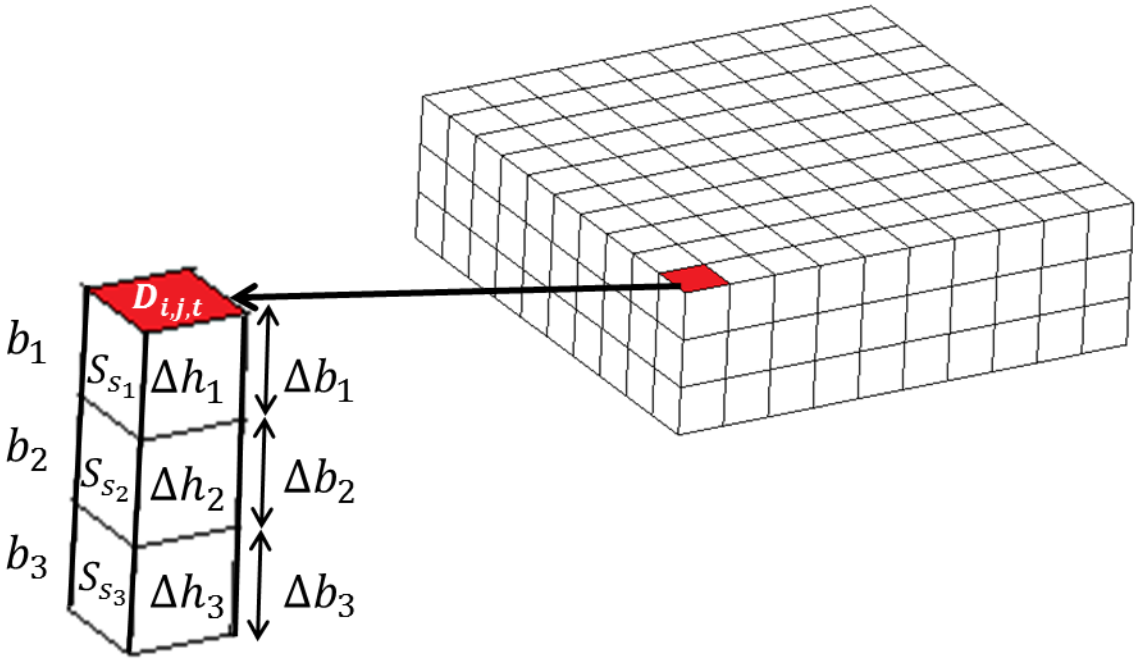

Figure 3.2: Schematic of calculating surface deformation from model results. Surface deformation $D_{i,j,t}$ at the red location can be calculated by adding Δb_k using the thickness b_k, specific storage S_{s_k}, and change in hydraulic head, Δh_k, of N=3 layers in Equation 10.

Figure 3.2 shows a uniform model grid in vertical and lateral directions, but Equation 10 can be applied to models of any discretization. Once the estimates of surface deformation due to modeled hydraulic head (pore pressure) change are completed, a properly georeferenced map can be generated by interpolating the deformation estimates at the center points of each cell. This allows for comparison between the observed surface deformation and the modeled surface deformation.

3.3 Technique Validation

To validate this method, we use the DInSAR results of *Kim and Lu* [2018] in Winker, Texas. *Kim and Lu* [2018] calculated a vertical uplift between late 2014 and April 2017 of approximately 5 – 6 centimeters near two wastewater disposal wells (API No. 42-495-33675 and

42-495-30150). The majority of the uplift (~5.0 cm) occurred after the disposal well API No. 42-495-33675 started injection in January 2016. The maximum surface uplift occurred close to the disposal well API No. 42-495-33675. A time series of the uplift was created by *Kim and Lu* [2018] approximately 270 m from the well. The overall uplift was of an irregular elliptic shape that decreased to less than 1 cm of uplift approximately 2 km from the disposal well. To illustrate the usefulness of the relation, we constrain the specific storage of the aquifer using Equation 10.

3.3.1 Theis Solution Validation

We estimate the change in hydraulic head $\Delta h(r,t)$ caused by wastewater injection as a function of distance from the well, *r* [m], and time since injection began, *t* [days], using the analytical *Theis* [1935] solution:

$$\Delta h(r,t) = \frac{Q}{4\pi T}\int_u^\infty \frac{e^{-x}}{x}dx, \quad (11)$$

where *Q* is the injection rate [m^3/day], *T* [m^2/day] is transmissivity, $u = r^2S/4Tt$ is dimensionless time parameter, *S* [-] is storativity, and *x* is the variable of integration. Transmissivity of an aquifer is a measure of the ability of the aquifer to transmit fluid and is calculated by multiplying the hydraulic conductivity of an aquifer by the saturated thickness. The storativity (specific storage multiplied by the saturated thickness) of an aquifer is a measure of how much water can be stored or released for a unit volume of the aquifer. In confined aquifers, storativity is a function of the aquifer compressibility. The Theis solution assumes a homogeneous, isotropic confined aquifer of infinite lateral extent. Therefore, this estimate does not take into consideration any pore pressure diffusion into the formations above or below the injection interval.

Kim and Lu [2018] indicated that the wastewater is injected into the 70 m thick Bell Canyon Formation sandstones; however, according to the H-10 forms publically available online from the Texas Railroad Commission, that is only true of well API No. 42-495-30150. The second well (API No. 42-495-33675) closest to the deformation injects into 730 m of the Bell Canyon Formation and Bone Springs Formation. The average permeability of the Bell Canyon Formation sandstones is 40 md (3.95×10^{-14} m^2) [*Dutton et al.*, 2003] and the permeability of the Bone Springs Formation is approximately 2 md (1.97×10^{-15} m^2) [*Montgomery*, 1997]. We calculated the average horizontal permeability ($k_{\bar{h}}$) using the arithmetic average:

$$k_{\bar{h}} = \frac{(k_1 b_1 + k_2 b_2)}{b_1 + b_2}, \qquad (12)$$

where k_1 and k_2 are the permeabilities [md] and b_1 and b_2 are the thicknesses [m] of the Bell Canyon Formation and Bone Springs Formation respectively. The average permeability of the injection interval is 5.64 md (5.57×10^{-15} m^2). This permeability converts to a hydraulic conductivity of 6.14×10^{-8} m/s; transmissivity is calculated by multiplying the hydraulic conductivity by the aquifer thickness for a value of 3.87 m^2/day. We estimate a constant injection rate over the 486 days between January 2016 and April 2017, by using the average injection rate, 1265 m^3/day, for the disposal well over that period. The injection volumes are publically available (H-10 forms) online through the Texas Railroad Commission. The change of hydraulic head is calculated for radii between 1m and 2,000 m from the well, with a particular interest at 270 m from the well, the approximate location of the DInSAR time series. We start with an estimated initial storativity of 10^{-4} [-] (Figure 3.3).

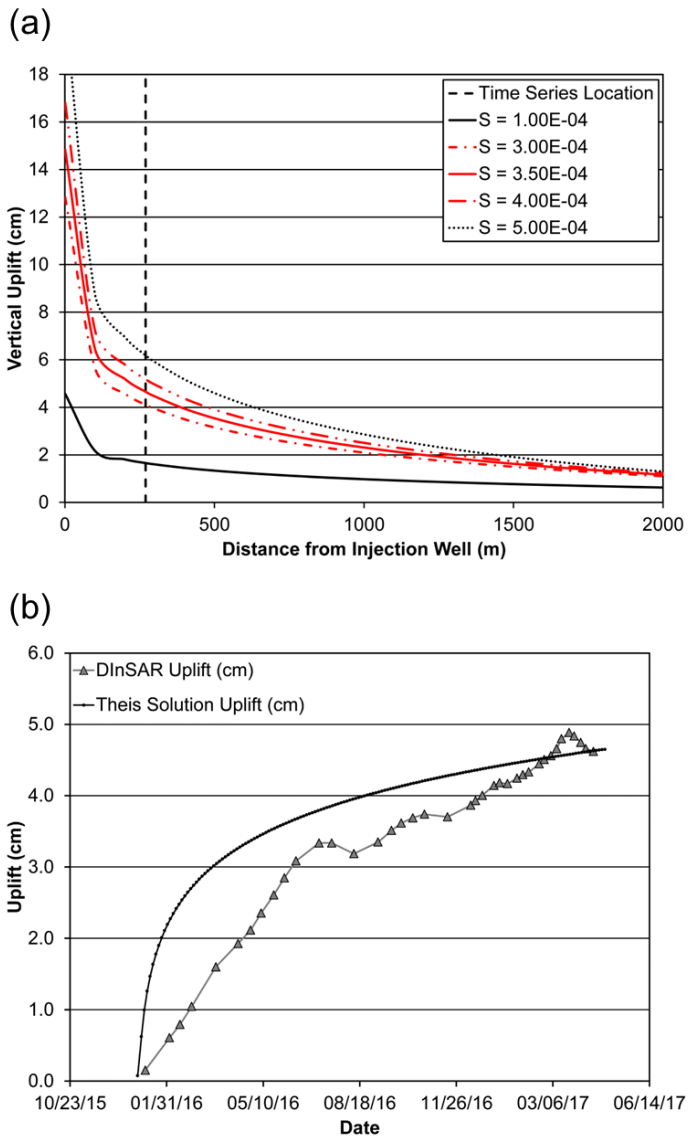

Figure 3.3: Uplift estimates (cm) from the Theis solution. (a) Results after 486 days of constant injection for multiple storativity values. The distance from the well increases along the x-axis. The approximate location of the DInSAR time series [*Kim and Lu*, 2018, Fig. 2a], 270 m from the injection well, is marked by the dashed black line. (b) Time series of uplift estimates at approximately 270 m from the injection well with a storativity of 3.5×10^{-4} [-]. The Theis solution uplift estimates are in the black line/circles, and the DInSAR time series data [*Kim and Lu*, 2018] are indicated by gray triangles.

With the initial storativity estimate, the change in hydraulic head at radii of 270 m and 2000 m from the well is approximately 165 m and 63 m respectively. Using Equation 10, the

estimated surface deformation is 1.65 cm and 0.63 cm (Figure 3.3a). We then constrain the storativity of the aquifer by matching the measured surface deformation (~5 cm since well 42-495-33675 began injection) to the estimated surface deformation using Equation 10. For ~5 cm of uplift at the time series location, the storativity must be approximately $3x10^{-4}$ to $5x10^{-4}$ [-] (Figure 3.3). Figure 3.3b compares the DInSAR time series from *Kim and Lu* [2018] to the uplift estimated based on the Theis solution change in hydraulic head. The two datasets will not match due to the fact that we used a constant injection rate for the Theis solution. However, the general trend in uplift is of the correct order of magnitude and follows the observed DInSAR uplift.

3.3.2 Groundwater Flow Model Validation

To further test the validity of the relation, a pore pressure model of the above problem was created. We created a 3D groundwater flow model using MODFLOW-2005 [*Harbaugh*, 2005] with a domain of 10 km x 10 km x 730 meters. The model simulated the approximately 70 m thick Bell Canyon Formation overlying approximately 660 m of Bone Springs Formation. The Bell Canyon Formation layer was assignment a hydraulic conductivity of $4.35x10^{-7}$ m/s and the Bone Springs Formation a hydraulic conductivity of $2.18x10^{-8}$ m/s. The injection well was placed in the center of the model and injected uniformly over the entire injection interval. The injection rate followed the reported values from January 2016 through April 2017 on the H-10 forms. General-head boundaries were set on each side boundary to virtually extend the size of the model domain. General-head boundaries allow for head dependent flux across the boundary by setting a hydraulic head at some distance beyond the boundary. We set the model to assume no head change 10 km beyond the model domain boundaries. The top and bottom of the model were assigned no-flow boundaries. Note we did not include any heterogeneity, which obviously must be present in the subsurface to create the irregular shape of the uplift.

An initial storativity of $4x10^{-4}$ [-] was used based on the average injection rate and Theis solution estimates, which translated to a total uplift at 270 m from the injection well of approximately 8.5 cm. Specific storage was adjusted to match the approximately 5 – 6 cm surface deformation near the injection well (Figure 3.4). With the variable injection rate, the storativity must be approximately $3x10^{-3}$ [-]. Figure 3.4b compares the time series of estimated uplift from the groundwater model to the DInSAR time series [*Kim and Lu*, 2018]. The overall pattern matches well and is of the same order of magnitude; however, the observed DInSAR uplift has a more gradual uplift than the uplift estimated by the groundwater model results.

Both these validations only vary one parameter, specific storage (storativity), to constrain the model. Varying multiple parameters to optimize the match is best when using surface deformation data. Specific storage of ~10^{-7} to 10^{-6} m^{-1} (storativity ~10^{-4} to 10^{-3}) translates to an aquifer compressibility of ~$1x10^{-11}$ to $1x10^{-10}$ Pa^{-1} using Equation 8. This aquifer compressibility is consistent with competent bedrock [*Freeze and Cherry*, 1979].

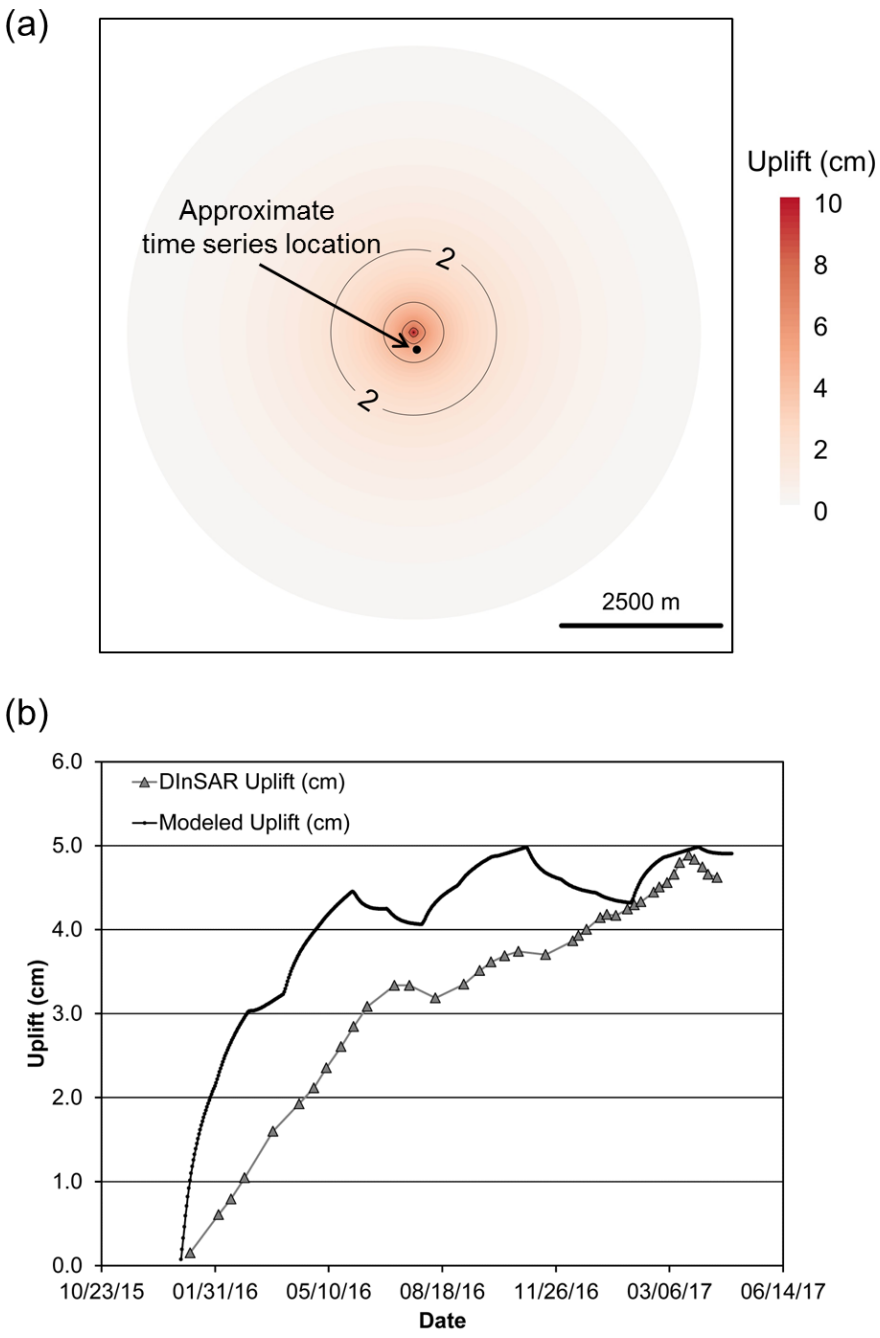

Figure 3.4: Uplift estimates (cm) from groundwater model. (a) Map view of uplift (cm) estimated from modeled change in hydraulic head after 486 days of injection using the reported injection rates with a storativity of $3x10^{-3}$ [-]. The approximate location of the DInSAR time series [*Kim and Lu*, 2018, in Fig. 2a], 270 m from the injection well, is shown at the black dot. (b) Time series of uplift estimates at approximately 270 m from the injection well (black dot in part (a)). The modeled uplift (cm) estimates are in the black line/circles, and the DInSAR time series data [*Kim and Lu*, 2018] are indicated by gray triangles.

3.4 Discussion and Conclusions

Relating 1D compaction to pore pressure changes is not a new concept [*Terzaghi*, 1925]. However, the concept has not been widely applied to use surface deformation as a constraint on models of pore pressure change from injection. Complicated inverse modeling has been conducted to constrain mechanical and hydraulic parameters [e.g. *Rinaldi et al.*, 2017]. While these advanced inverse modeling approaches achieve well constrained models with uncertainty estimates, they are computationally expensive and require a high level of modeling experience and time. The simple physics based relation we present here allows for first-order constraints on model parameters independent of model discretization and with low computational cost.

In areas with little constraint on hydraulic parameters, like areas of wastewater disposal in deep basal aquifers, this relation could be extremely useful. Models of injection of all forms into confined aquifers can be constrained using Equation 10. This approach can also be applied to study sites where artificial recharge is being used or proposed to control subsidence [e.g. *Zhang et al.*, 2015] or store water for later use [e.g. *Farid et al.*, 2018]. In addition, other natural processes where fluid pressure causes a surface deformation could benefit from use of this relation. Equation 10 can be used to constrain changes in permeability that cause surface uplift following earthquakes like the 2011 Tohoku earthquake [*Ishitsuka et al.*, 2017]. Natural injection of hydrothermal fluids around large calderas can also be responsible for surface uplift [*Hurwitz et al.*, 2007] and parameters of the rock could be constrained using this relation.

It should be noted, however, that there are some limitations. Surface deformation is the expression of possibly multiple processes occurring in the subsurface. When using surface deformation to constrain a model the following certain assumptions must be made. If other information about the deformation is not available, one major assumption is that the surface

uplift is caused entirely by pore pressure changes. In addition, this relation assumes that the deformation is one hundred percent elastic, which is not appropriate for all situations. Since the relation is based on 1D-compaction, all deformation is assumed to be vertical. These assumptions can lead to a mismatch of estimated uplift compared to observed uplift. However, that mismatch can also hold information about the system, including evidence for heterogeneity and indication that other processes are also affecting uplift.

Use of DInSAR also has its limitations. DInSAR does not always have high temporal resolution and often has problems with decorrelation due to vegetation, snow cover, shifting sediments, and more [*Massonnet and Feigl*, 1995]. It is important to note that SAR satellites are side-looking that is they do not look perpendicular to the ground, but at some angle off the perpendicular (look angle). Displacement determined by DInSAR is in the line of sight, or direction, the satellite is looking when the SAR images were acquired. Vertical deformation can only be resolved with knowledge about the lateral motion at the site and/or ascending and descending orbit SAR images. If there is lateral motion captured by DInSAR, then the lateral deformation would need to be removed and only the vertical component included when using Equation 10. Other methods of measuring surface deformation can also be used with this relation. GPS has a high temporal resolution but would need to be considered a point measurement for this method. Several or more GPS locations would need to be available to have reasonable constraints on a pore pressure model. Using GPS to ground-truth the surface deformation observed via DInSAR would be ideal for using this relation.

While there are limitations to the use of this relation, Equation 10 offers a simple formula for estimating surface uplift from pore pressure models. This allows a first-order constraint on

the hydraulic parameters of the confined aquifer, especially in cases where parameter data is limited and injection is occurring.

CHAPTER 4: SMALL EARTHQUAKES MATTER IN INJECTION-INDUCED SEISMICITY

Abstract

A simplistic triggering mechanism, pore pressure increase from injection, has been the focus of injection-induced seismicity studies for decades. Research into other possible mechanisms, like poroelastic stress changes, is ongoing, but there has been relatively little focus on earthquake interaction. While studies have looked at how moderate magnitude events ($M \geq 3.0$) may trigger larger magnitude induced seismicity, research into the cumulative effect of the hundreds to thousands of small magnitude ($M \leq 3.0$) events is lacking. Here, we use generic models to compare the possible stress changes from pore pressure increase and from earthquake interactions of small magnitude events. We find that the area of increased pore pressure is much larger than that of positive Coulomb static stress transfer; however, maximum Coulomb static stress change is larger than maximum pore pressure increase. We argue that, yes, small earthquakes do matter, and their interaction may be an important triggering mechanism to consider.

The chapter has been previously published:

Brown, M.R.M. and S. Ge (2018), Small Earthquakes Matter in Injection-Induced Seismicity, *Geophysical Research Letters, 45,* 5445-5453, doi: 10.1029/2018GL077472

4.1 Introduction

The basic physics of injection-induced seismicity has been understood for decades. In a nutshell, injected fluids increase pore pressure and decrease the effective stress on a critically stressed fault [*Hubbert and Rubey*, 1959; *Healy et al.*, 1968], leading to fault failure and earthquakes. However, this is a very simplified view of the triggering mechanism. Coulomb static stress transfer, the process of slip along a fault causing static (permanent) stress change [*King et al.*, 1994], has been used to describe earthquake interactions in a number of natural systems [e.g. *King et al.*, 1994; *Lin and Stein*, 2004; *Toda et al.*, 2005; *Toda et al.*, 2011]. The idea of earthquake interactions is that earthquake slip causes stress to change around the slip and this stress change causes further earthquakes [*King et al.*, 1994]. In natural systems, *King et al.* [1994] found that stress changes as low as 0.01 MPa can trigger seismicity.

Cumulative Coulomb static stress transfer can result from many small to moderate earthquakes. *Ziv and Rubin* [2000] calculated the cumulative static stress change in central California between 1969 and 1998 and found that cumulative static stress changes of much less than 0.01 MPa can still have a triggering effect. This is in line with the notion of a critically stressed crust [*Townend and Zoback*, 2000], which states that faults in the Earth's crust are at frictional equilibrium and only a small perturbation of stress will trigger failure. In the central United States and other areas, induced seismicity from wastewater injection has triggered hundreds to thousands of earthquakes [e.g. *Ellsworth*, 2013; *Weingarten et al.*, 2015; *Nakai et al.*, 2017b]. So, in terms of triggering mechanisms, we ask the question: *What about the earthquakes?*

Studies have shown the Coulomb static stress change (ΔCSS) for a single or a few moderate magnitude induced seismic events [e.g. *Sumy et al.*, 2014; *McNamara et al.*, 2015;

Chen et al., 2017]. *Sumy et al.* [2014] argued that a moderate injection-induced earthquake, magnitude M5.0, led to the triggering of the M5.7 Prague, Oklahoma earthquake through a series of earthquake interactions. *Chen et al.* [2017] calculated the ΔCSS from $M \geq 3.0$ earthquakes and suggest the M5.8 Pawnee, Oklahoma earthquake was also triggered by a combination of injection and earthquake interaction. However, the effects of *cumulative* ΔCSS from *small* magnitude injection-induced seismicity ($M \leq 3.0$) have not been thoroughly investigated.

Helmstetter et al. [2005] estimated the relative importance of small and large earthquakes for static stress transfer and found that while large earthquakes matter more in terms of energy release, small earthquakes are just as important as larger earthquakes for stress changes. A large magnitude event transfers more stress than a smaller one. However, the larger number of small earthquakes adds up. Cumulative static stress change of many small magnitude events is comparable to static stress change of one large magnitude event. Few studies have modeled ΔCSS caused by static stress transfer of actual induced seismicity. In one study, *Catalli et al.* [2013] modeled ΔCSS caused by micro-seismicity induced at the Basel Enhanced Geothermal site without considering stress changes caused by fluid injection. They found 75% of the events occurred in areas of positive ΔCSS that promotes failure. The fact that the majority of earthquakes occur in those areas suggests that earthquake interaction may control subsequent earthquake locations and, therefore, is an important component of induced seismicity.

Coulomb static stress transfer has been discussed as a potential mechanism in wastewater injection induced seismicity as well. *Schoenball et al.* [2018] investigated the Guthrie-Langston, Oklahoma earthquakes and found some areas with continuous seismic activity and others with short bursts of seismic activity. They suggested this could be due to two separate triggering mechanisms: slower pore pressure diffusion and more immediate static stress transfer. Further,

based on analysis of spatiotemporal evolution of induced seismicity in Oklahoma and Southern Kansas, *Schoenball and Ellsworth* [2017] concluded that static stress transfer must play a role as a triggering mechanism. They point out that static stress transfer has a short range of influence and, therefore, could appear similar to fluid diffusion processes.

We hypothesize that pore pressure increase from wastewater injection promotes failure on critically stressed, optimally oriented faults (Figure 4.1) in areas where induced seismicity occurs. Initial earthquakes then promote further failure through Coulomb static stress transfer. This process of earthquake interactions may continue and promote failure beyond the area of pore pressure increase, after injection has reduced rates or ceased entirely, and/or at larger magnitudes than previous events (Figure 4.1b). By convention, positive ΔCSS (designated by warm colors) indicates stress change that brings areas closer to failure while negative ΔCSS (designated by cool colors) stabilizes areas. In addition, there may be a "*mitigation limit*" for mitigation action of the injection parameters (e.g. injection rate, injection well spacing) if earthquake interactions become an equal or dominate triggering mechanism for the induced seismicity (Figure 4.1b). If that scenario occurs, mitigation of the seismicity may be ineffective and earthquakes will continue until the system returns to equilibrium. The objective of this study is to compare the relative importance of pore pressure increase and earthquake interactions as triggering mechanisms for injection-induced seismicity.

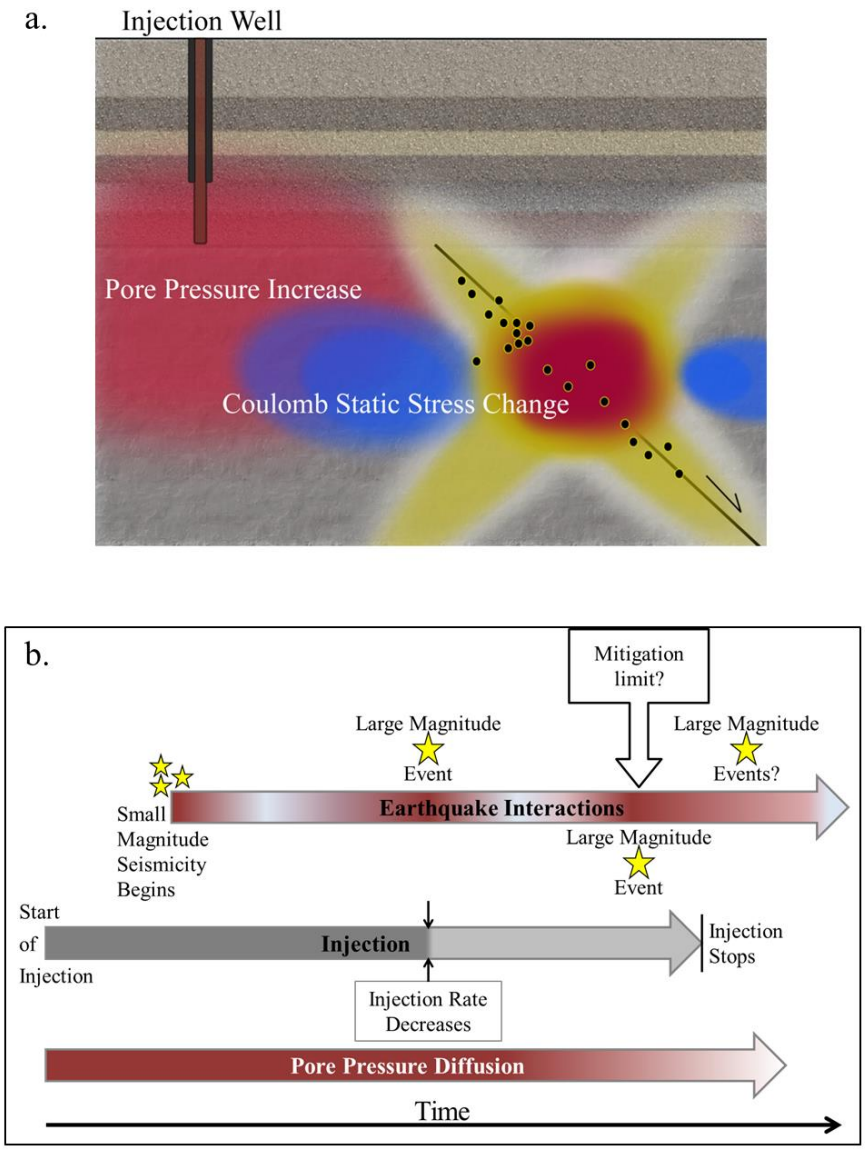

Figure 4.1: Conceptual interpretation of physical triggering mechanisms. (a) Conceptual cross-section diagram (perpendicular to normal fault strike) showing stress changes caused by possible triggering mechanisms. Warm colors (yellows to reds) represent positive stress change that promotes failure and cool colors (blues) represent negative stress change that promotes stability. Black dots represent hypothetical earthquakes in the crystalline basement below the injection interval. (b) Hypothesized scenario of triggering mechanisms, and the relationship to injection and mitigation actions.

4.2 Methods

Here, we use two generic models: one modeling pore pressure change from wastewater injection (Figure 4A.1a) and the other modeling Coulomb static stress transfer from a single cluster of earthquakes on two idealized faults (Figure 4A.1b). The models are independent of one another, and the stress changes are compared as separate but complementary triggering mechanisms. We use independent models to compare the stress change caused by reasonable scenarios of injection and earthquake occurrence to determine if the cumulative effect of small magnitude earthquakes can generate the same level of stress change as pore pressure increase that initiates the induced seismicity.

4.2.1 Pore Pressure Modeling

We model pore pressure change (ΔP) using a model with one injection well in the center of the model domain. The 3D model dimension is 50 km by 50 km by 10 km. A cross-sectional view of the model domain through the injection well is shown in Figure A.1a. The model consists of three lithologic layers: a 1,000 m thick confining layer starting at the surface (0 to -1,000 m); a 500 m thick injection interval (-1,000 to -1,500 m); and 8,500 m of crystalline basement (-1,500 to -10,000 m). We use MODFLOW-2005 to model ΔP caused by injection (full details in Appendix A.1). We conduct numerous simulations using reasonable ranges of values for permeability, specific storage, and injection rate. We vary permeability of the injection interval between 10^{-16} and 10^{-12} m^2. The crystalline basement has the same permeability of the injection interval at the contact and decreases with depth to 10^{-18} m^2 at -10,000 m. We vary specific storage between 10^{-7} and 10^{-5} m^{-1}. We run the models varying injection rates between 2,000 and 4,240 m^3/day (~377,400 and ~800,000 barrels per month). Each simulation models

ΔP due to injection at a constant rate for ten years. A full summary of model parameters for each simulation is included in Table A.1.

4.2.2 Coulomb Static Stress Transfer Modeling

Coulomb static stress transfer modeling was conducted using USGS Coulomb 3 software [*Lin and Stein*, 2004; *Toda et al.*, 2005], which calculates static stress transfer in an elastic half-space with uniform isotropic elastic properties. Coulomb static stress transfer is the process whereby static stress change results from slip along a source fault. Coulomb static stress transfer can promote or reduce the potential for earthquake triggering [e.g. *King et al.*, 1994; *Stein*, 1999; 2005; *Toda et al.*, 2012] based on the change of shear and normal stresses on the fault. After an earthquake, ΔCSS can be calculated on faults in areas around the earthquake slip, particularly receiver faults or optimally oriented faults. Receiver faults are faults with prescribed orientations; optimally oriented faults are faults with orientations most prone to slip in a given background stress. Coulomb static stress change (ΔCSS) is calculated as [*Stein*, 1999]:

$$\Delta CSS = \Delta\tau_s + \mu'(\Delta\sigma_n) \quad (1)$$

where $\Delta\tau_s$ is shear stress change (positive when increased in the direction of fault slip); μ' is effective coefficient of fault friction on the receiver fault; and $\Delta\sigma_n$ is normal stress change (positive when the fault is unclamped). Calculating static stress transfer to a prescribed fault orientation, receiver fault, is independent of background stress, but relies on the coefficient of friction, fault geometry, and sense of slip [*King et al.*, 1994].

We examine two idealized fault scenarios in this study (Figure A.1b): (1) a vertical left-lateral strike slip fault and (2) a normal fault striking 0° north and dipping 60° east. We generate the earthquake catalogs used to calculate Coulomb static stress transfer using the Gutenberg-Richter [*Gutenberg and Richter*, 1944] Magnitude-Frequency relation which is the power-law:

$$\log_{10} N = a - bM, \qquad (2)$$

where N is the number of events greater than or equal to magnitude M, and a and b are constants. The constant b relates the frequency of small events to larger events – the larger the b-value the more small magnitude events there are in relation to large magnitude events. The constant a relates to the productivity or total number of events for the system. We use three b-values low, average, and high (0.8, 1.0, and 1.2 respectively) and keep a consistent at $a = 3$. A range of b-values has been calculated for induced seismicity from low (< 1.0) b-values [*Goebel et al.*, 2017] to high (> 1.0) b-values [e.g. *Bachmann et al.*, 2012; *Brown and Liu*, 2016; *Goebel et al.*, 2017; *Mousavi et al.*, 2017]. We include all earthquakes of magnitude 1.0 and larger. The generated catalogs (data set S1) are: 158 events with magnitudes from M1.0 to M3.7 for $b = 0.8$; 100 events with magnitudes from M1.0 to M3.0 for $b = 1.0$; and 63 events with magnitudes from M1.0 to M2.5 for $b = 1.2$. We assigned random locations to each of the events using statistical distributions normalized to fault size [*Mai et al.*, 2005] and realistic fault sizes (Appendix A.2). We chose a fault length of 10 km and fault width of 4 km which is consistent with fault sizes for induced seismicity in New Mexico [*Nakai et al.*, 2017b]; Oklahoma [*Yeck et al.*, 2016b; *Yeck et al.*, 2017]; and Arkansas [*Horton*, 2012].

In addition to earthquake locations, earthquake parameters were needed for each event. Earthquake parameters include rupture length, rupture width, average slip, and slip direction. Coulomb 3 has built-in empirical fault relationships between earthquake magnitude and earthquake parameters, derived by *Wells and Coppersmith* [1994]. The empirical relationships, however, were derived based on earthquakes M > 4.5. Since the modeled seismicity is of M ≤ 3.7 using *Wells and Coppersmith* [1994] is not appropriate. Therefore, we use alternative relations [*Leonard*, 2010] to determine fault rupture length, fault rupture width, and average displacement

(Table A.2). The relations developed by *Leonard* [2010] apply to faults of all lengths and magnitudes. The earthquake locations are taken as the center point of earthquake rupture. We use parameters calculated from the relations of *Leonard* [2010] and set rupture length and rupture width around the center points. We set the slip direction to be pure left-lateral strike slip faulting or pure down-dip normal faulting. We use an effective coefficient of friction of 0.6 and Young's modulus of 80 GPa. We simulate the slip of each event as a rupture along a single fault. We calculate Coulomb static stress transfer for the cumulative change from all events for each catalog. The stress change is calculated on a receiver fault of the same orientation and slip direction as the source fault with the modeled earthquakes. The intention is to determine stress changes along the fault with sections that are already activated. In addition, we modeled scenarios with variable focal mechanisms (Appendix A.2) for a more realistic faulting scenario along a single fault.

4.3 Results

4.3.1 Pore Pressure Modeling Results

Results from pore pressure modeling show that pore pressure increase varies over several orders of magnitude with changing parameters. The results shown in Figure 4.2a are ΔP directly below the injection well within the crystalline basement. We eliminated two model simulations due to unrealistically high pressures near the injection well, but include them in Figure A.2. Results are most sensitive to the hydraulic permeability of the injection interval and crystalline basement. Maximum ΔP varies from 0.04 to 42.6 MPa. This is consistent with other site specific pore pressure models of induced seismicity [e.g. *Healy et al.*, 1968; *Keranen et al.*, 2014; *Hornbach et al.*, 2015; *Ogwari and Horton*, 2016; *Brown et al.*, 2017; *Nakai et al.*, 2017b]. Low permeability generates the largest pore pressure increase, but pore pressure does not diffuse very

far into the basement or laterally (Figure 4.2b); high permeability generates much further diffusion of pore pressure increase, but the magnitude of the increase is much smaller (Figure 4.2d) than low and medium permeability simulations (Figure 4.2b-c).

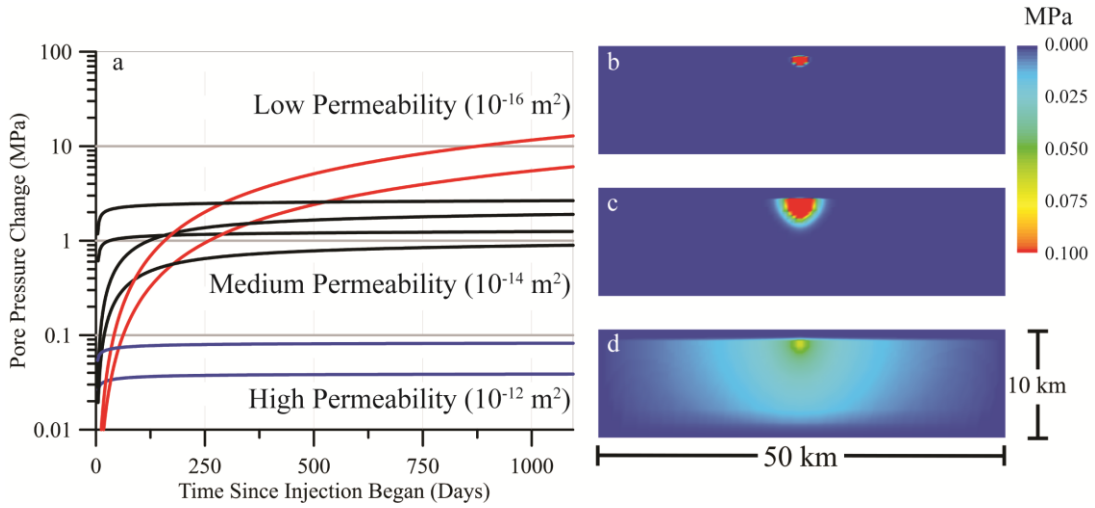

Figure 4.2: Pore pressure modeling results. (a) Graph of ΔP at the yellow dot, shown in Figure A.1a, directly below the injection well in crystalline basement. Simulations are grouped by permeability of injection interval (low, medium, or high). (b-d) Cross-sections of ΔP through the injection well after 3 years (1,095 days) of constant injection. (b) Low permeability, (c) medium permeability, and (d) high permeability.

4.3.2 Coulomb Static Stress Modeling Results

Results of the Coulomb static stress transfer modeling show that the largest change in stress was in the lowest *b*-value scenarios, consistent with a larger number of events with higher magnitude (Figure 4.3). The ΔCSS is shown in Figure 4.3 for average depth of the earthquakes, ranging from 3.8 to 4.3 km (Table A.3), and in the direction of slip of the source fault. There are areas of positive ΔCSS in all scenarios that are as large as or larger than estimated triggering thresholds of pore pressure (~0.07 to 0.10 MPa) from site specific studies [e.g. *Keranen et al.*, 2014; *Brown et al.*, 2017]. Maximum ΔCSS at average depth varies from approximately 12 to

770 MPa in strike-slip fault scenarios (Figure 4.3a-c) and approximately 18 to 62 MPa in normal fault scenarios (Figure 4.3d-f).

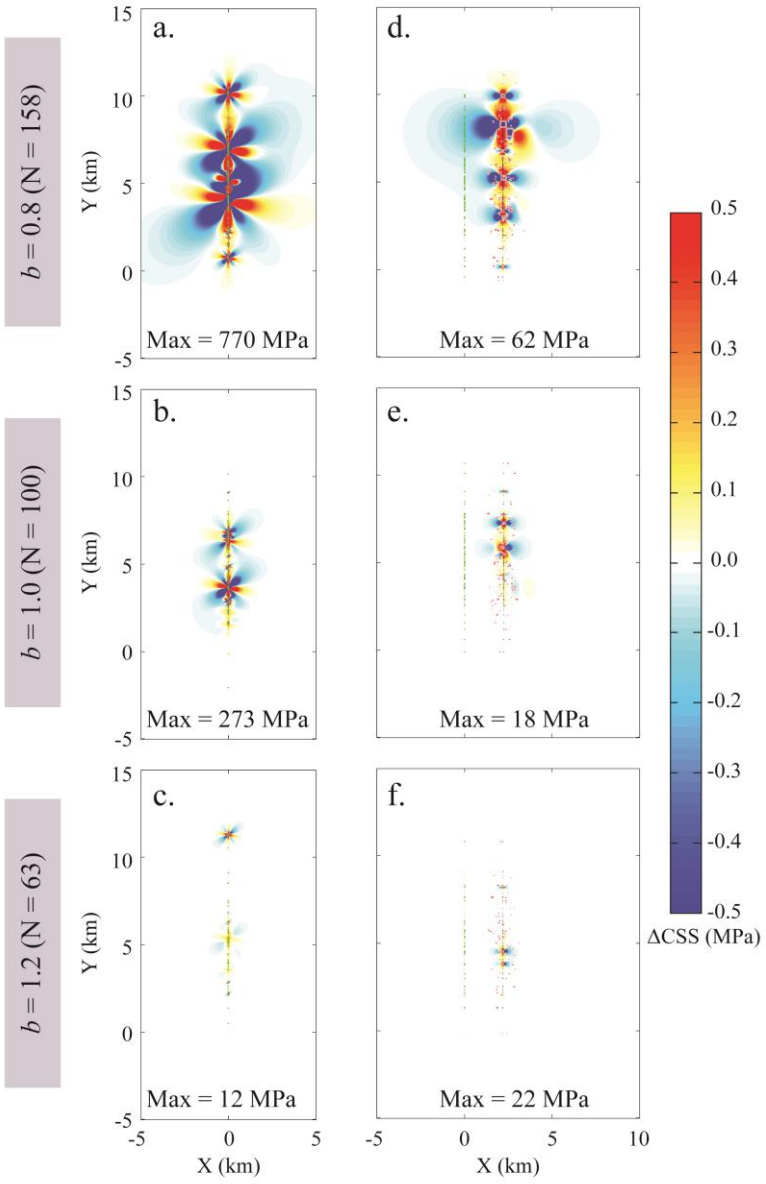

Figure 4.3: Coulomb static stress transfer model results for six event sequences at the average depth of the earthquakes for a receiver fault with the same orientation and direction of slip as the modeled earthquakes. (a – c) left-lateral strike slip fault results and (d – f) normal fault results. First row (a, d) are results for the catalog of 158 events generated using a *b*-value of 0.8; second row (b, e) are results for the catalog of 100 events generated using a *b*-value of 1.0; and third row (c, f) are results for the catalog of 63 events generated using a *b*-value of 1.2. The maximum positive ΔCSS is indicated for each scenario.

We also calculate modeled area at target depths (top of basement in ΔP models and average depth of earthquakes for ΔCSS models) with stress changes ≥ 0.01 MPa and ≥ 0.10 MPa (Figures A.3 and A.4). Sensitivity analysis is conducted to determine the effect varying the effective coefficient of friction has on the model, and it is found that the maximum ΔCSS and modeled area is largely insensitive to the effective coefficient of friction (Table A.5). *Hardebeck* [2006] found that for small fault lengths focal mechanism variability is within one standard deviation uncertainty of focal mechanisms, ~25°. Focal mechanism studies of induced seismicity in Texas [*Quinones et al.*, 2018] found that the mechanisms in single sequences are surprisingly consistent. Further sensitivity studies were conducted using variable focal mechanisms (Appendix A.2). While varied focal mechanism scenarios resulted in a decreased maximum ΔCSS (Table A.4) compared to consistent (pure strike slip or normal faulting) focal mechanism scenarios (Figure 4.4), the values are still as large as or larger than maximum ΔP. In addition, we modeled the ΔCSS for single moderate magnitude events with a seismic moment similar to the cumulative moment of the small magnitude events. Maximums of ΔCSS and most modeled areas above the stress threshold are lower than for the small magnitude scenarios (Table A.6).

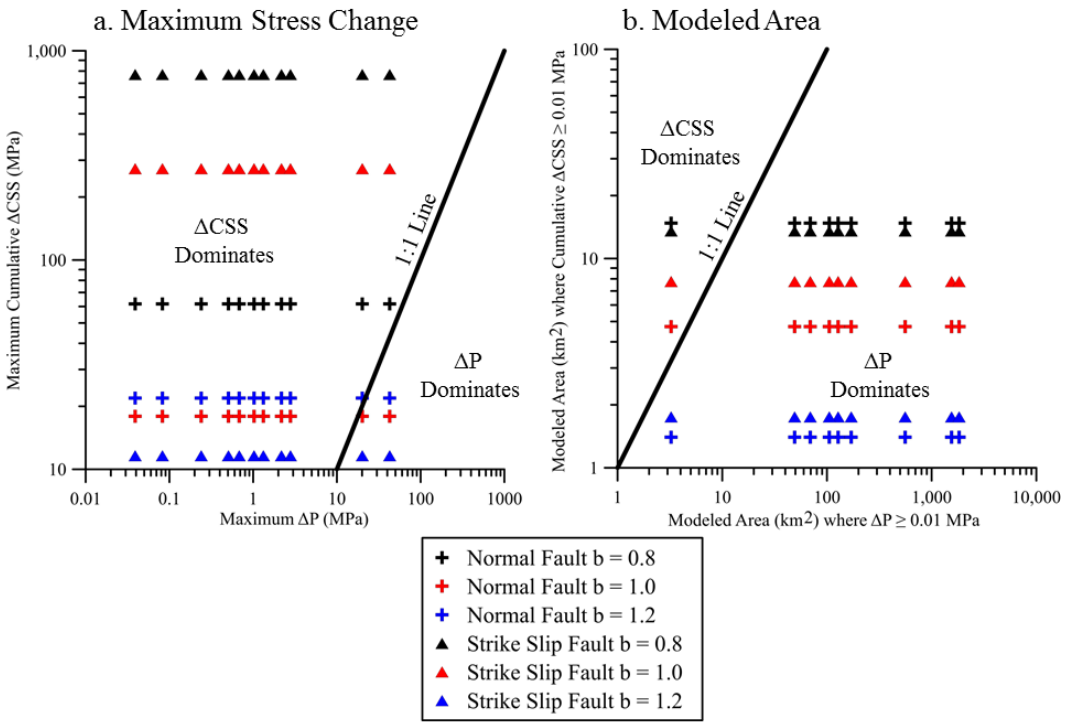

Figure 4.4: Comparison of modeled ΔP to modeled ΔCSS. The black lines indicate the 1:1 line separating the ΔCSS dominate region (above) from the ΔP dominate region (below). (a) Comparison of modeled maximum ΔP to modeled maximum ΔCSS. (b) Comparison of areas with modeled stress changes greater than or equal to 0.01 MPa. Area is calculated at average depth of the earthquakes for ΔCSS and directly below the injection interval at top of crystalline basement for ΔP.

4.4 Discussion

We compare magnitude of maximum ΔP from pore pressure modeling and maximum ΔCSS from Coulomb static stress transfer modeling in Figure 4.4a. A 1:1 line is included to separate ΔP dominated and ΔCSS dominated regions. We find that in the majority of cases, maximum ΔCSS is larger than maximum ΔP. This comparison shows that after a sequence of small magnitude events occurs, positive ΔCSS is at least comparable to the ΔP. Therefore,

earthquake interactions between small magnitude events initially induced by pore pressure increase may induce further seismicity in the same area.

We also compare the areas where modeled stress changes are ≥ 0.01 MPa (Figure 4.4b) for the average depth of the earthquakes (Table A.3) for ΔCSS results and the top of crystalline basement directly below the injection interval for ΔP results. For the majority of the pore pressure model scenarios, the area of ΔP is larger than ΔCSS in the Coulomb static stress transfer models. This confirms the recognized importance of pore pressure increase in inducing seismicity. The larger spatial extent of pore pressure change above the threshold of 0.01 MPa elevates the potential for encountering critically stressed optimally oriented faults. However, the much larger maximum stress change seen in the Coulomb static stress transfer modeling illustrates the importance of ΔCSS triggering. While the area of modeled stress increase above the 0.01 MPa threshold is small, the area is near the activated fault. The earthquake interactions could induce additional earthquakes along the fault that other events have already occurred.

Results of this study indicate the possible significance earthquake interactions can have in guiding mitigation efforts for injection-induced seismicity. Injection-induced seismicity has caused no deaths in the United States, but has caused property damage [*Morgan and Morgan*, 2011; *Yeck et al.*, 2016a], personal injury [*Yeck et al.*, 2017], and increased risk of damaging critical infrastructure [*McNamara et al.*, 2015]. Earthquake interactions may provide urgency for mitigation actions if the stress transfer from earthquake interaction generates sufficient stress changes to encourage continued induced seismicity. If earthquakes are shown to promote further triggering of more earthquakes (Figure 4.1), then effective mitigation options may be limited by how many earthquakes occur prior to mitigation action being taken.

In addition, in some instances the largest induced events have occurred following injection wells reducing or ceasing injection [e.g. *Kim*, 2013; *Yeck et al.*, 2017]. In both Youngstown, Ohio [*Kim*, 2013] and Fairview, Oklahoma [*Yeck et al.*, 2017] cases, the largest magnitude events occurred following sequences of small magnitude events. Continued seismicity could be related to pore pressure diffusion and/or earthquake interactions. Induced seismicity has been observed at great distances [e.g. *Keranen et al.*, 2014; *Block et al.*, 2015], 20 – 30 km or more, from the injection well. It may be possible that earthquake interactions of the small earthquakes near the largest events were a triggering mechanism for new earthquakes likely in addition to triggering by pore pressure increase. Finally, Coulomb static stress transfer has been indicated as a possible triggering mechanism for the two largest earthquakes in Oklahoma, the M5.7 Prague [*Sumy et al.*, 2014] and M5.8 Pawnee [*Chen et al.*, 2017] events. Considering the role of earthquake interaction of small magnitude events could be crucial to proper mitigation action decisions. Further site specific studies are needed to determine the extent of Coulomb static stress transfer as a mechanism for injection-induced seismicity.

4.5 Conclusions

Our generic models show that Coulomb static stress transfer from small earthquakes ($1.0 \leq M \leq 3.7$) can have a cumulative effect that generates stress changes as large as or larger than the modeled ΔP caused by wastewater injection. Maximum ΔCSS ranged approximately 12 – 770 MPa in strike-slip fault scenarios and approximately 18 – 62 MPa in normal fault scenarios. Pore pressure increase in the generic groundwater model reached to as high as 42.6 MPa. Therefore, the stress changes that can promote seismicity are comparable for both triggering mechanisms, pore pressure increase from injection and earthquake interactions. However, the areas of increased pore pressure are much larger than the areas of positive ΔCSS, which means

there is a higher potential for pore pressure increased area to encounter additional critically stressed faults. The positive ΔCSS does remain close to the modeled fault and may promote additional slip along the activated fault. This work indicates the role of the induced earthquake interactions, even though they are small magnitude events, could generate more induced seismicity. The positive ΔCSS near the already activated fault may limit the effectiveness of mitigation by triggering more earthquakes.

REFERENCES

Agarwal, R. G., R. Al-Hussainy, and H. J. J. Ramey (1970), An Investigation of Wellbore Storage and Skin Effect in Unsteady Liquid Flow: 1. Analytical Treatment, *Society of Petroleum Engineers Journal*, *10*, 279-290.

Bachmann, C. E., S. Wiemer, B. P. Goertz-Allmann, and J. Woessner (2012), Influence of pore-pressure on the event-size distribution of induced earthquakes, *Geophysical Research Letters*, *39*(9), L09302, doi:10.1029/2012gl051480.

Barba-Sevilla, M., B. Baird, A. Liel, and K. Tiampo (2018), Hazard Implications of the 2016 Mw 5.0 Cushing, OK Earthquake from a Joint Analysis of Damage and InSAR Data, *Remote Sensing*, *10*(11), doi:10.3390/rs10111715.

Bear, J. (1979), *Hydraulics of Groundwater*, McGraw-Hill, New York, NY.

Belitz, K., and J. D. Bredehoeft (1988), Hydrodynamics of Denver Basin: Explanation of Subnormal Fluid Pressures, *The American Association of Petroleum Geologists Bulletin*, *72*(11), 1334-1359.

Bell, J. W., F. Amelung, A. R. Ramelli, and G. Blewitt (2002), Land Subsidence in Las Vegas, Nevada, 1935-2000: New Geodetic Data Show Evolution, Revised Spatial Patterns, and Reduced Rates, *Environmental & Engineering Geoscience*, *8*(3), 155-174, doi:10.2113/8.3.155.

Block, L. V., C. K. Wood, W. L. Yeck, and V. M. King (2015), Induced seismicity constraints on subsurface geological structure, Paradox Valley, Colorado, *Geophysical Journal International*, *200*(2), 1172-1195, doi:10.1093/gji/ggu459.

Bommer, J. J., H. Crowley, and R. Pinho (2015), A risk-mitigation approach to the management of induced seismicity, *J Seismol*, *19*(2), 623-646, doi:10.1007/s10950-015-9478-z.

Brown, M. R. M., S. Ge, A. F. Sheehan, and J. S. Nakai (2017), Evaluating the effectiveness of induced seismicity mitigation: Numerical modeling of wastewater injection near Greeley, Colorado, *Journal of Geophysical Research: Solid Earth*, *122*(8), 6569-6582, doi:10.1002/2017jb014456.

Brown, M. R. M., and M. Liu (2016), Injection-induced seismicity in Carbon and Emery Counties, central Utah, *Geofluids*, *16*(5), 801-812, doi:10.1111/gfl.12184.

Catalli, F., M.-A. Meier, and S. Wiemer (2013), The role of Coulomb stress changes for injection-induced seismicity: The Basel enhanced geothermal system, *Geophysical Research Letters*, *40*(1), 72-77, doi:10.1029/2012gl054147.

Catalli, F., A. P. Rinaldi, V. Gischig, M. Nespoli, and S. Wiemer (2016), The importance of earthquake interactions for injection-induced seismicity: Retrospective modeling of the Basel Enhanced Geothermal System, *Geophysical Research Letters*, *43*(10), 4992-4999, doi:10.1002/2016gl068932.

Chen, X., N. Nakata, C. Pennington, J. Haffener, J. C. Chang, X. He, Z. Zhan, S. Ni, and J. I. Walter (2017), The Pawnee earthquake as a result of the interplay among injection, faults and foreshocks, *Sci Rep*, *7*(1), 4945, doi:10.1038/s41598-017-04992-z.

COGCC (2016), Colorado Oil & Gas Conservation Commission, edited.

Colorado Division of Water Resources (1976), Ground Water Resources of the Bedrock Aquifers of the Denver Basin, Colorado*Rep.*, Department of Natural Resources, Denver, CO.

Dart, R. (1985), Horizontal-stress directions in the Denver and Illinois Basins from the orientation of borehole breakouts*Rep.*, 85-733 pp, U.S. Geological Survey, Denver, CO.

Diao, Y., and R. M. Espinosa-Marzal (2018), The role of water in fault lubrication, *Nat Comm*, *9*(1), 2309, doi:10.1038/s41467-018-04782-9.

Duffield, G. M. (2006), AQTESOLV for Windows Version 4 User's Guide*Rep.*, HydroSOLVE, Inc., Reston, VA.

Dutton, S. P., W. A. Flanders, and M. D. Barton (2003), Reservoir characterization of a Permian deep-water sandstone, East Ford field, Delaware basin, Texas, *AAPG Bulletin*, *87*(4), 609-627.

DYFI (2016), USGS Did You Feel It? reports, edited.

Ellsworth, W. L. (2013), Injection-induced earthquakes, *Science*, *341*(6142), 1225942, doi:10.1126/science.1225942.

Farid, H. U., A. Bakhsh, M. U. Ali, Z. Mahmood-Khan, A. Shakoor, and I. Ali (2018), Field investigation of aquifer storage and recovery (ASR) technique to recharge groundwater: a case study in Punjab province of Pakistan, *Water Science and Technology: Water Supply*, *18*(1), 71-83, doi:10.2166/ws.2017.083.

Freeze, R. A., and J. A. Cherry (1979), *Groundwater*, Prentice-Hall, Inc., Englewood Cliffs, NJ.

Goebel, T. H. W., M. Weingarten, X. Chen, J. Haffener, and E. E. Brodsky (2017), The 2016 Mw5.1 Fairview, Oklahoma earthquakes: Evidence for long-range poroelastic triggering at >40 km from fluid disposal wells, *Earth and Planetary Science Letters*, *472*, 50-61, doi:10.1016/j.epsl.2017.05.011.

Gutenberg, B., and C. F. Richter (1944), Frequency of earthquakes in California, *Bulletin of the Seismological Society of America*, *36*, 185-188.

Harbaugh, A. W. (2005), MODFLOW-2005, the U.S. Geological Survey modular ground-water model -- the Ground-Water Flow Process, in *U.S. Geological Survey Techniques and Methods 6-A16*, edited.

Hardebeck, J. L. (2006), Homogeneity of Small-Scale Earthquake Faulting, Stress, and Fault Strength, *Bulletin of the Seismological Society of America*, *96*(5), 1675-1688, doi:10.1785/0120050257.

Healy, J. H., W. W. Rubey, D. T. Griggs, and C. B. Raleigh (1968), The Denver Earthquakes, *Science*, *161*(3848), 1301-1310.

Helmstetter, A., Y. Y. Kagan, and D. D. Jackson (2005), Importance of small earthquakes for stress transfers and earthquake triggering, *Journal of Geophysical Research*, *110*, B05S08, doi:10.1029/2004jb003286.

Herrmann, R. (2016), North America moment tensor 1995–2016, edited, St. Louis University web site.

Higley, D. K., and D. O. Cox (2007), Oil and Gas Exploration and Development along the Front Range in the Denver Basin of Colorado, Nebraska, and Wyoming*Rep.*, 1-40 pp.

Hill, D. P. (2008), Dynamic Stresses, Coulomb Failure, and Remote Triggering, *Bulletin of the Seismological Society of America*, *98*(1), 66-92, doi:10.1785/0120070049.

Hoffman, J., S. A. Leake, D. L. Galloway, and A. M. Wilson (2003), MODFLOW-2000 Ground-Water Model – User Guide to the Subsidence and Aquifer-System Compaction (SUB) Package*Rep.*, U.S. Geological Survey, Tucson, Arizona.

Hornbach, M. J., et al. (2015), Causal factors for seismicity near Azle, Texas, *Nat Commun*, *6*, 6728, doi:10.1038/ncomms7728.

Hornbach, M. J., M. Jones, M. Scales, H. R. DeShon, M. B. Magnani, C. Frohlich, B. Stump, C. Hayward, and M. Layton (2016), Ellenburger wastewater injection and seismicity in North Texas, *Physics of the Earth and Planetary Interiors*, *261*, 54-68, doi:10.1016/j.pepi.2016.06.012.

Horton, S. (2012), Disposal of Hydrofracking Waste Fluid by Injection into Subsurface Aquifers Triggers Earthquake Swarm in Central Arkansas with Potential for Damaging Earthquake, *Seismological Research Letters*, *83*(2), 250-260, doi:10.1785/gssrl.83.2.250.

Hsieh, P. A., and J. D. Bredehoeft (1981), A reservoir analysis of the Denver earthquakes: A case of induced seismicity, *Journal of Geophysical Research: Solid Earth*, *86*(B2), 903-920, doi:10.1029/JB086iB02p00903.

Hu, X., Z. Lu, and T. Wang (2018), Characterization of Hydrogeological Properties in Salt Lake Valley, Utah, using InSAR, *Journal of Geophysical Research: Earth Surface*, *123*(6), 1257-1271, doi:10.1029/2017jf004497.

Hubbert, M. K., and W. W. Rubey (1959), Role of fluid pressure in mechanics of overthrust faulting, *Geological Society of America Bulletin*, *70*, 115-206.

Hurwitz, S., L. B. Christiansen, and P. A. Hsieh (2007), Hydrothermal fluid flow and deformation in large calderas: Inferences from numerical simulations, *Journal of Geophysical Research*, *112*(B2), B02206, doi:10.1029/2006jb004689.

Ishitsuka, K., T. Matsuoka, T. Nishimura, T. Tsuji, and T. ElGharbawi (2017), Ground uplift related to permeability enhancement following the 2011 Tohoku earthquake in the Kanto Plain, Japan, *Earth, Planets and Space*, *69*(1), doi:10.1186/s40623-017-0666-7.

Jacob, C. E. (1947), Drawdown test to determine effective radius of artesian well, *Transactions of the American Society of Civil Engineers*, *112*, 1047-1064.

Jahr, T., G. Jentzsch, A. Gebauer, and T. Lau (2008), Deformation, seismicity, and fluids: Results of the 2004/2005 water injection experiment at the KTB/Germany, *Journal of Geophysical Research*, *113*(B11), doi:10.1029/2008jb005610.

Keranen, K. M., H. M. Savage, G. A. Abers, and E. S. Cochran (2013), Potentially induced earthquakes in Oklahoma, USA: Links between wastewater injection and the 2011 Mw 5.7 earthquake sequence, *Geology*, *41*(6), 699-702, doi:10.1130/g34045.1.

Keranen, K. M., M. Weingarten, G. A. Abers, B. A. Bekins, and S. Ge (2014), Sharp increase in central Oklahoma seismicity since 2008 induced by massive wastewater injection, *Science*, *345*(6195), 448-451, doi:10.1126/science.1255802.

Kim, J. W., and Z. Lu (2018), Association between localized geohazards in West Texas and human activities, recognized by Sentinel-1A/B satellite radar imagery, *Sci Rep*, *8*(1), 4727, doi:10.1038/s41598-018-23143-6.

Kim, W.-Y. (2013), Induced seismicity associated with fluid injection into a deep well in Youngstown, Ohio, *Journal of Geophysical Research: Solid Earth*, *118*(7), 3506-3518, doi:10.1002/jgrb.50247.

King, G. C. P., R. S. Stein, and J. Lin (1994), Static Stress Changes and the Triggering of Earthquakes, *Bulletin of the Seismological Society of America*, *84*(3), 935-953.

Langenbruch, C., and M. D. Zoback (2016), How will induced seismicity in Oklahoma respond to decreased saltwater injection rates?, *Science Advances*, *2*.

Leonard, M. (2010), Earthquake Fault Scaling: Self-Consistent Relating of Rupture Length, Width, Average Displacement, and Moment Release, *Bulletin of the Seismological Society of America*, *100*(5A), 1971-1988, doi:10.1785/0120090189.

Lin, J., and R. S. Stein (2004), Stress triggering in thrust and subduction earthquakes and stress interaction between the southern San Andreas and nearby thrust and strike-slip faults, *Journal of Geophysical Research: Solid Earth*, *109*(B2), doi:10.1029/2003jb002607.

Loesch, E., and V. Sagan (2018), SBAS Analysis of Induced Ground Surface Deformation from Wastewater Injection in East Central Oklahoma, USA, *Remote Sensing*, *10*(2), doi:10.3390/rs10020283.

Mai, P. M., P. Spudich, and J. Boatwright (2005), Hypocenter Locations in Finite-Source Rupture Models, *Bulletin of the Seismological Society of America*, *95*(3), 965-980, doi:10.1785/0120040111.

Manning, C. E., and S. E. Ingebritsen (1999), Permeability of the continental crust: Implications of geothermal data and metamorphic systems, *Reviews of Geophysics*, *37*(1), 127-150, doi:10.1029/1998rg900002.

Massonnet, D., and K. L. Feigl (1995), Discrimination of geophysical phenomena in satellite radar interferograms, *Geophysical Research Letters*, *22*(12), 1537-1540, doi:10.1029/95GL00711.

McDonald, M. G., and A. W. Harbaugh (1988), A modular three-dimensional finite-difference ground-water flow model, in *US Geological Survey Techniques of Water-Resources Investigations*, edited, p. 586.

McGarr, A., et al. (2015), Coping with earthquakes induced by fluid injection, *Science*, *347*(6224), 830-831.

McNamara, D. E., et al. (2015), Reactivated faulting near Cushing, Oklahoma: Increased potential for a triggered earthquake in an area of United States strategic infrastructure, *Geophysical Research Letters*, *42*(20), 8328-8332, doi:10.1002/2015gl064669.

Montgomery, S. L. (1997), Permian Bone Spring Formation: Sandstone Play in the Delaware Basin, Part II—Basin, *AAPG Bulletin*, *81*(9), 1423–1434.

Morgan, M. L., and K. S. Morgan (2011), Preliminary Damage Report of the August 22, 2011 Mw 5.3 Earthquake near Trinidad, Colorado*Rep.*

Mousavi, S. M., P. O. Ogwari, S. P. Horton, and C. A. Langston (2017), Spatio-temporal evolution of frequency-magnitude distribution and seismogenic index during initiation of induced seismicity at Guy-Greenbrier, Arkansas, *Physics of the Earth and Planetary Interiors*, *267*, 53-66, doi:10.1016/j.pepi.2017.04.005.

Nakai, J. S., A. F. Sheehan, and S. L. Bilek (2017a), Seismicity of the rocky mountains and Rio Grande Rift from the EarthScope Transportable Array and CREST temporary seismic networks, 2008-2010, *Journal of Geophysical Research: Solid Earth*, doi:10.1002/2016jb013389.

Nakai, J. S., M. Weingarten, A. F. Sheehan, S. L. Bilek, and S. Ge (2017b), A Possible Causative Mechanism of Raton Basin, New Mexico and Colorado Earthquakes Using Recent Seismicity Patterns and Pore Pressure Modeling, *Journal of Geophysical Research: Solid Earth*, *122*(10), 8051-8065, doi:10.1002/2017jb014415.

National Research Council (2013), *Induced Seismicity Potential in Energy Technologies*, 262 pp., The National Academies Press, Washington, DC, doi:10.17226/13355.

Ogwari, P. O., H. R. DeShon, and M. J. Hornbach (2018), The Dallas-Fort Worth Airport Earthquake Sequence: Seismicity Beyond Injection Period, *Journal of Geophysical Research: Solid Earth*, *123*(1), doi:10.1002/2017jb015003.

Ogwari, P. O., and S. P. Horton (2016), Numerical model of pore-pressure diffusion associated with the initiation of the 2010-2011 Guy-Greenbrier, Arkansas earthquakes, *Geofluids*, *16*(5), 954-970, doi:10.1111/gfl.12198.

Qin, Y., X. Chen, B. M. Carpenter, and F. Kolawole (2018), Coulomb Stress Transfer Influences Fault Reactivation in Areas of Wastewater Injection, *Geophysical Research Letters*, *45*(20), 11,059-011,067, doi:10.1029/2018gl079713.

Quinones, L. A., H. R. DeShon, M. B. Magnani, and C. Frohlich (2018), Stress Orientations in the Fort Worth Basin, Texas, Determined from Earthquake Focal Mechanisms, *Bulletin of the Seismological Society of America*, doi:10.1785/0120170337.

Raleigh, C. B., J. H. Healy, and J. D. Bredehoeft (1976), An Experiment in Earthquake Control at Rangely, Colorado, *Science*, *191*(4233), 1230-1237.

Renard, P., D. Glenz, and M. Mejias (2009), Understanding diagnostic plots for well-test interpretation, *Hydrogeology Journal*, *17*(3), 589-600.

Rinaldi, A. P., J. Rutqvist, S. Finsterle, and H.-H. Liu (2017), Inverse modeling of ground surface uplift and pressure with iTOUGH-PEST and TOUGH-FLAC: The case of CO2 injection at In Salah, Algeria, *Computers & Geosciences*, *108*, 98-109, doi:10.1016/j.cageo.2016.10.009.

Rubinstein, J. L., W. L. Ellsworth, and S. L. Dougherty (2018), The 2013–2016 Induced Earthquakes in Harper and Sumner Counties, Southern Kansas, *Bulletin of the Seismological Society of America*, *108*(2), 674-689, doi:10.1785/0120170209.

Rubinstein, J. L., and A. B. Mahani (2015), Myths and Facts on Wastewater Injection, Hydraulic Fracturing, Enhanced Oil Recovery, and Induced Seismicity, *Seismological Research Letters*, *86*(4), 1060-1067, doi:10.1785/0220150067.

Schoenball, M., and W. L. Ellsworth (2017), A Systematic Assessment of the Spatiotemporal Evolution of Fault Activation Through Induced Seismicity in Oklahoma and Southern Kansas, *Journal of Geophysical Research: Solid Earth*, doi:10.1002/2017jb014850.

Schoenball, M., F. R. Walsh, M. Weingarten, and W. L. Ellsworth (2018), How faults wake up: The Guthrie-Langston, Oklahoma earthquakes, *The Leading Edge*, *37*(2), 100-106, doi:10.1190/tle37020100.1.

Schulze-Makuch, D., D. A. Carlson, D. S. Cherkaur, and P. Malik (1999), Scale dependency of hydraulic conductivity in heterogeneous media, *Groundwater*, *37*(6), 904-919, doi:10.1111/j.1745-6584.1999.tb01190.x.

Shirzaei, M., W. L. Ellsworth, K. F. Tiampo, P. J. González, and M. Manga (2016), Surface uplift and time-dependent seismic hazard due to fluid injection in eastern Texas, *Science*, *353*(6306), 1416-1419, doi:10.1126/science.aag0262.

Singh, P. K., R. G. Agarwal, and L. D. Krase (1987), Systematic Design and Analysis of Step-Rate Tests To Determine Formation Parting Pressure, in *62nd Annual Technical Conference and*

Exhibition of the Society of Petroleum Engineers, edited, pp. 491-503, Society of Petroleum Engineers, Dallas, TX.

Stein, R. S. (1999), The role of stress transfer in earthquake occurrence, *Nature*, *402*, 605-609.

Stein, R. S. (2005), Earthquake Conversations, in *Scientific American*, edited, pp. 82-89.

Stewart, F. L., and A. Ingelson (2016), Regulating energy innovation: US responses to hydraulic fracturing, wastewater injection and induced seismicity, *Journal of Energy & Natural Resources Law*, *35*(2), 109-146, doi:10.1080/02646811.2017.1253915.

Sumy, D. F., E. S. Cochran, K. M. Keranen, M. Wei, and G. A. Abers (2014), Observations of static Coulomb stress triggering of the November 2011M5.7 Oklahoma earthquake sequence, *Journal of Geophysical Research: Solid Earth*, *119*(3), 1904-1923, doi:10.1002/2013jb010612.

Teatini, P., G. Gambolati, M. Ferronato, A. Settari, and D. Walters (2011), Land uplift due to subsurface fluid injection, *Journal of Geodynamics*, *51*(1), 1-16, doi:10.1016/j.jog.2010.06.001.

Terzaghi, K. (1925), *Erdbaumechanik auf bodenphysikalisher Grundlage*, 399 pp., Deuticke, Wien, Austria.

Theis, C. V. (1935), The relation between the lowering of the piezometric surface and the rate and duration of discharge of a well using ground water storage, *Transactions American Geophysical Union*, *2*, 519-524.

Toda, S., J. Lin, and R. S. Stein (2011), Using the 2011 M w 9.0 off the Pacific coast of Tohoku Earthquake to test the Coulomb stress triggering hypothesis and to calculate faults brought closer to failure, *Earth, Planets and Space*, *63*(7), 725-730, doi:10.5047/eps.2011.05.010.

Toda, S., R. S. Stein, G. C. Beroza, and D. Marsan (2012), Aftershocks halted by static stress shadows, *Nature Geoscience*, *5*(6), 410-413, doi:10.1038/ngeo1465.

Toda, S., R. S. Stein, K. B. Richards-Dinger, and S. B. Bozkurt (2005), Forecasting the evolution of seismicity in southern California: Animations built on earthquake stress transfer, *Journal of Geophysical Research*, *110*, B05S16, doi:10.1029/2004jb003415.

Townend, J., and M. D. Zoback (2000), How faulting keeps the crust strong, *Geology*, *28*(5), 399-402.

USGS CRC (2016), USGS Core Research Center, edited.

Weingarten, M., and S. Ge (2015), Hydrogeologic modeling aimed at optimizing injection well operation in a hypothetical multi-injection well
reservoir: Implications for induced seismicity, in *2015 AGU Fall Meeting*, edited, San Francisco, CA.

Weingarten, M., S. Ge, J. W. Godt, B. A. Bekins, and J. L. Rubinstein (2015), High-rate injection is associated with the increase in U.S. mid-continent seismicity, *Science*, *348*(6241), 1336 - 1340.

Wells, D. L., and K. J. Coppersmith (1994), New Empirical Relationships among Magnitude, Rupture Length, Rupture Width, Rupture Area, and Surface Displacement, *Bulletin of the Seismological Society of America*, *84*(4), 974-1002.

Wiemer, S., and M. Wyss (2000), Minimum Magnitude of Completeness in Earthquake Catalogs: Examples from Alaska, the Western United States, and Japan, *Bulletin of the Seismological Society of America*, *90*(4), 859–869.

Woessner, J., and S. Wiemer (2005), Assessing the Quality of Earthquake Catalogues: Estimating the Magnitude of Completeness and Its Uncertainty, *Bulletin of the Seismological Society of America*, *95*(2), 684-698, doi:10.1785/0120040007.

Yang, Y. J., and T. M. Gates (1997), Wellbore skin effect in slug-test data analysis for low-permeability geologic materials, *Ground Water*, *35*(6), 931.

Yeck, W. L., G. P. Hayes, D. E. McNamara, J. L. Rubinstein, W. D. Barnhart, P. S. Earle, and H. M. Benz (2017), Oklahoma experiences largest earthquake during ongoing regional wastewater injection hazard mitigation efforts, *Geophysical Research Letters*, *44*(2), 711-717, doi:10.1002/2016gl071685.

Yeck, W. L., A. F. Sheehan, H. M. Benz, M. Weingarten, and J. Nakai (2016a), Rapid Response, Monitoring, and Mitigation of Induced Seismicity near Greeley, Colorado, *Seismological Research Letters*, *87*(4), 837-847, doi:10.1785/0220150275.

Yeck, W. L., M. Weingarten, H. M. Benz, D. E. McNamara, E. A. Bergman, R. B. Herrmann, J. L. Rubinstein, and P. S. Earle (2016b), Far-field pressurization likely caused one of the largest injection induced earthquakes by reactivating a large preexisting basement fault structure, *Geophysical Research Letters*, *43*(19), 10,198-110,207, doi:10.1002/2016gl070861.

Zhang, Y., J. Wu, Y. Xue, Z. Wang, Y. Yao, X. Yan, and H. Wang (2015), Land subsidence and uplift due to long-term groundwater extraction and artificial recharge in Shanghai, China, *Hydrogeology Journal*, *23*(8), 1851-1866, doi:10.1007/s10040-015-1302-x.

Ziv, A., and A. M. Rubin (2000), Static stress transfer and earthquake triggering: No lower threshold in sight?, *Journal of Geophysical Research: Solid Earth*, *105*(B6), 13631-13642, doi:10.1029/2000jb900081.

APPENDIX

A1. Pore Pressure Model

A1.1 Model Set-up

We conducted the pore pressure modeling using MODFLOW-2005 that solves the groundwater flow equation for hydraulic head [*McDonald and Harbaugh*, 1988]:

$$S_s \frac{\partial h}{\partial t} = \frac{\partial}{\partial x}\left(K_x \frac{\partial h}{\partial x}\right) + \frac{\partial}{\partial y}\left(K_y \frac{\partial h}{\partial y}\right) + \frac{\partial}{\partial z}\left(K_z \frac{\partial h}{\partial z}\right) + Q \qquad (1)$$

where S_s is specific storage; h is hydraulic head; t is time; K_x, K_y, and K_z are hydraulic conductivity in the subscript direction; and Q is volumetric flux per unit volume of sources and/or sinks. Hydraulic conductivity is related to permeability based on the fluid properties using the equation:

$$K = \frac{k\rho g}{\mu}, \qquad (2)$$

where K is hydraulic conductivity, k is permeability of the porous media, ρ is fluid density, g is gravitational acceleration, and μ is fluid dynamic viscosity. The hydraulic head change is calculated by subtracting the initial head from the modeled hydraulic head at each time step. Hydraulic head change (Δh) is then related to pore pressure change (ΔP) using the equation:

$$\Delta P = \gamma \Delta h, \qquad (3)$$

where γ is the specific weight of the fluid. We assign an initial head of 0 meters to the model. We assign constant head boundaries with a constant head of 0 meters to the four vertical sides of the model and the model top. We create the model sufficiently large to eliminate boundary effects from the assigned boundary conditions. The model set-up is included in Figure A.1a.

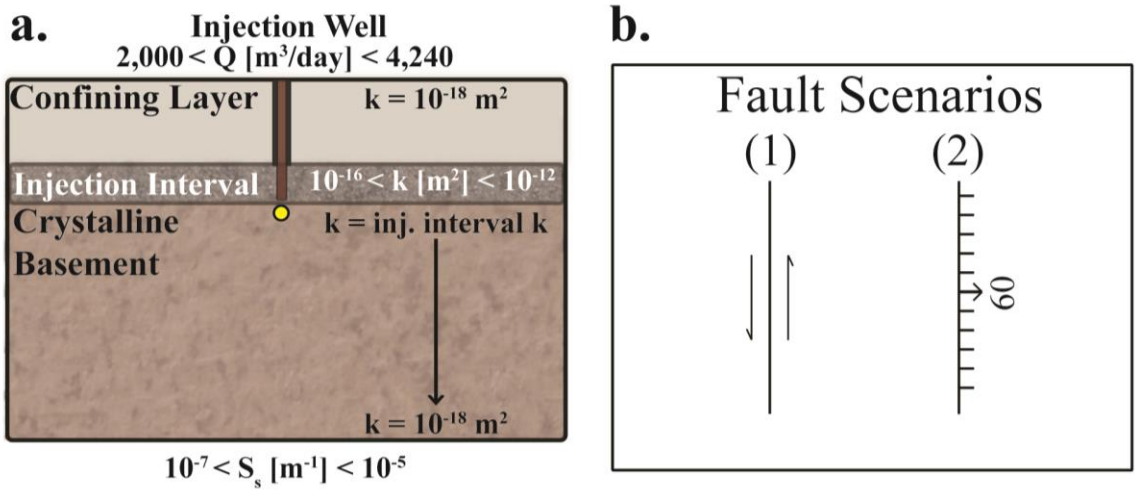

Figure A.1: Generic Model Set-ups. (a) Pore pressure model shown in cross-section. The injection well is located in the center of the model injecting into a 500 m thick injection interval. Permeability (k) ranges are indicated for each lithological layer; the permeability of the crystalline basement decreases with depth. Ranges of injection rate (Q) and specific storage (S_s) are indicated at the top and bottom respectively. The yellow dot is the location of the model results shown in Figure 4.3. (b) Fault scenarios for the Coulomb static stress transfer modeling shown in map view. Fault scenario (1) is a left-lateral vertical strike slip fault and fault scenario (2) is a normal fault striking 0° N and dipping 60° E.

A1.2 Model Results

Figure A.2, shows the model results with all simulations included, including S3 and S10, simulations which we excluded from the main text due to unreasonably high pressure change in the injection well caused by the very low permeability and specific storage combination for those simulations. The full parameters are included in Table A.1 for each simulation. We also calculated the modeled area above pore pressure change thresholds (0.01 MPa and 0.10 MPa) at targeted depths (Figure A.2). We calculated the modeled area by determining how many model cells were above the stress change threshold and multiplying by the cell area. The targeted depths are directly below the injection interval at 0 km into the crystalline basement;

approximately 1 km below the injection interval in the crystalline basement; and approximately 3.5 km below the injection interval in the crystalline basement.

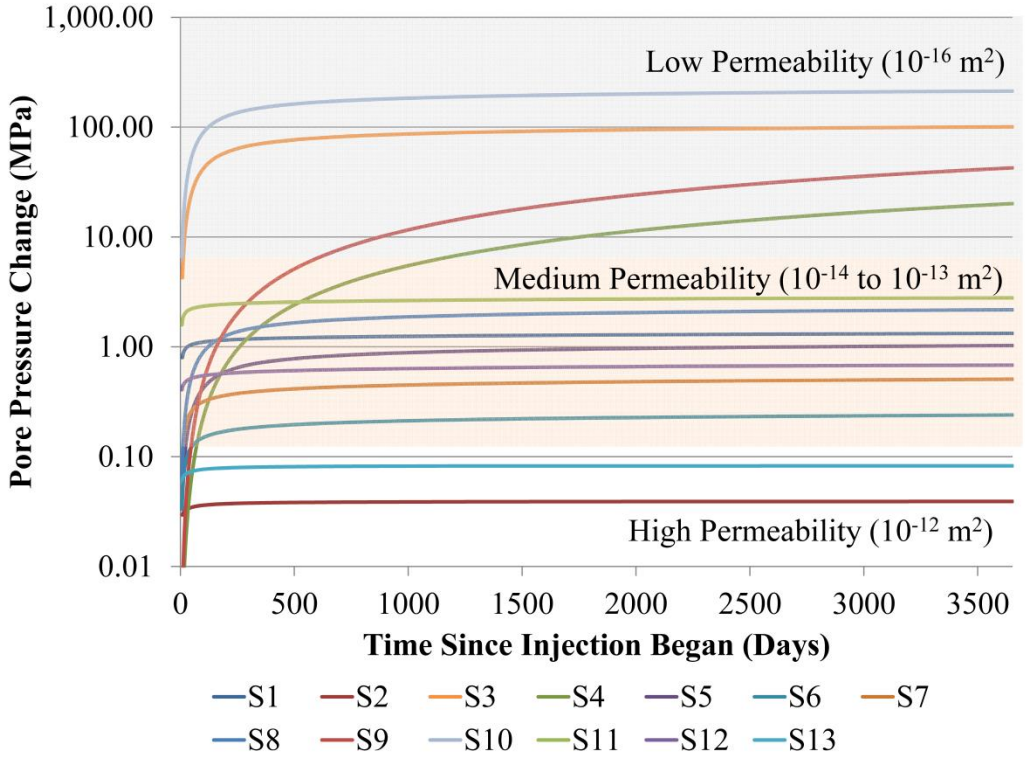

Figure A.2: Modeled pore pressure results for directly below the well in the basement at the yellow dot shown on Figure A.1. The results are labeled by colored lines and full details of the simulation parameters are in Table A.1.

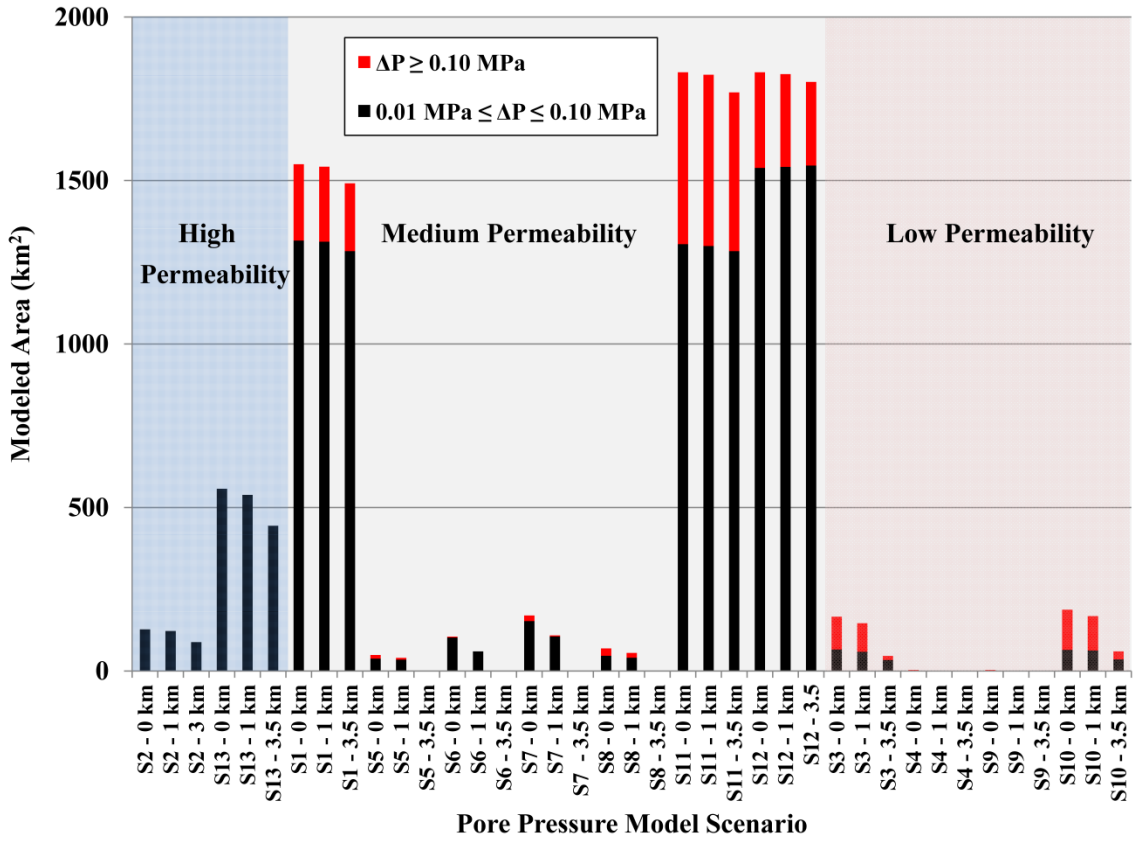

Figure A.3: Modeled area above stress change thresholds from the pore pressure model results for targeted depths below the injection interval within the crystalline basement. The simulations are numbered along the x-axis and the target depth is listed. In addition, the simulations are grouped by permeability (high, medium, and low). The black portion of the bars is the area with a stress change between 0.01 MPa and 0.10 MPa. The red portion of the bars represents the area with a stress change ≥ 0.10 MPa. The total length of the bars (red plus black) gives the modeled area with stress change ≥ 0.01 MPa.

Table A.1: Pore pressure model parameters for all model simulations shown in Figure A.2.

Model Simulation	Injection Interval Permeability (k) [m^2]	Crystalline Basement Permeability (k) [m^2]	Model Specific Storage (S_s) [m^{-1}]	Injection Rate (Q) [m^3/day]	Total Time [days]
S1	1E-14	From 1E-14 to 1E-18	1.E-07	2000	3652
S2	1E-12	From 1E-12 to 1E-18	1.E-07	2000	3652
S3	1E-16	From 1E-16 to 1E-18	1.E-07	2000	3652
S4	1E-16	From 1E-16 to 1E-18	1.E-05	2000	3652
S5	1E-14	From 1E-14 to 1E-18	1.E-05	2000	3652
S6	1E-13	From 1E-13 to 1E-18	1.E-05	2000	3652
S7	1E-13	From 1E-13 to 1E-18	1.E-05	4240	3652
S8	1E-14	From 1E-14 to 1E-18	1.E-05	4240	3652
S9	1E-16	From 1E-16 to 1E-18	1.E-05	4240	3652
S10	1E-16	From 1E-16 to 1E-18	1.E-07	4240	3652
S11	1E-14	From 1E-14 to 1E-18	1.E-07	4240	3652
S12	1E-13	From 1E-13 to 1E-18	1.E-07	4240	3652
S13	1E-12	From 1E-12 to 1E-18	1.E-07	4240	3652

A2. Coulomb Static Stress Transfer Model

We use two idealized fault scenarios shown in Figure A.1b for the Coulomb static stress transfer modeling. We calculate random locations for each event using the Random function in MATLAB with a normal distribution in the along-strike direction (normalized by fault length) and a Weibull distribution in the down-dip direction (normalized by fault width) [*Mai et al.*, 2005]. *Mai et al.* [2005] used a database of finite source models of earthquakes to determine location distributions in different faulting regimes. They normalized the locations by fault size and found that in the along-strike direction the locations are best-fit by a normal distribution with

a mean of 0.5 and standard deviation of 0.23. In the down-dip direction, strike-slip and crustal dip-slip event locations were best fit by a Weibull distribution,

$$P(x) = \frac{B}{A} \cdot \left(\frac{x}{A}\right)^{B-1} \cdot e^{-(x/A)^B}, \quad (4)$$

where A and B are scale and shape parameters, respectively. The best fitting scale parameter, A, is 0.626 and 0.692 for strike-slip and crustal dip-slip, respectively. The best fitting shape parameter, B, is 3.921 and 3.394 for strike-slip and crustal dip-slip, respectively. Since these distributions are normalized by fault size, we chose a fault length (10 km) and width (4 km) to be representative of a mid-continent reactivated fault.

The along-strike lateral coordinate (Y) is calculated using a normal distribution with the parameters of *Mai et al.* [2005] multiplied by the fault length. The depth coordinate (Z) is calculated using a Weibull distribution with the parameters of *Mai et al.* [2005] multiplied by the fault width. We then added 2 km to shift the events deeper. The second lateral coordinate (X) is set either to zero for the strike-slip fault scenario or calculated using the formula for a plane with the normal fault strike and dip (000/60E) that intersects the surface at the axes origin (0,0,0). For the normal fault scenarios, all the events occur along the plane expressed by the following equation:

$$Z = 1.732X, \quad (5)$$

where X, Y, and Z are in kilometers.

We calculate the earthquake parameters using the relations of *Leonard* [2010] shown in Table A.2. The fault width is calculated from dividing the fault area by the fault length with the assumption of a rectangular area of slip.

Table A.2: Earthquake parameter relations of [*Leonard*, 2010] used for the Coulomb static stress transfer models.

Parameter	Strike Slip Fault	Normal Fault
Fault Area, A, (in km^2)	$M_w = 1.0 \text{ Log}(A) + 3.99$	$M_w = 1.0 \text{ Log } (A) + 4.19$
Fault Length, L, (in km)	$M_w = 1.67 \text{ Log}(L) + 4.17$	$M_w = 1.67 \text{ Log}(L) + 4.32$
Average Slip, D_{av}, (D_{av} in m and L in km)	$\text{Log } (D_{av}) = 0.833 \text{ Log}(L) - 1.34$	$\text{Log } (D_{av}) = 0.833 \text{ Log}(L) - 1.07$

Table A.3: Average depths for earthquake catalogs used for the Coulomb static stress transfer models.

		b-value	**Average Depth (km)**
Fault Scenario	**Strike slip**	0.8	4.2
		1.0	4.2
		1.2	4.3
	Normal	0.8	3.8
		1.0	3.9
		1.2	3.8

We explored how varying focal mechanisms influence the Coulomb static stress change. Using the same distribution of b-values, we generated new random locations as described above and added variability in the strike and dip of the faults. *Hardebeck* [2006] found that for small fault lengths focal mechanism variability is within one standard deviation uncertainty of focal mechanisms, ~25°. Focal mechanism studies of induced seismicity in Texas [*Quinones et al.*, 2018] found that the mechanisms in single sequences are surprisingly consistent. We varied the strike of the faults randomly with a mean of 0° north and a standard deviation of 25°. The dip of the faults was also varied randomly with a mean of 90° and 60°, for the strike slip and normal faults respectively, and a standard deviation of 25°. In addition, we varied the rake of the events.

For the strike slip fault scenarios, we allowed the rake of each event to include either normal or reverse slip, but maintained left lateral slip. For the normal fault scenarios, we allowed the rake of each event to include either left or right lateral slip, but maintained normal slip.

We examine the maximum Coulomb static stress change and the modeled area above stress change thresholds of 0.01 MPa and 0.10 MPa at the average depth of the earthquakes (Table A.3). We calculated the modeled area by determining how many model cells were above the stress change thresholds and multiplying by the cell area. The maximum Coulomb static stress change and the modeled area at the average depth of the events for each scenario with a stress change ≥ 0.01 MPa and ≥ 0.10 MPa are included in Table A.4. The modeled area results are presented in Figure A.4. The varied focal mechanism scenarios show a decreased maximum Coulomb static stress change, but similar areas of Coulomb static stress change compared to the scenarios with no variation in focal mechanisms.

Table A.4: Comparison of model results for faulting scenarios with consistent or varying focal mechanisms calculated at the average depth of the events and in the average strike, dip, and slip direction of the source fault.

			Results at average depth of events		
		b- value	**Area (km^2) ΔCSS ≥ 0.01 MPa**	**Area (km^2) ΔCSS ≥ 0.10 MPa**	**Max. ΔCSS (MPa)**
Fault Scenario	**Pure Strike slip**	0.8	28.6	8.9	769.6
		1.0	7.4	1.9	273.3
		1.2	3.4	0.4	11.6
	Varied Strike Slip	0.8	23.8	7.8	36.7
		1.0	6.4	1.0	6.8
		1.2	1.7	0.3	6.0
Fault Scenario	**Pure Normal**	0.8	15.7	5.7	61.7
		1.0	5.2	0.8	17.9
		1.2	1.2	0.2	21.9
	Varied Normal	0.8	27.5	5.1	4.3
		1.0	6.2	0.1	0.7
		1.2	1.0	0.1	1.1

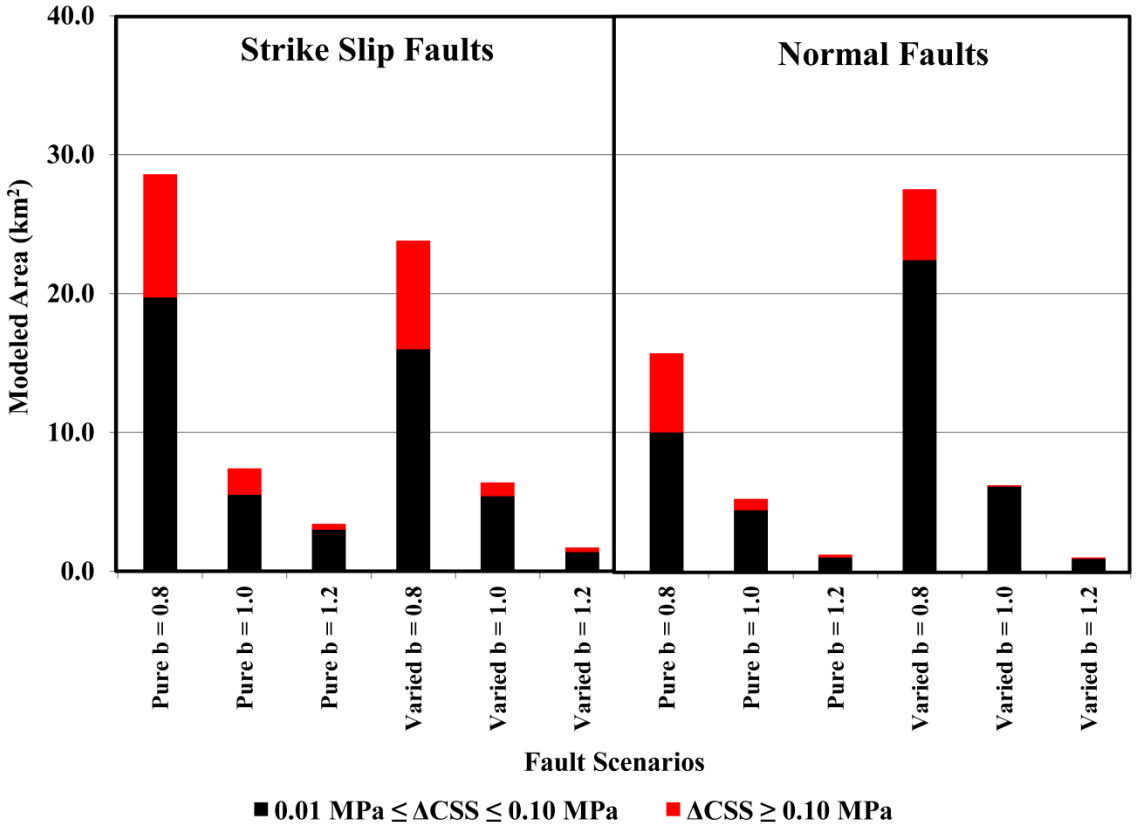

Figure A.4: Modeled area above stress change thresholds from Coulomb static stress transfer model at the average depth for each faulting scenario. The term "pure" indicates scenarios with a consistent focal mechanism for all events and "varied" indicates scenarios where the focal mechanism was allowed to vary. The black portion of the bars is the area with a stress change between 0.01 MPa and 0.10 MPa. The red portion of the bars represents the area with a stress change ≥ 0.10 MPa. The total length of the bars (red plus black) gives the modeled area with a stress change ≥ 0.01 MPa.

In addition to the results presented in the text, we calculate the Coulomb static stress transfer (Table A.3) for the six fault scenarios with varying effective coefficient ranging from low (0.4) to high (0.8). The results are for the average earthquake depths of each scenario (see Table A.3) and in the direction of slip of the modeled fault. The results (Table A.5) show that the maximum Coulomb static stress change is insensitive to effective coefficient of friction, and that the modeled area where ΔCSS ≥ 0.01 MPa is relatively insensitive to effective coefficient of friction.

Table A.5: Comparison of faulting results for varying effective coefficients of friction.

Effective coefficient of friction			**μ = 0.4**	**μ = 0.6**	**μ = 0.8**	**μ = 0.4**	**μ = 0.6**	**μ = 0.8**
		b- value	**Max. ΔCSS (MPa)**			**Area (km^2) ΔCSS ≥ 0.01 MPa**		
Fault Scenario	**Strike slip**	0.8	769.6	769.6	769.6	22.8	28.6	35.8
		1.0	273.3	273.3	273.3	6.5	7.4	8.4
		1.2	11.6	11.6	11.6	3.2	3.4	3.8
	Normal	0.8	61.7	61.7	61.7	17.1	15.7	14.9
		1.0	18.1	17.9	17.6	4.7	5.2	5.5
		1.2	21.8	21.9	22.0	1.2	1.2	1.2

Finally, we also explored how the static stress transfer differed for the cumulative effect of many small magnitude events from that of a single moderate event of similar moment (Table A.6). The maximum change in Coulomb static stress is much lower than in the cases of the small earthquakes with the same cumulative moment. In addition, for the majority of the cases, the area of increased Coulomb stress change is much smaller for the moment equivalent moderate events compared to the scenarios of small earthquakes with the same cumulative moment.

Table A.6: Model results for faulting scenarios of a single event with similar moment as the idealized scenarios presented in Table A.4.

					Model Results at 5 km Depth		
		b-value	**Equivalent Magnitude**	**Moment (dyne cm)**	**Area (km^2) ΔCSS ≥ 0.01 MPa**	**Area (km^2) ΔCSS ≥ 0.10 MPa**	**Max. ΔCSS (MPa)**
Fault Scenario	**Pure Strike slip**	0.8	4.8	1.78×10^{23}	32.73	1.86	3.42
		1.0	4.1	1.56×10^{22}	1.56	0.05	0.30
		1.2	3.6	2.90×10^{21}	0.14	0.00	0.06
	Pure Normal	0.8	4.6	8.76×10^{22}	10.75	0.58	2.17
		1.0	3.9	8.25×10^{21}	0.53	0.01	0.20
		1.2	3.4	1.49×10^{21}	0.03	0.00	0.04